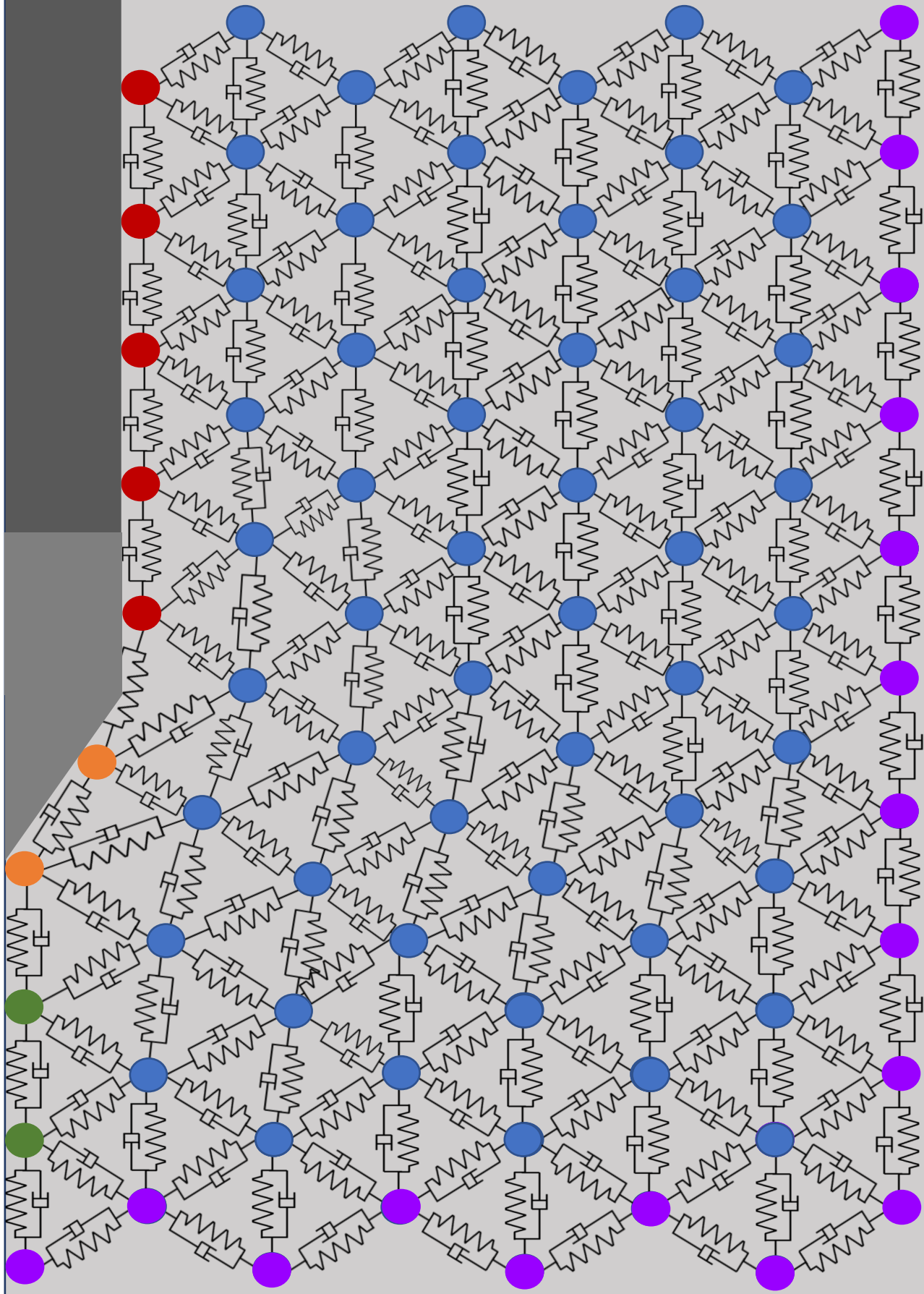# A two-dimensional pile penetration model for the GBM Vibro-drill

by L.J. van der Bijl

A two-dimensional pile penetration model for the Vibro-drill;

Develop a two-dimensional pile/soil interaction model that is capable of describing the pile/soil interaction during pile installation using the GBM Vibro-drill.

By

L.J. van der Bijl BSc.

in partial fulfilment of the requirements for the degree of

Master of Science
in Offshore and Dredging Engineering

at the Delft University of Technology,
to be defended publicly on Monday the 7th of October, 2019 at 15:30 AM.

Thesis committee:	Prof. Dr. A.V. Metrikine,	TU Delft
	Ir. J.S. Hoving MSc,	TU Delft
	Ir. B.J.M. Arntz	GBM Works
	Dr.ir. A. Tsouvalas	TU Delft

1 Abstract

The energy transition results in large offshore windfarms being installed. The most common support structure for a wind turbine at sea is a monopile. These are currently installed by large hydraulic hammers. However, hammering produces a lot of underwater noise which may harm marine life (Kastelein, 2014). Therefore, the industry is looking for new installation methods that are more environment friendly. GBM Works aims to implement such a new installation technique called the Vibro-drill. They introduce a revolutionary new design which is to replace the hammering technique. Vibrations, jetting and liquefaction are used to reduce the soil resistance. This reduction is so powerful that the monopile sinks into the ground under its own weight without producing the harmful underwater noise.

Before each monopile is installed an analysis is made of the factors determining the chance of a successful installation. This process is called a penetration prediction. For the industry to accept the Vibro-drill installation method, penetration predictions are required to prove the applicability of the new technique. The radical changes in the installation process used by this technique make it impossible to use current penetration prediction methods. This means that a new prediction method needs to be developed that takes into account the specific features of the Vibro-drill.

This thesis aims to address this problem by way of providing building blocks for the development of a fully-fledged penetration prediction model that is applicable to the Vibro-drill method. To this end, this thesis will focus on delivering a two-dimensional soil model in penetrated by a pile.

The two-dimensional approach, which is the basis of this thesis, has of course its limitations as only a part of the pile and soil are included in the model. The assumed point symmetry over the centreline of the monopile leads to only a slice of the pile being modelled.

The soil is captured using a lattice model. A well-known practice for modelling soil in a two-dimensional way. The properties of the lattice are determined using Cone Penetration Test data. As a result the model represents different layers of soil along the depth. The model uses a rigid pile to penetrate the soil. The penetration of the pile causes a reaction force in the soil. This force is used to calculate the friction forces. The reaction force and the friction force are the basis for calculating the penetration speed of the pile. From this it follows that the penetration speed and final installation depth depend on the different soil layers within the soil model.

A first step towards validation is made. The pile/lattice interaction is verified and the results are compared to test data. A sensitivity analysis is performed to verify the independence of the lattice size and resolution on the modelled penetration speed of the pile. Subsequently the penetration predictions of the model in its current form are analysed. The results are compared to the real-life outcome of tests with the Vibro-drill.

From this first attempt to validation the conclusion can be drawn that the two-dimensional model, as developed in this thesis, could be a suitable basis for further work on a viable penetration prediction method for the Vibro-drill technique. Finally, recommendations are made for further enhancing the model with a view to its eventual implementation as a fully functional penetration prediction model for the Vibro-drill.

An electronic version of this thesis is available at http://repository.tudelft.nl/

i. Preface

The research that is the subject of this thesis was undertaken with a view to obtaining a Master in Offshore and Dredging Engineering at the Technical University of Delft. Conducting this study has been a long and sometimes challenging journey into often uncharted areas. It could never have been done without the advice, help and support of other people. To them I am immensely grateful.

Firstly, I wish to express my gratitude to the committee that supervised my work on this thesis, consisting of Prof. Dr. A.V. Metrikine, Ir. J.S. Hoving and Ir. B.J.M. Arntz.

Ir. B. Arntz of GBM Works not only provided the infrastructure for this study by making a place available in the premises of his company, but he also gave me invaluable advice. His day-to-day availability for bouncing off ideas was of great help to me.

A special thanks also to Ir. J.S. Hoving who during my research often stimulated and inspired me, particularly when I threatened to lose my way. He was always there to give me support and advice when I most needed it.

I very much appreciated working with the colleagues at GBM works who made my graduation time also a socially enjoyable period.

I also want to thank my girlfriend for her support and patience during the time I was working on this thesis. She was always there to cheer me up when a came home from a long day at the office.

Last but not least, I would like to thank my parents who have always supported me in every way possible during my long time as a student and especially my dad, who has reviewed this report multiple times. I could always rely on them for advice or help if I needed it and even during hard times they always kept believing in me. Without them I could not have finished this masters and for that I am forever thankful.

Leonard van der Bijl
Delft, October 2019

Table of contents

1 Introduction to monopile installation using the Vibro-drill

All over the world governments are making an effort to transfer from with fossil fuels and are investing in renewable energy. One of these renewable energy sources is wind. In the early 1980's the first large scale onshore wind turbines were installed. Soon it became clear that wind turbines on land were causing problems. They ruin the landscape and produce a lot of noise. New foundation techniques made it possible to install wind turbines at sea (Arshad & O'Kelly, 2016) in so called offshore windfarms. At sea they would generate less noise pollution and less visual pollution. It also comes with the additional benefit of having a smooth surface with a lot of wind, which ensures a better efficiency. In the Netherlands, these offshore windfarms are now becoming one of the most important sources of renewable energy. As we speak, large scale projects are being installed or planned to be installed in the near future.

1.1 Offshore wind industry

The offshore wind industry is therefore large than ever before (Wind Europe, 2018). Especially in the Netherlands, where a lot of large offshore contractors are located, the effects of the growing market are noticeable. New courses concerning offshore wind are introduced at universities and former offshore oil contractors are converting their fleet to suit the growing demand in offshore wind installations.

1.1.1 Market description

Not only in the Netherlands the offshore wind industry is growing. As Figure 1 shows, countries all over the world, like China and the US, are seeing the potential and are investing in new offshore wind projects. A large percentage of these future projects uses monopiles as foundation as they are the cheapest form of foundation in water depths until 50 meters (Van De Brug et al., 2010). Moreover, a large part the projects that use monopiles are installed in soil situations that suit the Vibro-drill.
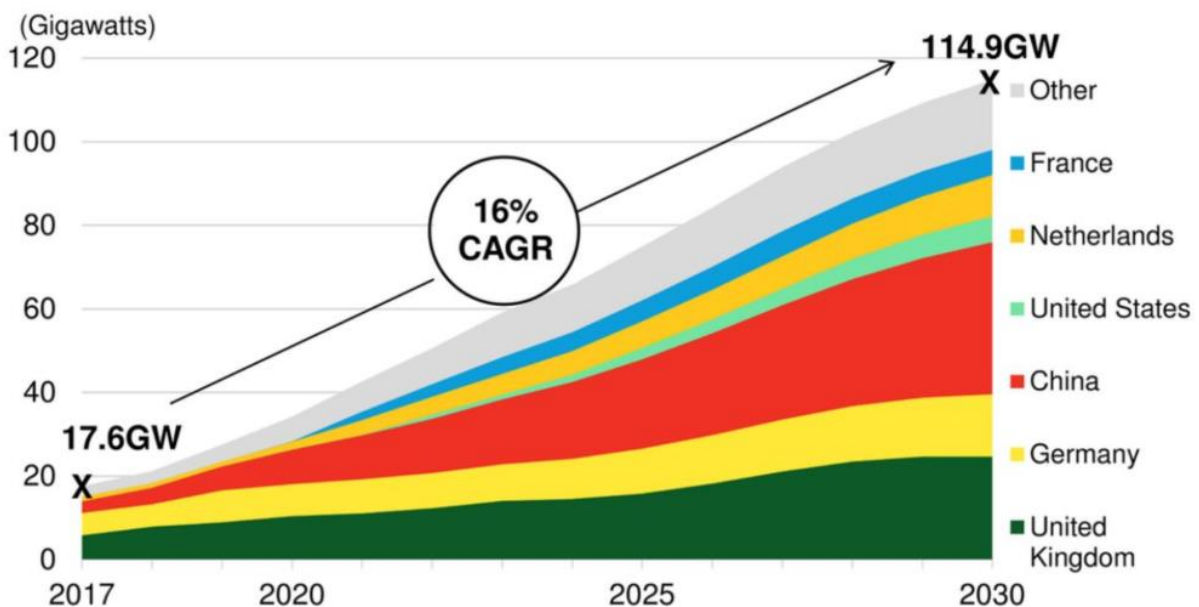
Figure 1: Offshore wind market growth

1.1.2 Installation of a monopile

Wind turbines are supported by a foundation. In most cases this foundation consists of a large diameter pile, called a monopile. Currently, during the installation process of a monopile, a hydraulic hammer is used to drive the monopiles into the ground. The process starts by upending the monopile from the deck of the ship into a gripper frame at the side of the ship. The hydraulic hammer is lifted and installed on top of the

monopile. For a typical monopile it takes about 2000 blows from the hydraulic hammer before the monopile reaches its target depth. When this depth is reached the hydraulic hammer is lifted from the monopile and the ships sails to the next installation location.

Figure 2: Current noise mitigation: bubble curtain

1.1.3   Challenges in the industry

There are however some problems with this hammering technique. Each blow of the hydraulic hammer sends large vibrations through the monopile structure. After 2000 blows this results in fatigue damage, especially in the upper part of the monopile were the hydraulic hammer exercises its force. To overcome this problem the monopile is overdesigned. The thickness of the wall is increased along the full length of the monopile. Resulting in a lot of added steel, and hence, costs.
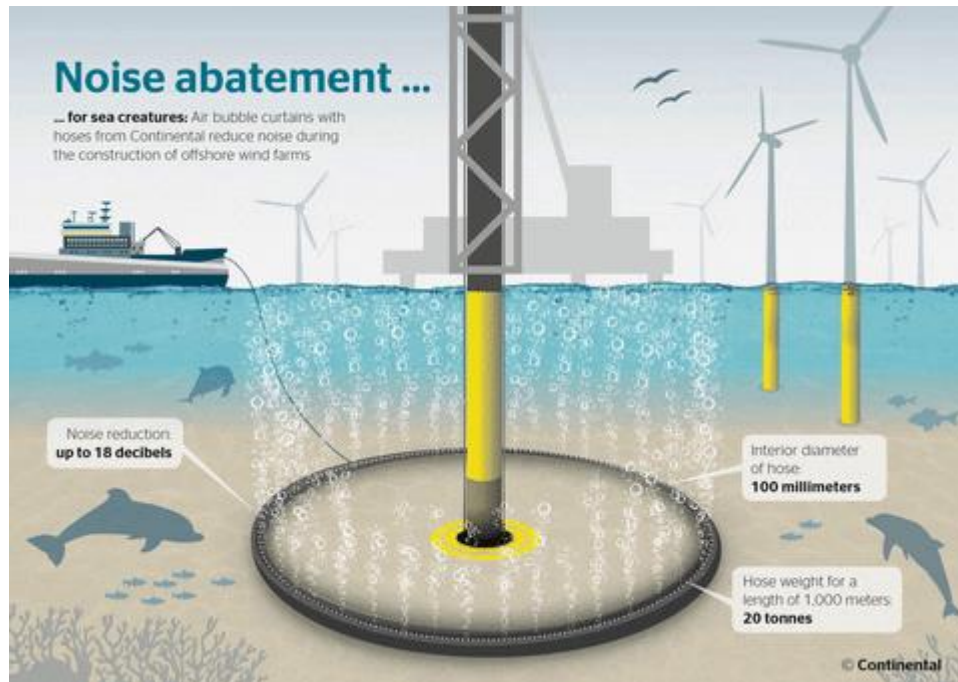
This is not the biggest problem however, more importantly, during the hammering process a lot of underwater noise is produced. This noise is harmful to the marine life in the area. It can permanently damage the hearing of large sea mammals and it can do even greater damage to smaller sea life. To reduce this negative impact on marine life several measures are taken. One of these measures is using bubble curtains to block the sound shown in Figure 2. As the name suggest, a curtain of bubbles is created around the monopile which partly blocks the noise made by the hammering. However, this only reduces the noise level until it falls within the level that is allowed by EU legislation. On top of that, the daily cost of one bubble curtain is 100.000 euros and for the sound to be dampened enough, three of those bubble curtains are required. Resulting in a daily cost of 300.000 euros per day (Schrocht, 2015).

1.2   Introduction to the vibro-drill installation method

It goes without saying that the above-mentioned problems pose an interesting challenge to technicians in this area of expertise. There are several initiatives underway to find solutions to these problems. One of these initiatives is undertaken by GBM Works which is working on a solution that would solve both these problems. They introduce a revolutionary new design which is to replace the hammering technique. Vibrations, jetting and liquefaction are used to reduce the soil resistance. This reduction is so powerful that the monopile sinks into the ground under its own weight. This new technique is called the Vibro-drill.
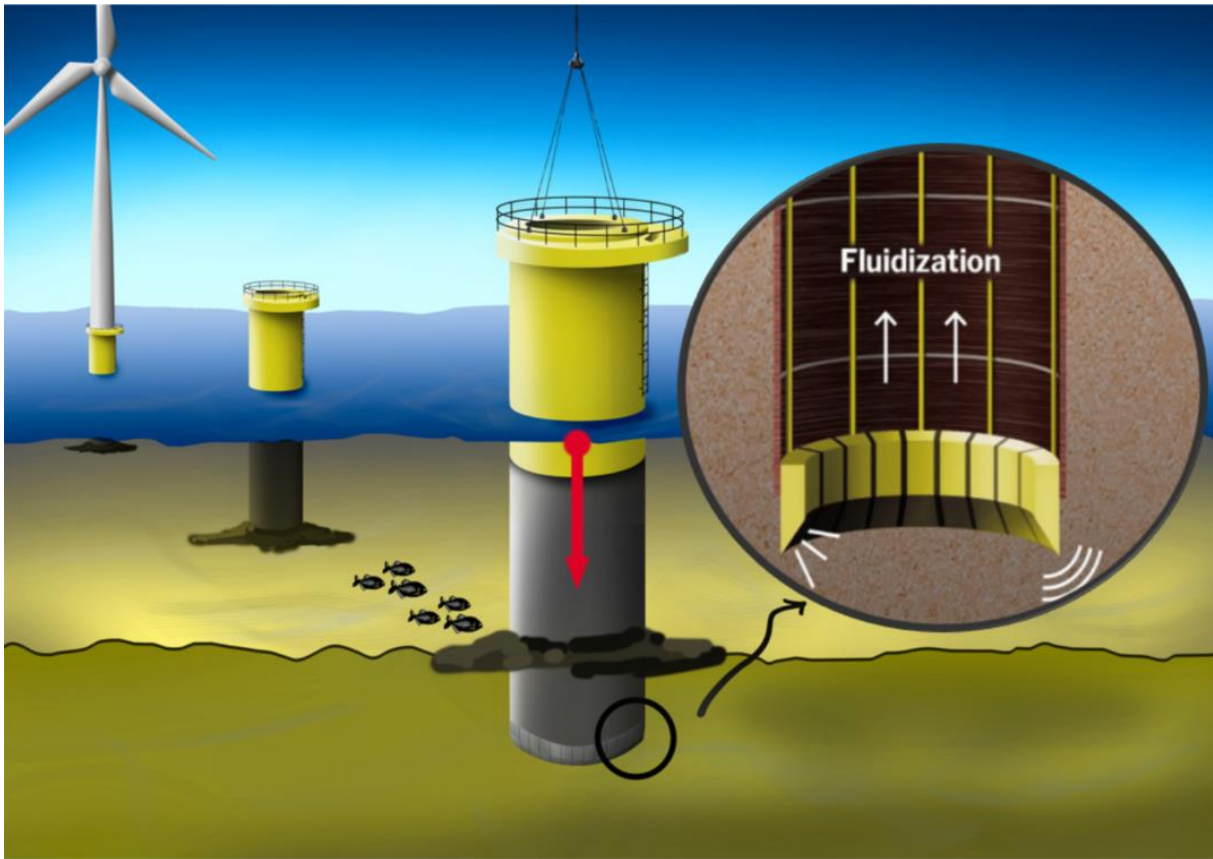
Figure 3: Working principles GBM Vibro-drill

1.2.1 Working principles

The Vibro-drill is located on the bottom of the hollow monopile, it influences the soil in two ways. It generates vibrations and uses high power jets along the diameter of the pile. These jets are pointed downwards, upwards and towards the inside of the pile. They do not point outwards as that might influence the soil on the outside of the pile and thus the bearing capacity. A picture of what the Vibro-drill looks like is depicted in Figure 3.

Reduction of tip resistance

The vibrations and jets have an effect on the tip resistance. They both induce a phenomenon called soil liquefaction. This process causes the soil to behave like a liquid. In saturated soil the pores between the soil particles are filled with water. When the soil is shaken due to vibrations these soil particles start to displace, causing the pores between the particles to change. As a result, water travels from one pore to another between the soil particles, momentarily disconnecting the two soil particles which results in a reduction of the friction forces between the soil particles and thus a reduction in the stiffness of the soil.

Jetting works in a similar manner. Water is introduced to the soil nearby the tip. Consequently the pore water pressure increases. This causes a flow of water from the tip to locations further away from the tip with a lower pore pressure. Here again, as the water flows from pore to pore it momentarily disconnects the soil particles, which results in a reduction in soil stiffness.

As described above, both vibrations and jetting result in a reduction of the soil stiffness, which in turn reduces the tip resistance.
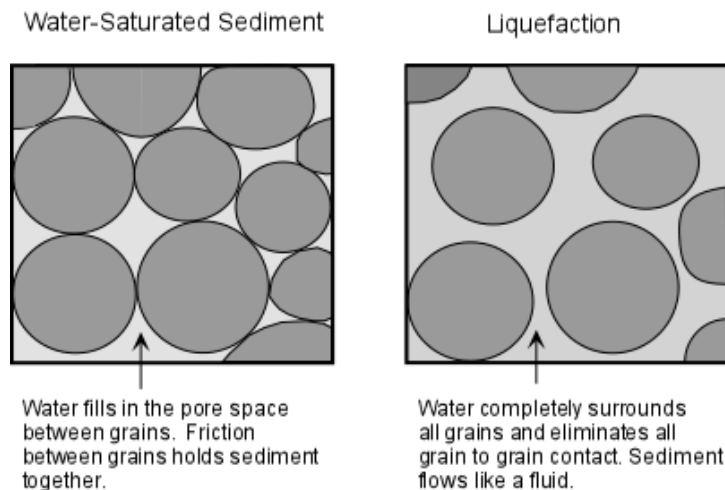
Water-Saturated Sediment   Liquefaction

Water fills in the pore space between grains. Friction between grains holds sediment together.

Water completely surrounds all grains and eliminates all grain to grain contact. Sediment flows like a fluid.

Figure 4: Liquefaction process

Reduction of shaft resistance

The shaft resistance is overcome in two ways. On the inside of the pile fluidization takes place. The jets pointing inwards and upwards inject a lot of water into the soil creating a similar phenomenon as the liquefaction at the tip. Only now the amount of water is such that friction between the particles totally disappears and the soil behaves like liquid. As a result, the friction on the inside of the pile is drastically reduced.

On the outside of the pile the friction is reduced using vibrations. The pile is induced with vibrators attached to the pile. This results in a relative acceleration between the soil and the pile. In doing so the friction between the soil and the pile is defined by the kinetic friction instead of the static friction, which is much lower.

1.2.2 Advantages

The advantages of the Vibro-drill technique, as currently developed by GBM are self-evident. The harmful noise produced by the traditional hammering method is drastically reduced. The same goes for the fatigue damage caused by this method. The substantial reduction in soil resistance and continues vibrations result in a much faster descent of the pile into the seabed. Last but not least, the Vibro-drill technique avoids some of the costs related to hammering.

However, before the Vibro-drill technique can be successfully implemented, further study and problem solving will be required.

1.3 Problem description

Before each monopile is installed an analysis is made of the factors determining the chance of a successful installation. Cone Penetration Tests (CPTs) provide the soil properties for the location after which a penetration model simulates the installation of the monopile. From this installation simulation the penetration speed, the final depth and the installation time are obtained. This process is called a penetration prediction.

For the industry to accept the Vibro-drill installation method, penetration predictions are required to prove the applicability of the new technique. The radical changes in the installation process that is used by this technique make it impossible to use current penetration prediction methods. This means that a new prediction method needs to be developed that considers the specific features of the Vibro-drill.

One of the problems with the development of a pile penetration prediction method is how to arrive at a workable model of the soil. To this end in this thesis a lattice model will be used, a well-known practise for modelling soil.

1.4   Research objectives

This thesis addresses the problem described in chapter 1.3 by way of providing building blocks for the development of a fully-fledged penetration prediction model that is applicable to the Vibro-drill method. In doing so, this thesis will focus on delivering a two dimensional representation of the soil model in which a pile is penetrated. For this purpose, the soil will be modelled as a lattice. More information on lattice models and the implementation within this model can be found in chapter 0 and 3.2. The pile/lattice interaction is verified and the results are compared to real life test data, which is a first step towards validation.

Following from the scope the main goal of this thesis project becomes:

Develop a two-dimensional pile/soil interaction model that is capable of describing the pile/soil interaction during pile installation using the GBM Vibro-drill.

Within this framework the following sub-objectives can be discerned:

- Understand the working principles of a lattice model for soil application.
- Derive lattice properties that correspond to soil properties obtained from CPT.
- Describe the pile lattice interaction during pile penetration.
- Perform a sensitivity analysis regarding lattice properties.
- Discuss hypothesis on the applicability and validity of the model.

1.5   Approach

First a literature study is performed regarding the research on existing soil and penetration models, specifically with a view to obtaining an insight in the working principles of a lattice model. This study will involve an assessment of whether these models or parts of them are of relevance to the Vibro-drill technique. The study focuses also on the lattice model with a view to obtaining an insight in its working principles.

The basis of the model is developed in Python. To be able to make a start of an accurate description of the pile penetration, the model should capture the soil reaction in at least two-dimensions. The two-dimensional approach which is the basis of this thesis, has of course its limitations as only a part of the pile and soil are included in the model. This two-dimensional approach is reflected in the pile/soil model by means of assuming point symmetry and symmetry inside and outside the pile.

Following from the concept of point symmetry, only a "slice" of the pile/soil needs to be modelled. For shorter computational time purposes, this "slice" is then assumed to be symmetrical resulting in only the outside of the pile/soil being modelled. This process is explained in Figure 5.
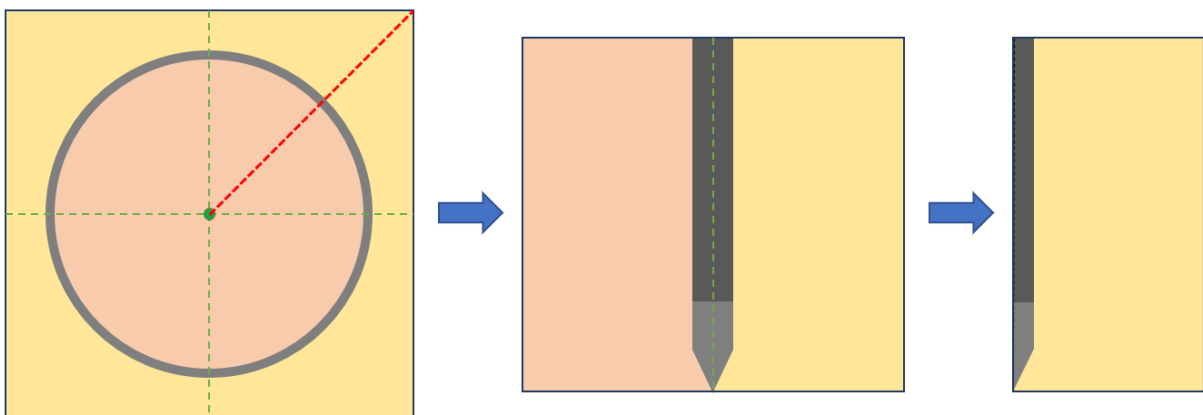

Figure 5: From 3D pile to 2D model

CPT data from a previous test location of GBM are used to define different layers within the soil model. The pile is modelled as a rigid body. Contact conditions for the pile and the soil are defined. The penetration

process of the pile through the lattice is developed. The penetration of the pile causes a reaction force in the soil model. This force is used to calculate the friction forces. As a result, the penetration speed and final installation depth depend on the different soil layers.

Finally the forces that play a role in the pile/soil interaction are verified and the influence of the soil model on the penetration is assessed.

1.6 Outline

This report consists of several chapters, this section is used to shortly introduce them. Chapter 1 introduces the installation of a monopile. It highlights the shortcomings of the current methods and introduces the ground-breaking GBM Vibro-drill method. Finally the thesis topic and its scope and relevance are explained. Chapter 2 displays the current knowledge relevant to the thesis topic. It shows the existing penetration and soil models. Chapter 3 explains how the model is built and how it works. It starts with a general overview of the model, after which it goes further into each single aspect of the model. Chapter 4 provides an insight in the verification process. The forces that play a role in the pile/soil interaction are verified and the influence of the soil model on the penetration is made the subject of a sensitivity analysis. Chapter 5 shows and discusses the results of the model. Finally, chapter 0 contains the conclusions and recommendations regarding the model. The results of this study are discussed, and recommendations are made for further development of the penetration model.

2 State-of-the-art of soil-penetration models

A literature study was conducted with a view of obtaining insight into the previous research on topics relevant to the subject of this thesis. The study focused on existing penetration models so as to assess whether they have features that could be useful for the development of a two-dimensional penetration model. Thus as far as models are identified that are relevant (Arntz, 2018) (Keuzenkamp, 2017), attention will be given to how they operate and how well they represent reality. Various criteria will be used to determine if, and if so to what extent, they could be useful for the purpose of this thesis. If need be, models that would not be applicable in their integrity could be broken down into components that might well have relevance to the Vibro-drill technique. Another subject included in the study is the concept of a lattice. This concept is an important element of the two-dimensional model as developed in this thesis and, as such, requests some further attention.

2.1 Existing penetration models

As stated before, most of the existing penetration models relate to the use of the hammering technique. These models are of no or rather limited relevance for the Vibro-drill method, which is radically different and, therefore, requires a different approach in modelling. However, existing penetration models which are developed for vibratory driving of piles and sheet piles, can be of interest for the Vibro-drill method. Therefore a study is performed in which such penetration models are identified and analyzed.

A lot of different modelling approaches and engineering design tools have been used to assess the vibratory drivability of piles and sheet piles (Whenham & Holeyman, 2005), (Mens, Korff, & van Tol, 2012). The most simple models are based on a force equilibrium (Jonker, 1987), (Azzouzi, 2003), (Van Baars, 2004). They determine whether the force generated by the vibrator can overcome a certain soil resistance and thus provide an insight into the dimensions of the vibrator which is capable of installing that particular pile or sheet pile. However, these models do not deal in any with the penetration speed and are therefore considered too elementary to investigate further.

To be able to establish something about the penetration speed, a one-dimensional model is required in which the movement of a pile, seen as a rigid body mass, is described from inertial equilibrium conditions. Mathematical expressions are used to describe the soil resistance. They are determined using experimental results. The majority of the models fall within this category (Holeyman, 1993), (Dierssen, 1994), (Van De Brug et al., 2010). They are relatively straight forward and fast and with enough experimental results most of the models are calibrated such that they provide a relatively reliable penetration prediction. At the TU Delft there are two models that were construed prior to this thesis. Both are developed at the TU Delft by Jeroen Keuzenkamp and Ben Arntz respectively and both deal with vibratory pile penetration (Arntz, 2018) (Keuzenkamp, 2017). The following sections 2.1.1 and 2.1.2 will go further into these models and will ascertain to what extent they might be useful for the purpose of this thesis.

Discrete element method, from now on referred to as DEM, is a method in which the soil is modelled as particles that come into contact with each other. This contact is described in so called contact conditions. There are some pile penetration models that use this approach (Matlock, 1977), but they are mostly focussed on the soil reaction as a pile penetrates the soil (Wang & Zhao, 2014), not so much the penetration itself. This method is commonly used to describe soil problems on a micro-scale. The model in this research however, is macro-scale. If the DEM approach is used for this model the computation time and complexity would be enormous and therefore it is deemed to be of no practical value for this research.

Another method for modelling pile penetration is the finite element method, from now on referred to as FEM. There are several models that use the FEM approach (Chow and Smith, 1984), (Smith & To, 1988), (Leonards et al., 1995), (Cudmani and Sturm, 2006), (Mabsout, Reese, & Tassoulas, 1995), (Henke & Grabe, 2006), (Henke & Grabe, 2006). Although this method is applicable for a penetration model, it has one large

drawback. It does not model waves propagating through the soil. Also this method falls therefore short off the requirements for this thesis.

For this thesis the decision was made to use the lattice model to represent the soil. During the literature study it became clear that this method is not commonly used for pile penetration models. It could therefore provide a new view on how a pile penetration model can be made using a lattice model. In section 2.2 provides an insight in the way a lattice model is used to model soil.

2.1.1 One-dimensional penetration model

The thesis of Jeroen Keuzenkamp focused on a soil compaction method by means of a vibratory drill (Keuzenkamp, 2017). In this process a drill attached to a probe uses vibrations to penetrate the soil. Even when the probe is fully penetrated the drill keeps exerting vibrations onto the soil. The vibrations cause the soil to densify. A schematic overview of this process is shown in Figure 6. This technique is used in the dredging industry to densify reclaimed land.
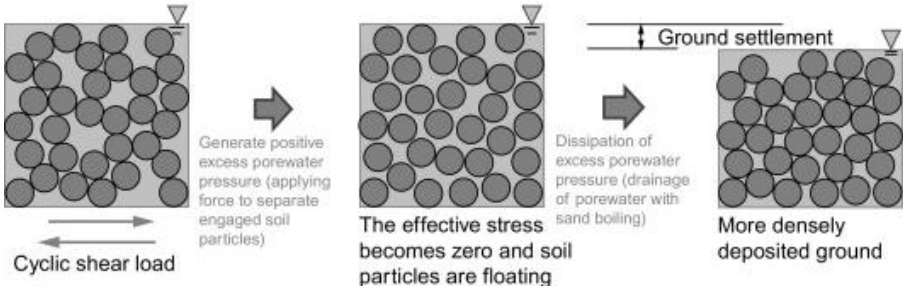

Figure 6: Liquefaction compaction process

Although this research is related to on the installation of a monopile, the vibratory drilling process uses the same liquefaction process as the Vibro-drill. It contains a one-dimensional penetration model simulating the penetration of the drill and probe into different soil layers. It simulates the pile and drill as a point mass and uses a spring damper element to simulate the elastic deformation of the soil and a damper slider element to simulate the plastic deformation of the soil. The vibratory forces are modelled using a sinusoidal force acting on the point mass. A configuration of the model is shown in Figure 7.
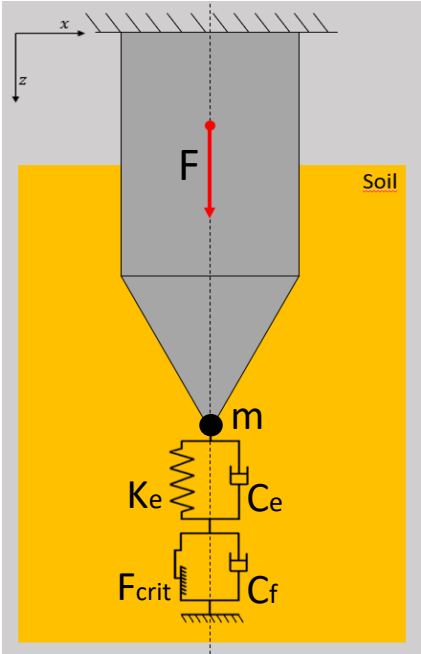

Figure 7: One-dimensional penetration model J. Keuzenkamp

The model uses a CPT correlation to translate the CPT data into usable soil properties like Shear and Youngs modulus. These properties are then used to define different soil layers in values for the spring and damper coefficients and the critical force of the slider element. A stick/slip approach is used to simulate the transition between elastic and plastic deformation of soil. Stick and slip are two conditions of the model. When the model is in stick conditions only elastic deformation takes places, this is achieved by generating the equation of motion of the system with only the contribution of the spring/dashpot element. When the critical force of the slider element is exceeded, the system transitions to slip condition. The equation of motion for this condition is generated using both the spring/dashpot element and the slider/dashpot element. The plastic deformation of the soil takes place in the slip condition and is defined by the displacement of the slider element.

The model only takes forces and displacements in Z-direction into account, which is not sufficient for the two-dimensional model in this thesis, however, the soil representation using CPT data is an interesting attribute. Therefore, the CPT correlation to obtain the soil characteristics from the CPT data is also used for this research.

2.1.2 One-dimensional penetration model that captures two-dimensions

The second model dealing with vibratory pile penetration was developed by Ben Arntz, the founder of the company GBM works. The company that develops the Vibro-drill. In his master thesis a feasibility study regarding the Vibro-drill was performed. Experiments with a scaled prototype were conducted and, using the results of these experiments, a one-dimensional penetration model was created. This model uses a similar technique as the model of Jeroen Keuzenkamp. It uses the same spring/dashpot and slider/dashpot elements and stick/slip technique but it places them under an angle. In doing so, displacements and forces in both X- and Z-direction can be taken into account. This creates the opportunity to introduce the bending stiffness of the pile and how the pile is affected by vibrations. A new, more precise penetration method can be developed. For further information on the working-principles reference is made to (Arntz, 2018).

Although this model is specifically built for Vibro-drill application, the one-dimensional properties of the model make it of limited value for further development. Therefore, in this research a new model is constructed in which a two-dimensional soil displacement is incorporated.
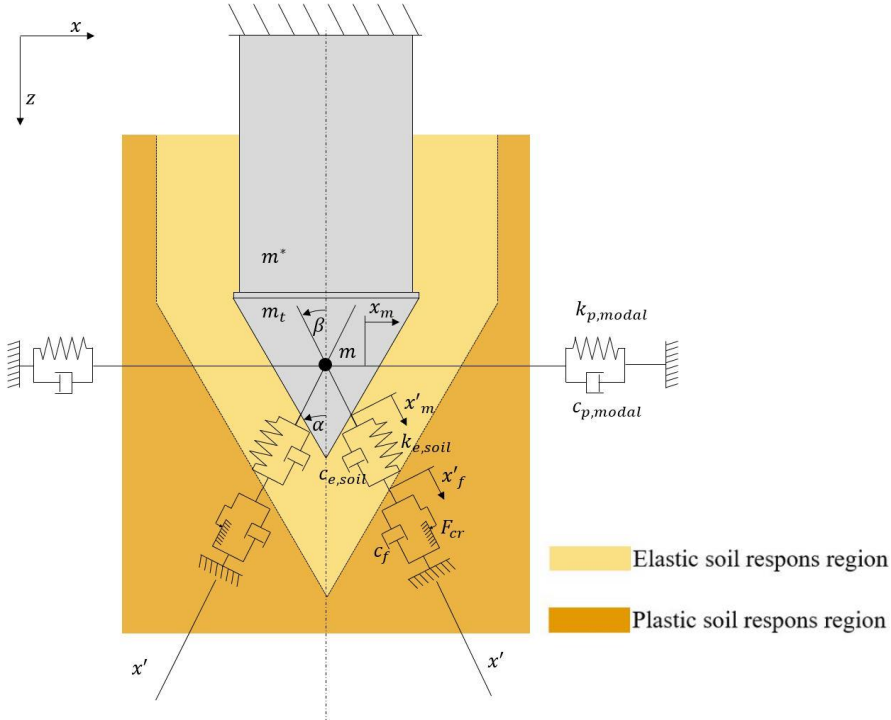

Figure 8: One-dimensional penetration model B. Arntz

2.2 Lattice model

A lattice model is a discrete physical model that is defined on a lattice. This lattice can have all kinds of shapes and sizes. It can be used for all kinds of purposes. The Lattice Boltzmann method, for instance, is used to replicate fluid flows.

In this research, the purpose of the lattice model is to simulate the soil. A similar approach is used in the research of J.S. Hoving (Hoving, 2019). It is a combination of point masses which are connected via spring/dashpot elements. The point mass is called a node. This node captures the soil reaction of the soil volume it represents. If the node is displaced, the connection between the other nodes ensures that they too are affected by the displacement.

The lattice model is a well-known practice for modelling soil in a two-dimensional way. A lattice can have all kinds of shapes and sizes, the lattice used in this research, however, is built up using point masses, springs and dampers in a hexagonal shape. Each point mass represents the mass and location of a certain volume of soil. The dampers represent the energy that is dissipated when this volume of soil is displaced within the lattice, the springs mimic the elastic deformation of the soil. The equation of motion of a specific mass in the lattice is determined by the boundary conditions and its location within the lattice.
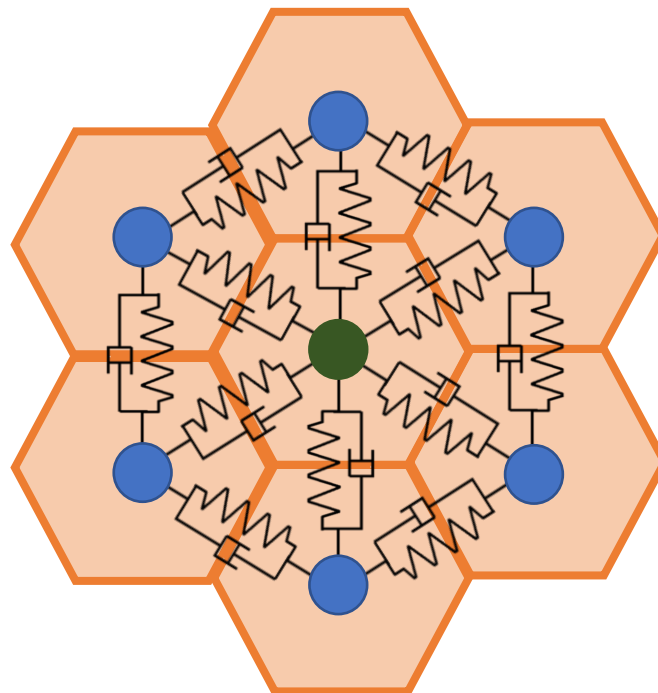

Figure 9: Hexagonal lattice structure

As will be clear form the above, existing models sometimes do have elements or use concepts that are of a certain relevance to the development of a two-dimensional penetration model. On the other hand, there is still a lot of uncharted area which is not surprising as we are dealing with a totally new technique. Chapter 3 will explain further how the two-dimensional model has taken shape.

3 Penetration Model Description

The goal of this thesis is to provide a pile penetration model that accurately simulates the pile/soil interaction in two dimensions. In doing so an important step is taken in the development of a two-dimensional pile penetration model for the Vibro-drill installation method. This model will provide a better insight in the forces that play a role in the process of a pile moving through soil. To be able to describe the pile/soil interaction, several components need to be present in the model. This chapter explains what these components are and how they interact.
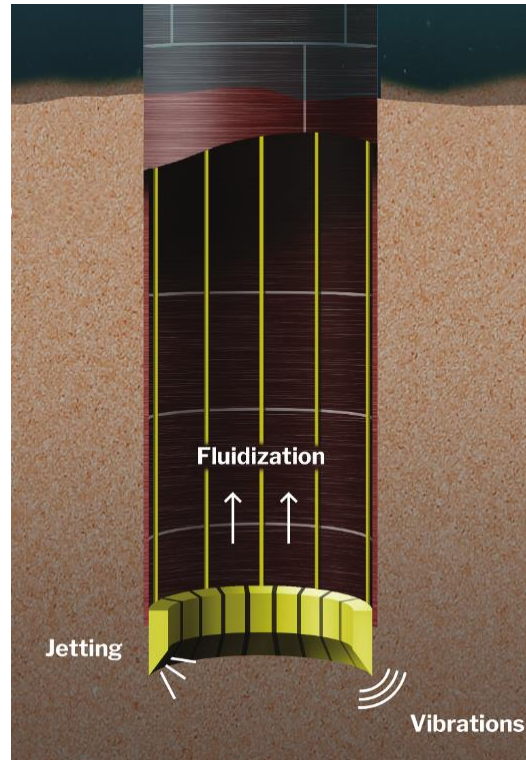
Figure 10: Working principles Vibro-drill

3.1 Model components

At first glance the model can be divided into three main components. A pile, the soil and the Vibro-drill. The pile is assumed to be a rigid body, it is a solid object that can't deform. Irrelevant of time and external forces the distance between any two points within the rigid body remains the same. This assumption facilitates the incorporation in the model. The pile can now be modelled as a certain area that can only move up or down. The soil however, is assumed to undergo large deformations, these are caused by the interaction between the pile and the soil. The large deformations and the inhomogeneous character of soil make the modelling of and the research of this part challenging. The interaction between a penetrating rigid pile and a lattice is new scientific terrain. This makes it an interesting subject for further development of the Vibro-drill penetration model. As regards the Vibro-drill, its effects are simplified, since this model is mainly focused on the interaction between the pile and the soil and not on the Vibro-drill itself. Only the added forces generated by the excentres are taken into account and the effects of these forces on the penetration are part of this study. The three main components of the model now become soil, pile/lattice interaction and the Vibro-drill.

3.1.1 Soil

There are a lot of different types of soil. Each having different characteristics when it comes to pile penetration. Especially when, instead of hammering, methods like vibrations and jetting are used to penetrate the pile. These latter methods are much more sensitive to soil changes (Groen, 2016) and since the soil can change tremendously between locations just several meters apart, it is important to know in detail the existing soil situation at the location of installation.

Currently, CPT measurements are the industry standard to obtain soil data. From the CPT types of soil can be determined that are present along the installation depth of the monopile. The soil characteristics of the model can then be calculated according to the results of the CPT measurements. Finally, the model will produce a penetration prediction on which the installation plan for the monopile can be based.
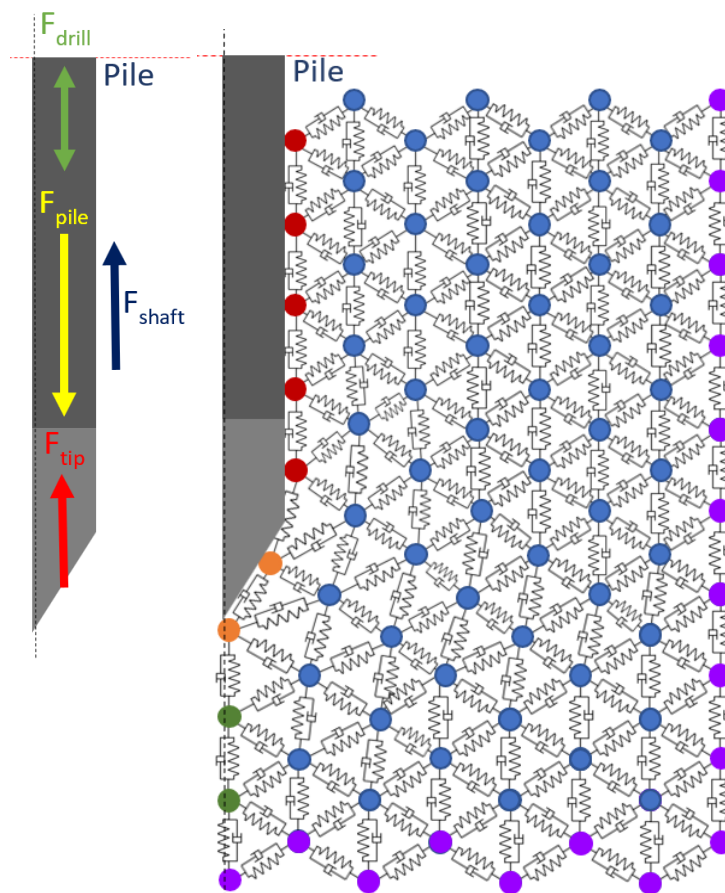

Figure 11. Lattice model and pile with relevant forces

Modelling the soil is one of the most challenging aspects of this research. If the modelled soil perfectly mimics the soil in real life, the installation predictions of the penetration model for the vibro-drill will be very accurate. However, it is very hard to create a model that perfectly represents the soil characteristics. Chapter 3.2 explains how, for the purpose this study, the soil is modelled as a lattice.

3.1.2 Pile/lattice interaction

The goal of establishing the interaction between the pile and the lattice used in this model is to capture the same phenomena as produced by the interaction between a pile and the soil in real life. In real life, a pile will mostly experience friction forces and forces due to displacement of soil. When the vibro-drill is introduced there are other phenomena that have an influence on the interaction. In this case the vibration,

jetting and liquefaction are having an impact on the friction and displacement forces. Chapter 3.3 will be dealing with the calculation of friction and displacement forces and how these forces change when the vibro-drill is introduced.

3.1.3 Vibro-drill

The forcing in this model is generated by the Vibro-drill. The eccentric force of the Vibro-drill would be most effective if it would have the same frequency as the natural frequency of the pile. However, this is not possible because the pile is assumed to be rigid and consequently has no natural frequency. As a consequence, as stated in chapter 3.1, the effects of the eccentric force of the Vibro-drill are simplified. Aside from the forcing the effect of vibrations, jetting and liquefaction on the friction factor is remarkable. Chapter 3.4 explains how the Vibro-drill is incorporated in the model.

3.2 Lattice soil model

Soil can be modelled in various ways. Different aspects of the soil can be captured in different models. As stated in chapter 2.1, the researches of Ben Arntz and Jeroen Keuzenkamp use two elements to model soil characteristics, a spring damper element is used to describe the elastic deformation of the soil and damper friction element is used to describe plastic deformation of the soil. However, this method only describes the soil deformation in one dimension. While this model should be capable of describing the soil deformation in two dimensions.

For this reason a lattice model is used for this research, a well-known practice for modelling soil in a two dimensional way. A lattice can have all kinds of shapes and sizes, the lattice used in this research, however, is built up using point masses, springs and dampers in a hexagonal shape. Each point mass represents the mass and location of a certain volume of soil. The dampers represent the energy that is dissipated when this volume of soil is displaced within the lattice, the springs mimic the elastic deformation of the soil. The equation of motion of a specific mass in the lattice is determined by the boundary conditions and its location within the lattice.

The soil is modelled as a finite two-dimensional domain. At the lower end of this domain, the soil is assumed not to be affected by the installation of the pile. Therefore, at this location the soil is not allowed to move. Hence, it can also be interpreted as a large volume of soil surrounded by walls. Since double symmetry is assumed, only the right half of the domain will be modelled. The soil located at the centreline of the total area (the left edge of the model) is assumed to only move in Z-direction. A visual representation of the creation process of the lattice is shown on the next page in Figure 12.

The goal of the soil model is to accurately mimic the soil characteristics of the different types of soil along the installation depth. The CPT data is used to calculate the model parameters; the masses and spring and damper coefficients. The equations of motion for each mass determines the displacement over time. The following chapters discuss how the model parameters are calculated and how the equations of motion are formed.
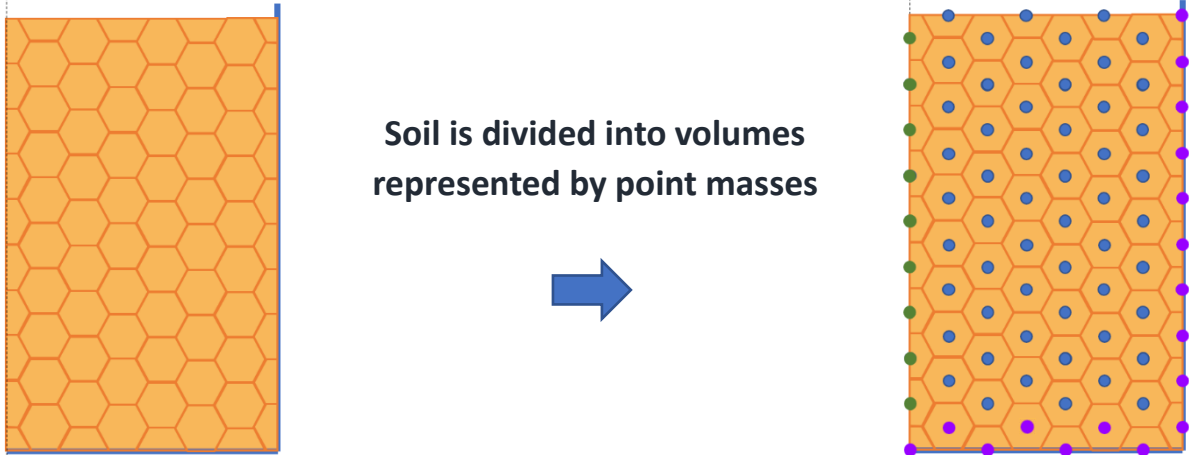
Only right half is modelled due to symmetry
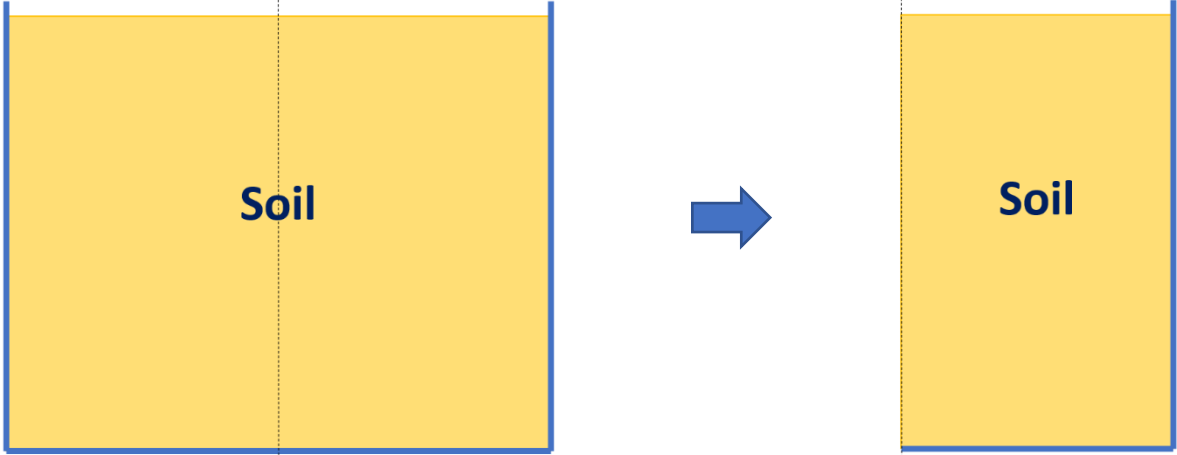
Soil

Soil

Soil is divided into volumes represented by point masses

Springs and dampers are added to simulate soil deformation

Figure 12: Steps from soil to lattice

3.2.1 Correlation between soil and lattice parameters

It is not possible to directly calculate the model parameters from the CPT data. Simply because a correlation between CPT data and the model parameters for a hexagonal lattice does not exist. Soil is commonly described in a continuous form while a lattice model describes the soil in a discrete form. Consequently, a correlation between the more common continuous soil model and the CPT data does exist (P. K. Robertson, 2013), (Peter K Robertson, 2015). Thus, in order to obtain the lattice model parameters, first the continuous soil model parameters need to be calculated with the CPT data. Then the lattice model parameters can be calculated using the continuous soil model parameters. The following two chapters explain how these correlations work and they show the equations used to calculate the parameters.
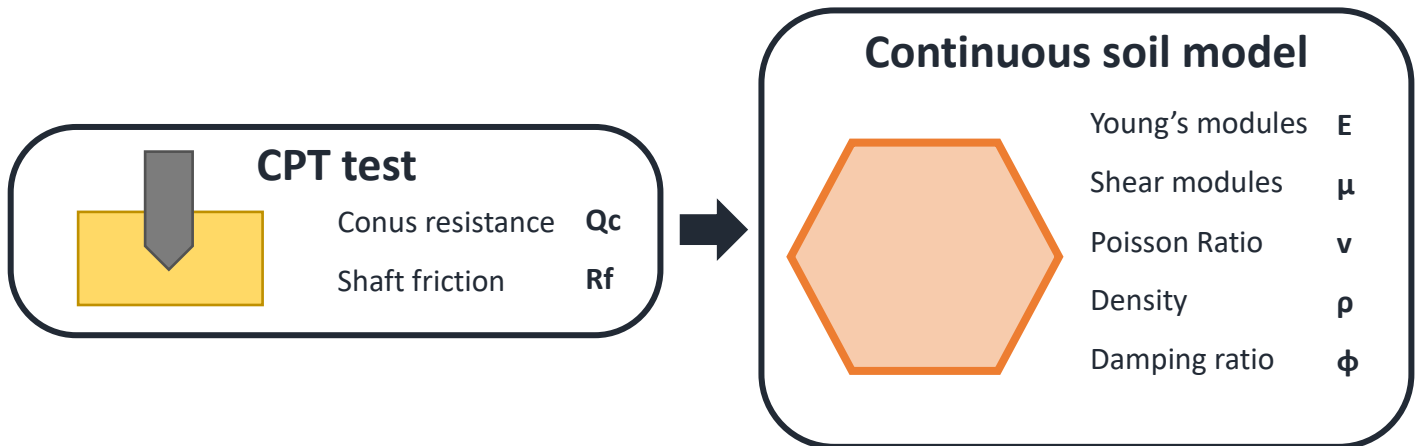

Figure 13: CPT and Continuous soil model parameters

3.2.1.1 CPT data to Continuous soil parameters

As mentioned before, a correlation between the CPT soil data and the continuous soil parameters is used to obtain the model parameters. There are many correlations that can be used but the correlation used in this research is from Robertson. This correlation is also used by Jeroen Keuzenkamp in his graduation thesis (Keuzenkamp, 2017).

Soil type

In the research of (Robertson, et al, 1986) a soil index chart is proposed to determine the type of soil. The chart shows the type of soil for every combination of friction ratio and conus resistance.
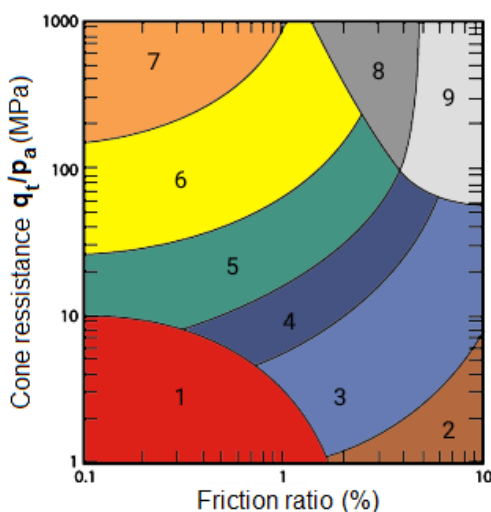
SBT zone	Proposed common SBT description
1	*Sensitive fine-grained*
2	*Clay - organic soil*
3	*Clays: clay to silty clay*
4	*Silt mixtures: clayey silt & silty clay*
5	*Sand mixtures: silty sand to sandy silt*
6	*Sands: clean sands to silty sands*
7	*Dense sand to gravelly sand*
8	*Stiff sand to clayey sand**
9	*Stiff fine-grained**

* Overconsolidated or cemented

Figure 14: Soil types

Young's modulus

The Young's modulus describes the elasticity of the soil. It is quite easily influenced by stress and strain history and soil mineralogy; therefore it is difficult to provide a proper estimation (Peter K Robertson, 2015). In this research it is calculated by multiplying the conus resistance with a certain factor alpha. This factor ranges between 2 and 5 and it depends on the cone resistance. The higher values represent the stronger types of soil and the lower values represent the softer types of soil.

$$E = \alpha \cdot q_c \tag{3.1}$$

However, there is a more sophisticated way to determine the factor alpha. This correlation also incorporates the vertical stress and friction ratio. The Young's modulus is defined as the stiffness of the soil at 0.1% strain. It has to be taken into account that this method can only be used for uncemented predominantly silica sands. This equation depends on I_c, which is the radius of concentric circles that define the soil type boundaries. I_c can assumed to be I_{SBT}, the same circle only now for a non-normalized soil behaviour type index, if the vertical stress is found to be between 50 and 150 kPa (Peter K Robertson, 2010).

$$E = \alpha_E (q_c - \sigma_{vo}) \tag{3.2}$$

$$\alpha_E = 0.015 \left(10^{0.55 \cdot I_c + 1.68} \right) \tag{3.3}$$

I_c is calculated using the tip resistance, the shaft friction and the atmospheric pressure. With I_c the factor alpha can be calculated. Multiplying alpha with tip resistance will eventually provide the Youngs modulus.

$$I_{SBT} = \sqrt{\left(3.47 - \log \frac{q_c}{p_a} \right)^2 + \left(1.22 + \log R_f \right)^2} \tag{3.4}$$

The SBT chart on the right shows the "soil behaviour type" contours.

Poisson's ratio

The Poisson's ratio of soil represents how much the soil expands in directions perpendicular to the direction in which it is compressed, and, vice versa, how much the soil contracts in those directions when it is stretched. For soils usually present at wind farm locations this value usually lies between 0.2 and 0.4. However, when using a hexagonal lattice structure to model the soil, the properties of the lattice cause the Poisson ratio to always remain constant at 0.25. A more elaborate explanation on this matter can be found in chapter 3.2.1.3.

Shear modules

The Shear modules, like the Youngs modulus, is used to describe the elasticity of the soil. It describes the response of the soil to shear stresses and is defined by the ratio between shear stress and the shear strain. The following formula uses the Youngs modules and Poisson ratio to calculate the Shear modules.

$$G = \frac{E}{2(1+v)} \tag{3.5}$$

Density and damping ratio

The density of the soil is assumed to remain the same over the depth of the model at a value of 2000 kg/m3. As to the damping ratio, this is one of the parameters that is used to calibrate the model. Which means that it is an iterative process that determines the value of the damping coefficient, it will not be calculated using the CPT data. The damping ratio is an input parameter of the model and determines the ratio between the damping coefficient and the critical damping.
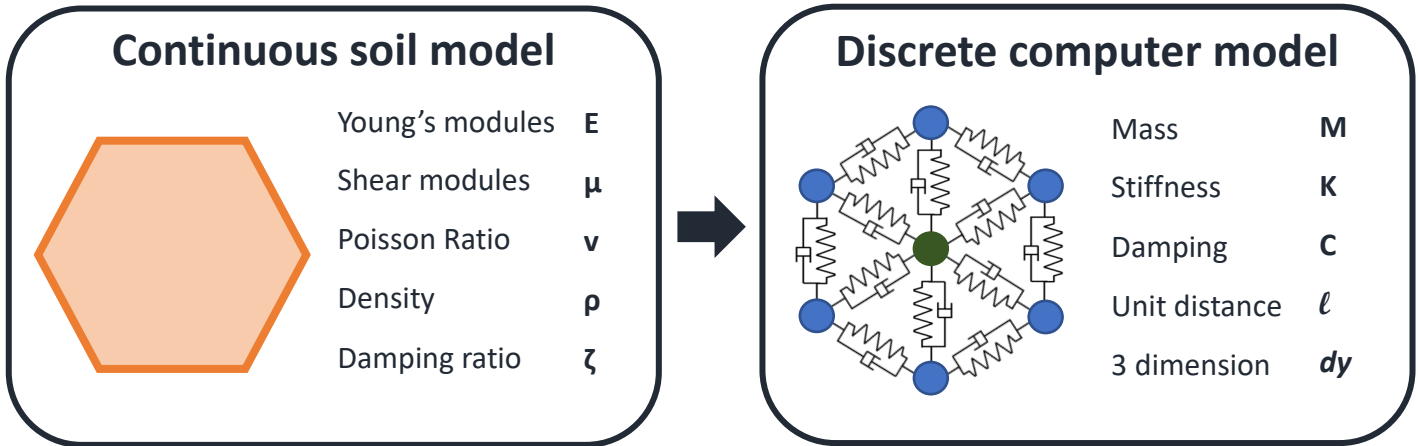

Figure 15: Continuous soil model and discrete computer model parameters

3.2.1.2   Continuous soil parameters to lattice model parameters

Now that the elastic moduli that describe the soil are known they can be used to calculate the lattice model parameters. As mentioned in chapter 3.2 a lattice uses masses which are connected by springs and dampers to describe the soil. Consequently, relations for the mass, the spring and the damper coefficient need to be found.

Mass, Unit distance and 3de dimension

Since the mass of a particle inside the lattice represents a certain volume of soil, the mass itself is calculated by multiplying this volume with the density of the soil. The volume of the soil is defined by the Unit distance (ℓ), the distance between two masses, and the length of the model in the 3de dimension (dy), the dimension in which no displacement takes place. Both these parameters are input parameters, meaning they are chosen, not calculated. The Unit distance determines the resolution of the lattice. Changing the 3de dimension (dy) doesn't really have an influence on the outcome of the model, therefore it is chosen to be 1.

$$M = \tfrac{\sqrt{3}}{2}\rho\ell^2 dy$$

$$V = \tfrac{\sqrt{3}}{2}\ell^2 dy$$
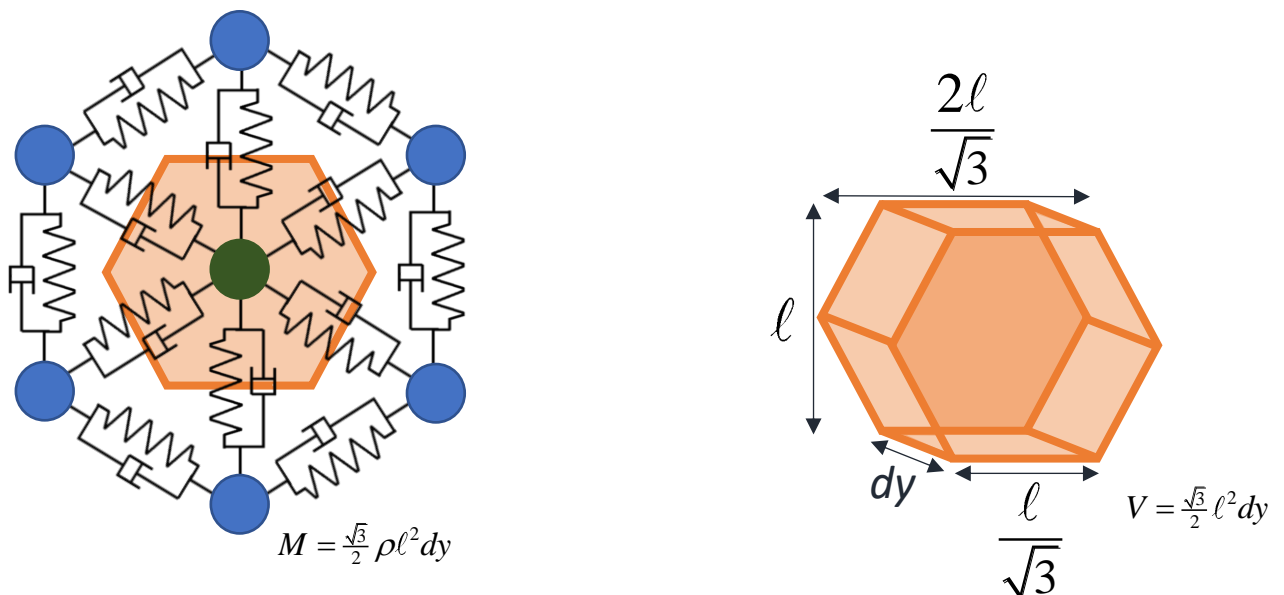
Stiffness

To obtain relations between the kinematic properties of the hexagonal lattice and the macro-material properties, the equations of motion of a particle in the homogeneous hexagonal lattice must, in the long-wave limit, reduce to the equations motion for a corresponding two-dimensional continuum (Maradudin et al., 1963), (Suiker, 2001). If this is done correctly the following relation is obtained:

$$\lambda = \mu = \frac{\sqrt{3}}{4} \frac{K}{dy} \tag{3.6}$$

Two things are interesting about this relation. First two parameters are introduced, called the Lamé constants λ and μ, in which the second Lamé operator μ is equal to the Shear modulus. They follow from the equations of motion for a two-dimensional continuum and describe the elastic properties of the soil through the Young's modulus E and the Poisson's ratio v.

$$\lambda = \frac{vE}{(1-2v)(1+v)} \tag{3.7}$$

$$\mu = \frac{E}{2(1+v)} = G \tag{3.8}$$

Second, the relation shows that the parameters are equal. Consequently, for a hexagonal lattice, this relation only holds if the Poisson's ratio is equal to ¼. Additionally the Lamé operators relates only to the Young's modulus.

$$\lambda = \mu = \tfrac{2}{5} E \tag{3.9}$$

Using these relations the stiffness coefficient K can now be expressed in the Young's modulus and the 3de dimension.

$$K = E \frac{8}{2\sqrt{3}} dy \tag{3.10}$$

Damping

To obtain the relation for the Damping coefficient, the relations for the critical damping and the natural frequency of a hexagonal lattice are used.

$$w_n = \sqrt{\frac{3K}{m}} \tag{3.11}$$

$$c_c = \tfrac{2}{3} m w_n = \tfrac{2}{3}\sqrt{3Km} \tag{3.12}$$

The damping ratio is defined as the ratio between the damping coefficient and the critical damping. The damping ratio is one of the inputs of the model, if it is multiplied with the critical damping, the damping coefficient for the model is obtained.

$$\xi = \frac{C}{c_c} \tag{3.13}$$

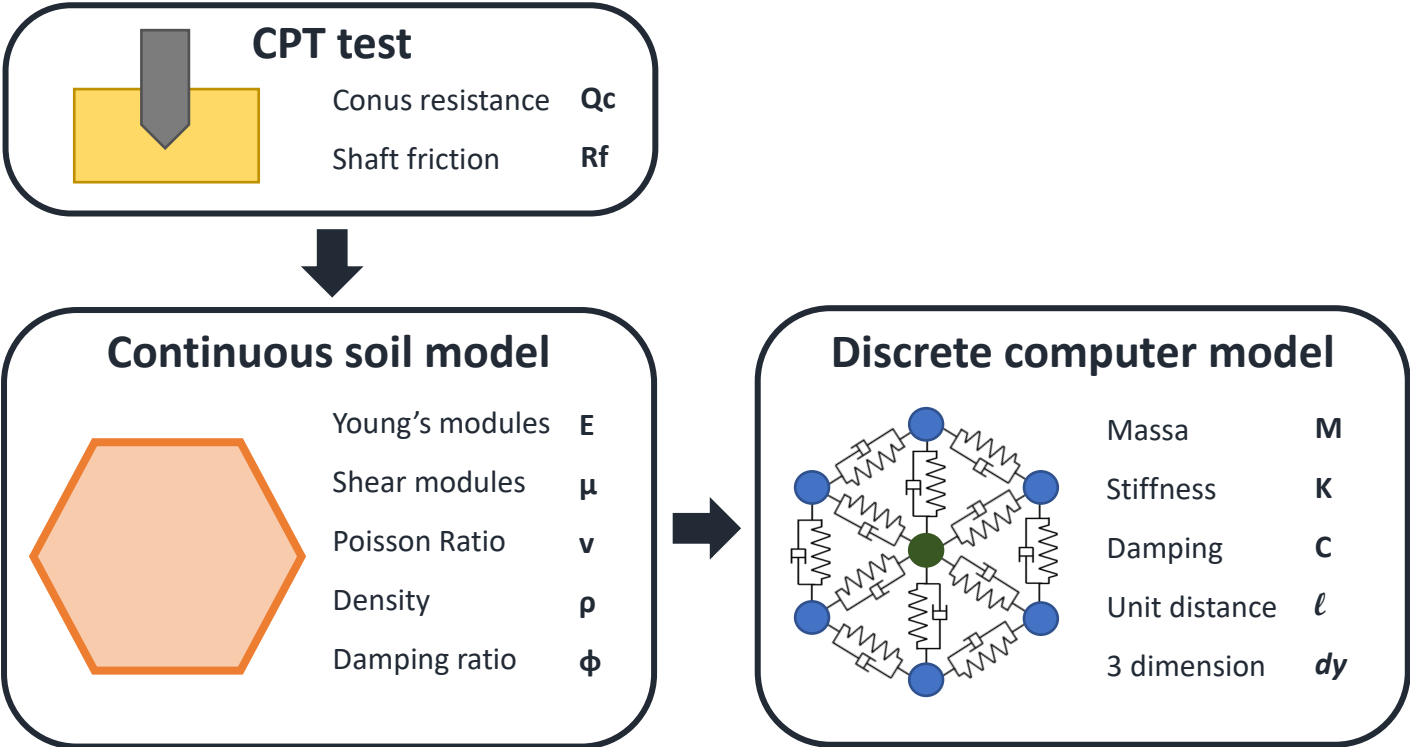$$C = \xi \cdot c_c = \tfrac{2}{3}\sqrt{3Km} \tag{3.14}$$

Figure 16: Flowchart from CPT to Discrete computer model

3.2.2 Equations of Motion for the lattice model

As discussed in chapter 3.2 the soil is divided into certain volumes of soil, each volume is represented by a node. The EOM of a node describes the displacement, velocity, acceleration and the direction in which each of these three phenomena occur at the exact location of this node. The node is located in the centre of gravity of the volume of soil, which means that the displacements of the total soil volume is only captured at certain points (the nodes) inside the total soil volume each representing its own smaller volume. Each node is connected to surrounding nodes by means of a spring/dashpot element. The angle under which the element is located relative to the node is applied in the EOM to describe the contribution of the spring and dashpot in X- and Z-direction. The spring and dashpot recreate the energy necessary to displace a node relative to another node. For each type of soil this energy is different, and since this model assumes non-uniform soil the spring and damper constants will change for each element.

All of the events described above play an important role in generating the EOM and thus have a big impact on the results of the model. The parameters of the model must be chosen in such a way that they provide an EOM that will accurately describe the displacement of the soil and subsequently generate realistic results for our model. The process of finding the correct parameters is further elaborated on in chapter 3.2.1.

The location of the node within the lattice plays an important role in generating the EOM for that specific node. Each node will be assigned one of 5 different categories: free nodes, edge nodes, interface nodes, pile nodes and tip nodes. For every case the direction in which the node is allowed to move is different, as a result the EOM is different. To determine which node can be assigned to a certain category a detection algorithm is used, this detection algorithm is explained in chapter 3.2.4. First, the general equation of motion for a node in a hexagonal lattice will be derived.

The configuration for which the EOM is derived is shown in Figure 18. The OEM describes the displacement of the inner node (node m,n) in either X- or Z- direction. It depends on the elongations of the spring/dashpot elements, which depend on both the displacement of the node m,n for which the EOM is derived and the node attached to the other side of the element. The angle of the element relative to the positive x-axis from the middle of the node determines its contribution to the displacement. The angle for node m+1,n+1 is shown in Figure 18.
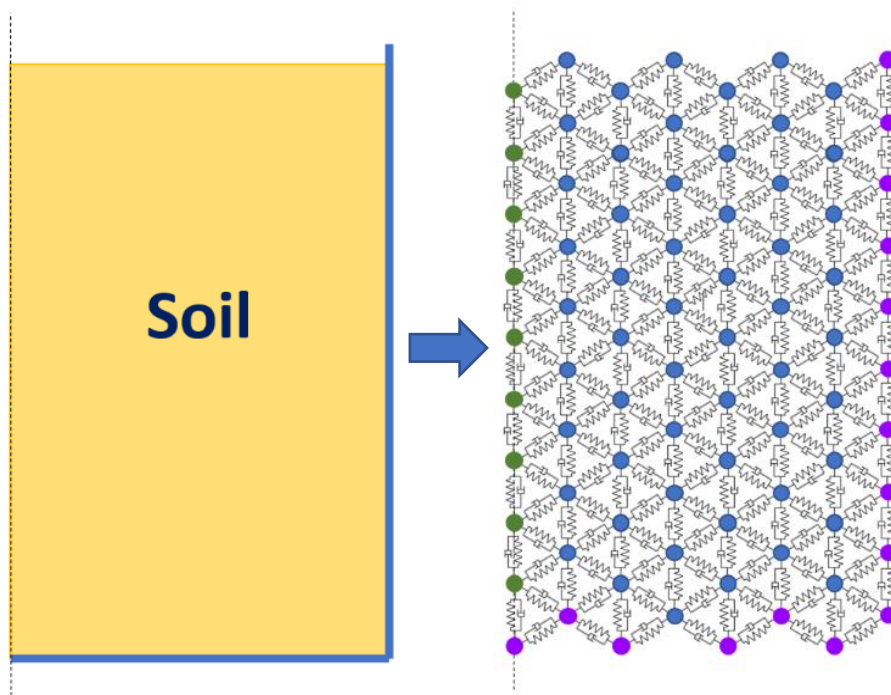

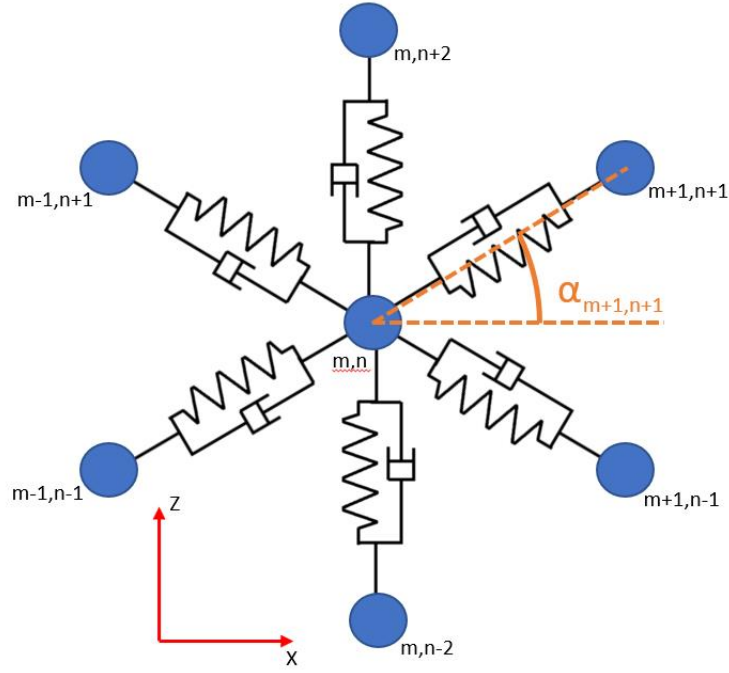*Figure 17: From soil to lattice*

Figure 18: Configuration for node on the inside of lattice

The actual derivation is performed using the Euler-Lagrange method. For this method, first the kinetic and potential energy of the system need to be obtained. The kinetic energy is given by:

$$E_{kin} = \tfrac{1}{2}m(\dot{u}_x)^2 + \tfrac{1}{2}m(\dot{u}_z)^2 \tag{3.15}$$

In which $\mathring{u}_x$ and $\mathring{u}_z$ are the velocities in X- and Z-direction for the center node m,n and m is its mass. The potential energy is found as:

$$E_{pot} = \sum_{j=1}^{6} \tfrac{1}{2}\hat{K}_j(e_j)^2 \text{ , where } \hat{K}_j = K_j + \frac{d}{dt}C_j \tag{3.16}$$

In which e is the elongation of the spring/dashpot element and k is the combined spring constant which contains the spring constant itself and the time derivative of "u" multiplied by the damping constant. This is done to simplify the EOM by getting rid of ů. J in the summation runs from 1 to 6, for all the springs.

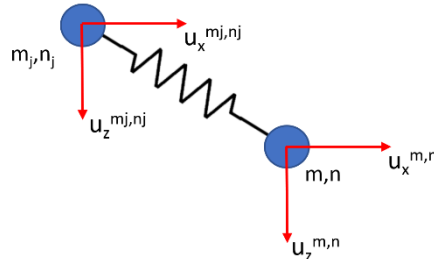*Figure 19: Elongation of element*

Elongation:

$$e_j = e_x^j \cos\alpha^{m_j,n_j} + e_z^j \sin\alpha^{m_j,n_j} \tag{3.17}$$

Linearized elongation:

$$e_j = \left(u_x^{m_j,n_j} - u_x^{m,n}\right)\cos\alpha^{m_j,n_j} + \left(u_z^{m_j,n_j} - u_z^{m,n}\right)\sin\alpha^{m_j,n_j} \tag{3.18}$$

The elongation of the springs is linearized to eliminate second order values from the differential equation. Consequently the EOM only holds for small strains/displacements. The effects this assumption has on the results is discussed in chapter 5. The elongation is inserted in the equation for the potential energy.

$$E_{pot} = \tfrac{1}{2}\sum_{j=1}^{6}\hat{K}_j\left(\left(u_x^j - u_x\right)\cos\alpha_j + \left(u_z^j - u_z\right)\sin\alpha_j\right)^2 \tag{3.19}$$

And the square brackets are solved.

$$E_{pot} = \tfrac{1}{2}\sum_{j=1}^{6}\hat{K}_j\left(\begin{array}{l}\left(u_x^j - u_x\right)^2\cos^2\alpha_j + \left(u_z^j - u_z\right)^2\sin^2\alpha_j \\ +2\left(u_x^j - u_x\right)\left(u_z^j - u_z\right)\cos\alpha_j\sin\alpha_j\end{array}\right) \tag{3.20}$$

Eventually the potential and kinetic energy can be inserted in the Lagrangian equation.

$$L = E_{kin} - E_{pot} \tag{3.21}$$

$$L = \tfrac{1}{2}m\left(\dot{u}_x\right)^2 + \tfrac{1}{2}m\left(\dot{u}_z\right)^2 - \tfrac{1}{2}\sum_{j=1}^{6}\hat{K}_j\left(\begin{array}{l}\left(u_x^j - u_x\right)^2\cos^2\alpha_j + \left(u_z^j - u_z\right)^2\sin^2\alpha_j \\ +2\left(u_x^j - u_x\right)\left(u_z^j - u_z\right)\cos\alpha_j\sin\alpha_j\end{array}\right) \tag{3.22}$$

Now the Lagrangian equation is used in the Euler-Lagrange formula to find both EOMs.

$$\frac{\partial L}{\partial u_{x/z}} - \frac{\partial}{\partial t}\frac{\partial L}{\partial \dot{u}_{x/z}} = 0 \tag{3.23}$$

For X-direction:

$$\frac{\partial\left(-\tfrac{1}{2}\sum_{j=1}^{6}\hat{K}_j\left(\begin{array}{l}\left(u_x^j - u_x\right)^2\cos^2\alpha_j + \left(u_z^j - u_z\right)^2\sin^2\alpha_j \\ +2\left(u_x^j - u_x\right)\left(u_z^j - u_z\right)\cos\alpha_j\sin\alpha_j\end{array}\right)\right)}{\partial u_x} - \frac{\partial}{\partial t}\frac{\partial\left(\tfrac{1}{2}m\left(\dot{u}_x\right)^2 + \tfrac{1}{2}m\left(\dot{u}_z\right)^2\right)}{\partial \dot{u}_x} = 0 \tag{3.24}$$

$$m\ddot{u}_x + \tfrac{1}{2}\sum_{j=1}^{6}\frac{\hat{K}_j}{\partial u_x}\left(\left(u_x^j - u_x\right)^2\cos^2\alpha_j + 2\left(u_x^j - u_x\right)\left(u_z^j - u_z\right)\cos\alpha_j\sin\alpha_j\right) = 0 \tag{3.25}$$

And for Z-direction:

30

$$\frac{\partial\left(-\frac{1}{2}\sum_{j=1}^{6}\hat{K}_j\left(\begin{array}{c}\left(u_x^j-u_x\right)^2\cos^2\alpha_j+\left(u_z^j-u_z\right)^2\sin^2\alpha_j\\+2\left(u_x^j-u_x\right)\left(u_z^j-u_z\right)\cos\alpha_j\sin\alpha_j\end{array}\right)\right)}{\partial u_z}-\frac{\partial}{\partial t}\frac{\partial\left(\frac{1}{2}m\left(\dot{u}_x\right)^2+\frac{1}{2}m\left(\dot{u}_z\right)^2\right)}{\partial\dot{u}_z}=0 \qquad (3.26)$$

$$m\ddot{u}_z+\frac{1}{2}\sum_{j=1}^{6}\frac{\hat{K}_j}{\partial u_z}\left(\left(u_z^j-u_z\right)^2\sin^2\alpha_j+2\left(u_x^j-u_x\right)\left(u_z^j-u_z\right)\cos\alpha_j\sin\alpha_j\right)=0 \qquad (3.27)$$

During every timestep of the simulation the angle alpha is updated. Therefore, the EOMs are always changing. This also means that the linearization for the elongation can still hold. By constantly updating the EOM, the displacements relative to the previous time step stays small. If the nodes would be in the start position of the simulation they will have the arrangement of Figure 18 and the EOMs will look as followed:

$$m\ddot{u}_x+\hat{K}\left(\begin{array}{c}3u_x^{m,n}-\frac{3}{4}\left(u_x^{m+1,n-1}+u_x^{m-1,n-1}+u_x^{m-1,n+1}+u_x^{m+1,n+1}\right)\\+\frac{1}{4}\sqrt{3}\left(u_z^{m+1,n-1}-u_z^{m-1,n-1}+u_z^{m-1,n+1}-u_z^{m+1,n+1}\right)\end{array}\right)=0 \qquad (3.28)$$

$$m\ddot{u}_z+\hat{K}\left(\begin{array}{c}3u_z^{m,n}-u_z^{m,n-2}-u_z^{m,n+2}-\frac{1}{4}\left(u_z^{m+1,n-1}+u_z^{m-1,n-1}+u_z^{m-1,n+1}+u_z^{m+1,n+1}\right)\\+\frac{1}{4}\sqrt{3}\left(-u_x^{m+1,n-1}+u_x^{m-1,n-1}-u_x^{m-1,n+1}+u_x^{m+1,n+1}\right)\end{array}\right)=0 \qquad (3.29)$$

Now that it is known how the EOM is derived, there is a need to look into the difference in EOM for each category within the lattice. Figure 20 shows the possible configurations and there allowed movements. Then, for each category there is explained how the OEMs are formed and finally Figure 20 shows the configurations and their EOMs combined.
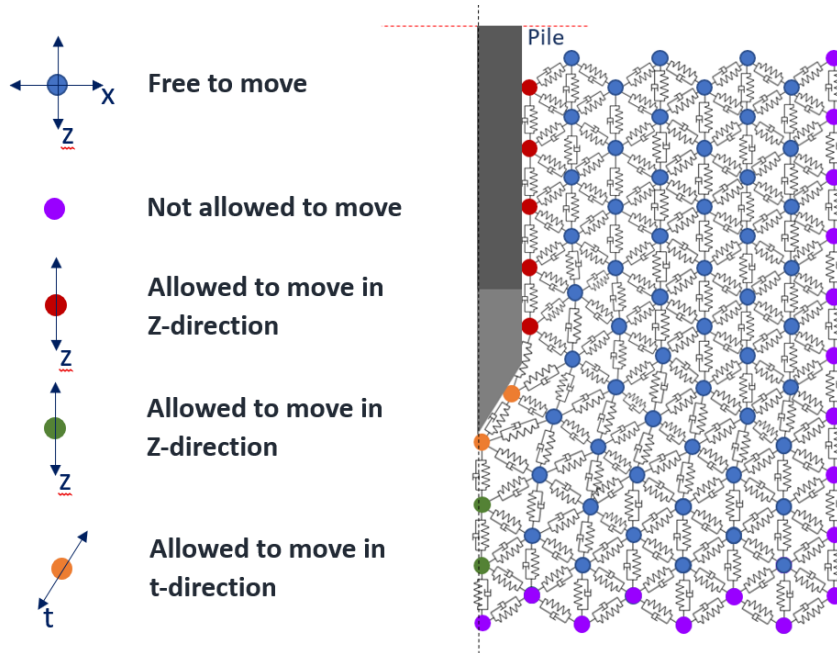

Figure 20: Possible configurations regarding the displacements of nodes

3.2.2.1 Free nodes

Nodes on the interior of the lattice are not restricted by anything, they are free to move in X- and Z-direction. For this reason they have an EOM in both X- and Z-direction. Such nodes can have three configurations. The majority has the first configuration, they are completely surrounded by other nodes. But at the top edge of the lattice there are two other possible configurations, each with their own EOM's. These configurations and EOM's are shown below.
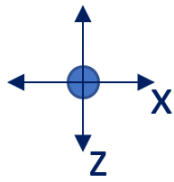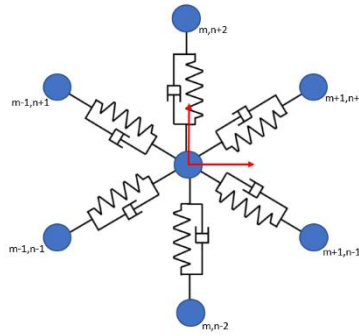
$$\ddot{u}_x = -\tfrac{1}{2}\sum_{j=1}^{6}\frac{\hat{K}_j}{\partial u_x \cdot m}\left(\left(2u_x - 2u_x^j\right)^2 \cos^2\alpha_j + 2\left(u_z - u_z^j\right)\cos\alpha_j\sin\alpha_j\right)$$

$$\ddot{u}_z = -\tfrac{1}{2}\sum_{j=1}^{6}\frac{\hat{K}_j}{\partial u_z \cdot m}\left(\left(2u_z^j - 2u_z\right)\sin^2\alpha_j + \left(2u_z^j - u_z\right)\cos\alpha_j\sin\alpha_j\right)$$
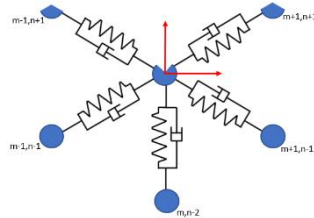
Figure 21: Free node EOMs

Configuration 1:

$$m\ddot{u}_x + \hat{K}\left(3u_x^{m,n} - \tfrac{3}{4}\left(u_x^{m+1,n-1} + u_x^{m-1,n-1} + u_x^{m-1,n+1} + u_x^{m+1,n+1}\right) + \tfrac{1}{4}\sqrt{3}\left(u_z^{m+1,n-1} - u_z^{m-1,n-1} + u_z^{m-1,n+1} - u_z^{m+1,n+1}\right)\right) = 0$$

$$m\ddot{u}_z + \hat{K}\left(3u_z^{m,n} - u_z^{m,n-2} - u_z^{m,n+2} - \tfrac{1}{4}\left(u_z^{m+1,n-1} + u_z^{m-1,n-1} + u_z^{m-1,n+1} + u_z^{m+1,n+1}\right) + \tfrac{1}{4}\sqrt{3}\left(-u_x^{m+1,n-1} + u_x^{m-1,n-1} - u_x^{m-1,n+1} + u_x^{m+1,n+1}\right)\right) = 0$$
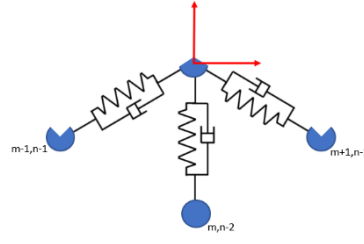

Configuration 2:

$$\tfrac{2}{3}m\ddot{u}_x + \hat{K}\left(\tfrac{9}{4}u_x^{m,n} - \tfrac{3}{4}\left(u_x^{m+1,n-1} + u_x^{m-1,n-1} + \tfrac{1}{2}u_x^{m-1,n+1} + \tfrac{1}{2}u_x^{m+1,n+1}\right) + \tfrac{1}{4}\sqrt{3}\left(u_z^{m+1,n-1} - u_z^{m-1,n-1} + \tfrac{1}{2}u_z^{m-1,n+1} - \tfrac{1}{2}u_z^{m+1,n+1}\right)\right) = 0$$

$$\tfrac{2}{3}m\ddot{u}_z + \hat{K}\left(\tfrac{7}{4}u_z^{m,n} - u_z^{m,n-2} - \tfrac{1}{4}\left(u_z^{m+1,n-1} + u_z^{m-1,n-1} + \tfrac{1}{2}u_z^{m-1,n+1} + \tfrac{1}{2}u_z^{m+1,n+1}\right) + \tfrac{1}{4}\sqrt{3}\left(-u_x^{m+1,n-1} + u_x^{m-1,n-1} - \tfrac{1}{2}u_x^{m-1,n+1} + \tfrac{1}{2}u_x^{m+1,n+1}\right)\right) = 0$$

Configuration 3:

$$\tfrac{1}{3}m\ddot{u}_x + \hat{K}\left(\tfrac{3}{4}u_x^{m,n} - \tfrac{3}{8}\left(u_x^{m-1,n+1} + u_x^{m+1,n+1}\right) + \tfrac{1}{8}\sqrt{3}\left(u_z^{m-1,n+1} - u_z^{m+1,n+1}\right)\right) = 0$$

$$\tfrac{1}{3}m\ddot{u}_z + \hat{K}\left(\tfrac{5}{4}u_z^{m,n} - u_z^{m,n-2} - \tfrac{1}{8}\left(u_z^{m+1,n-1} + u_z^{m-1,n-1}\right) + \tfrac{1}{8}\sqrt{3}\left(-u_x^{m+1,n-1} + u_x^{m-1,n-1}\right)\right) = 0$$

3.2.2.2 Edge nodes

The nodes at the lower and right edge of the lattice represent the soil that is not supposed to move. These nodes are the ones that keep the lattice in place. They represent a volume of soil, but since it is not supposed to move it will also have no impact on the model. Only the location of the nodes is relevant. It is used to determine the elongation of the springs connected to nodes that can move.


$$\ddot{u}_x = 0$$
$$\ddot{u}_z = 0$$

Figure 22: Edge nodes EOMs

3.2.2.3 Interface nodes

The interface is defined as the heartline of the model. It is the position at which our model is assumed to be symmetrical. Since the model is symmetrical it can be assumed that the soil on the left side of the pile will behave in the same way as the soil on the right side of the pile. Consequently, only the right side of the soil has to be modelled to generate a valid result. This symmetricity also means that the soil is not allowed to move in X-direction, because if it would, symmetry is lost. The configuration of these nodes is the same as the configuration for the nodes on the pile and the flipper and is shown as configuration 4.
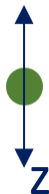
$$\ddot{u}_x = 0$$
$$\ddot{u}_z = -\tfrac{1}{2}\sum_{j=1}^{4} \frac{\hat{K}_j}{\partial u_z \cdot m}\left(\left(2u_z^j - 2u_z\right)\sin^2\alpha_j + \left(2u_z^j - u_z\right)\cos\alpha_j \sin\alpha_j\right)$$

Figure 23: Interface nodes EOMs

3.2.2.4 Pile nodes

The nodes which are located at the side of the pile have a similar situation as the nodes on the interface line. For these nodes it is assumed that they will always stay in contact with the pile. Since the pile does not move in x-direction, the nodes also do not move in x-direction and will therefore only have an equation of motion in z-direction and not in x-direction.
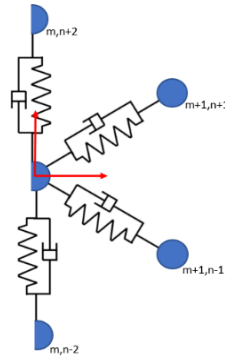
$$\ddot{u}_x = 0$$

$$\ddot{u}_z = -\frac{1}{2}\sum_{j=1}^{4}\frac{\hat{K}_j}{\partial u_z \cdot m}\left(\left(2u_z^j - 2u_z\right)\sin^2\alpha_j + \left(2u_z^j - u_z\right)\cos\alpha_j\sin\alpha_j\right)$$

Figure 24: Pile nodes EOMs

Configuration 4:

$$\frac{1}{2}m\ddot{u}_x + \hat{K}\left(\frac{3}{2}u_x^{m,n} - \frac{3}{4}\left(u_x^{m+1,n-1} + u_x^{m+1,n+1}\right) + \frac{1}{4}\sqrt{3}\left(u_z^{m+1,n-1} - u_z^{m+1,n+1}\right)\right) = 0$$

$$\frac{1}{2}m\ddot{u}_z + \hat{K}\left(\frac{3}{2}u_z^{m,n} - \frac{1}{2}u_z^{m,n-2} - \frac{1}{2}u_z^{m,n+2} - \frac{1}{4}\left(u_z^{m+1,n-1} + u_z^{m+1,n+1}\right) + \frac{1}{4}\sqrt{3}\left(-u_x^{m+1,n-1} + u_x^{m+1,n+1}\right)\right) = 0$$

3.2.2.5 Tip nodes

Let us consider the interaction between the lattice and the tip. Just as on the interface and along the pile, the nodes are assumed to be attached to the tip surface. They are only allowed to move along the length of the tip. However, unlike at the interface or the pile, the direction in which the node is allowed to move cannot be expressed in one X- or Z-direction. Thus the solution is not as simple as eliminating one of the EOMs. Therefore the same approach as the research of O. Dorival is used (Dorival, 2008). A local coordinate system is introduced in which **n** is the direction perpendicular to the tip surface and **t** the direction parallel to the tip surface. Using this local coordinate system, now the direction in which the node is allowed to move can be expressed in one direction, namely, the t-direction. And, consequently, the node is not allowed to move in n-direction.

The unilateral contact equations below are used to model the contact situation. Two situations are considered. The first being static friction, this only occurs when the node is not moving, hence, static. If the node is not allowed to move, it will not move in either t- nor n-direction. If the node experiences kinetic friction, the contact equation for t-direction depends on both the EOM in X- and Z-direction.

Static friction:

$$\ddot{\mathbf{u}} \cdot \mathbf{n} = 0 \tag{3.30}$$

$$\ddot{\mathbf{u}} \cdot \mathbf{t} = 0 \tag{3.31}$$

Kinetic friction:

$$\underline{\underline{m}}\,\underline{\ddot{\mathbf{u}}} \cdot \underline{\mathbf{n}} = 0 \tag{3.32}$$

$$\underline{\underline{m}}\,\ddot{\mathbf{u}} \cdot \underline{\mathbf{t}} = \left(\underline{\mathbf{f}}^{\,\text{ext}} + \underline{\mathbf{f}}^{\,\text{int}}\right) \cdot \underline{\mathbf{t}} \tag{3.33}$$

n and t are actually vectors that represent the contribution of a displacement in X- and Z-direction to n- or t-direction.

$$\underline{\mathbf{n}} = \begin{bmatrix} \cos(\alpha) & -\sin(\alpha) \end{bmatrix} \tag{3.34}$$

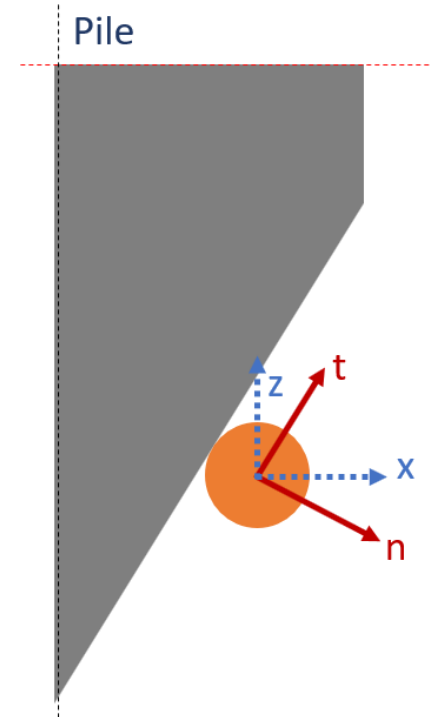$$\underline{\mathbf{t}} = \begin{bmatrix} \sin(\alpha) & \cos(\alpha) \end{bmatrix} \tag{3.35}$$

Figure 25: Global axis system for node at tip

ü and (f^ext + f^int) are vectors that represent the ordinary EOMs in X- and Z-direction. With m being the mass matrix.

$$\underline{\ddot{\mathbf{u}}} = \begin{bmatrix} \ddot{u}_x \\ \ddot{u}_z \end{bmatrix} \tag{3.36}$$

$$\left(\underline{\mathbf{f}}^{\,\text{ext}} + \underline{\mathbf{f}}^{\,\text{int}}\right) = \begin{bmatrix} F_{ext,x} - C \cdot \dot{u}_x - K \cdot u_x \\ F_{ext,z} - C \cdot \dot{u}_z - K \cdot u_z \end{bmatrix} \tag{3.37}$$

If these vectors are substituted in the contact equations […] the EOM for X- and Z- direction can be obtained.

$$M\ddot{u}_x \cdot \cos\beta + M\ddot{u}_z \cdot -\sin\beta = 0$$

$$M\ddot{u}_x \cdot \sin\beta + M\ddot{u}_z \cdot \cos\beta = \left(F_{ext,x} - F_{i,x}\right)\sin\beta + \left(F_{ext,z} - F_{i,z}\right)\cos\beta$$

If these equations are solved for ü$_x$ and ü$_z$ it provides the EOM in X- and Z-direction. It can be observed that both EOMs depend on displacements in both directions. Which makes sense, if the node is only allowed to move in the t-direction, for every displacement in X-direction there is a corresponding displacement in Z-direction. Only than the contact equation can be satisfied.

$$\ddot{u}_x = \frac{\sin^2\beta}{M}\left(F_{ext,x} - F_{i,x}\right) + \frac{\cos\beta\sin\beta}{M}\left(F_{ext,z} - F_{i,z}\right)$$
$$\ddot{u}_z = \frac{\cos\beta\sin\beta}{M}\left(F_{ext,x} - F_{i,x}\right) + \frac{\cos^2\beta}{M}\left(F_{ext,z} - F_{i,z}\right)$$

Figure 26: Tip nodes EOMs

Now that for each category the EOMs are known, in Figure 20 an overview is provided that summarizes the location, the movement and the EOM for each specific category.

3.2.3 Pile-imposed displacement

When the node is at the interface or at the shaft of the pile it can move in Z-direction. The displacement for each timestep is calculated by the solver. The solver provides a displacement in Z-direction, the same direction in which the node is allowed to move. However, as soon as the node is at the tip surface this changes. Now the node is only allowed to move in t-direction, while the solver only provides a displacement in X- or Z-direction. As a result the displacement in X-direction depends on the displacement in Z-direction to satisfy the displacement in t-direction.

In reality the node will want to move in directions other than just the t-direction. To account for this a pile-imposed displacement is introduced which takes place between each timestep of the solver. Within the model this displacement depends on the penetration of the pile, hence the name pile-imposed displacement. As the pile moves down it displaces the nodes in n-direction. This displacement is added up to the results of the previous solver timestep and afterwards used as the initial conditions for the next solver time step. This process continues until the node reaches the pile shaft. In Figure 27 this process is shown for one node.
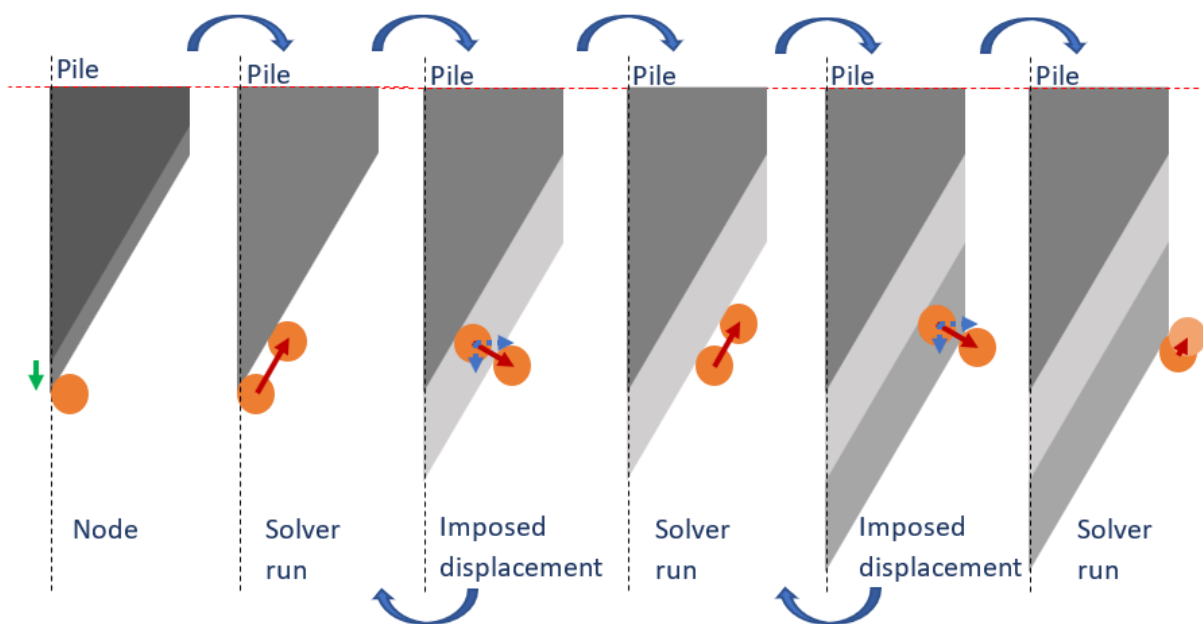

Figure 27: Solver and pile imposed displacement process

As stated above, the pile-imposed displacement is calculated using the penetration of the pile. But in fact there is a lot more required to calculate this displacement.
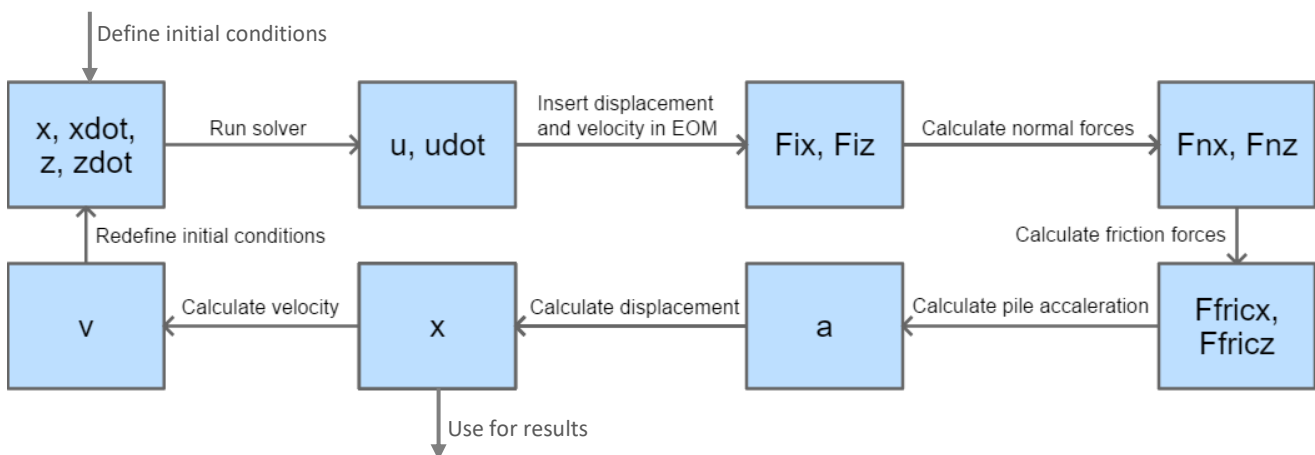

Figure 28: Order in which pile-imposed displacement parameters are calculated

First the initial conditions for the solver need to be defined. Afterwards the solver will provide the displacement and velocity for the node in X- and Z-direction. These are then used in the equation of motion to calculate the internal forces.

$$m\ddot{\mathbf{u}} \cdot \mathbf{n} = \left(\mathbf{f}^{\text{ext}} + \mathbf{f}^{\text{int}}\right) \cdot \mathbf{n} = 0 \tag{3.40}$$

$$M\ddot{u}_x \cdot \cos\beta + M\ddot{u}_z \cdot -\sin\beta = \left(F_{ext,x} - F_{i,x}\right)\cos\beta + \left(F_{ext,z} - F_{i,z}\right)\sin\beta = 0 \tag{3.41}$$

$$F_{ext,x} - F_{i,x} = F_{ext,z} - F_{i,z} = 0 \tag{3.42}$$

$$F_{i,x} = C \cdot \dot{u}_x + K \cdot u_x \tag{3.43}$$

$$F_{i,z} = C \cdot \dot{u}_z + K \cdot u_z \tag{3.44}$$

Using the internal forces the normal force on the pile is calculated. Which then is used to calculate the friction forces.

$$F_{ext,t} = F_{fric,t} = F_{n,x} \cdot \mu_{fric} \sin\beta + F_{n,z} \cdot \mu_{fric} \cos\beta \tag{3.45}$$

The soil acts on the pile resisting the penetration. This force is called the total soil resistance and is calculated by the sum of the contributions of al the friction forces and the normal forces of each node in Z-direction. A further analysis of the soil resistance is provided in chapter 3.3.

$$F_{soil} = \sum_{i=1}^{n} F_{fric,z} + \sum_{i=1}^{n} F_{n,z} \tag{3.46}$$

n = # nodes into contact with pile

To calculate the actual pile-imposed displacement, first the acceleration and velocity of the pile need to be obtained. Newton's second law is used to calculate the acceleration of the pile. The velocity is calculated after each timestep to be used in the next timestep.

$$a_i = \frac{F_{pile} - F_{fric,total}}{M_{pile}} \tag{3.47}$$

$$\Delta x_i = v_{i-1}t - \frac{1}{2}a_i t^2 \tag{3.48}$$

$$v_i = v_{i-1} + a_i t \tag{3.49}$$

Finally, the pile-imposed displacement is added up to the results from the solver and they become the initial conditions for the next solver run. The external forces calculated in this timestep become the external forces used in the equation of motion for the next time step of the solver.

3.2.4 Detection Algorithm

The output from the solver is used to generate the information that is necessary to advance to the next time step.

This detection algorithm first calculates the location of the pile. It uses the X and Z-coordinates of the nodes from which it is known that they came into contact with the flipper surface in the previous time step.

$$z_{tip} = z_{node} - z_{n,tip} = z_{node} - \frac{x_{node}}{\tan \beta} \qquad (3.50)$$

Than the algorithm looks at the location of the pile and compares it to the location of each node. It appoints the node to one of four categories (interface, flipper, pile or free).

Figure 29: Parameters used in pile location calculation

3.2.5 Randomization

As Jeroen Hoving states in his research (Hoving, 2019): *"To capture the physics of nonlinear material behaviour, the random heterogeneity of the considered material must be accounted for. Absence of this randomness in a two- or three-dimensional lattice yields a significant mesh dependency in its nonlinear response as any occurring nonlinear phenomena will propagate along the directions privileged by the regular mesh, thereby losing the unstructured character of nonlinear material behaviour."*. In other words, a randomized lattice captures the nonlinear soil phenomena and is therefore a more realistic way for modelling soil.

This model incorporates the randomness by changing the initial location of each node on the inside of a regular mesh. It does this by randomly choosing two values. The first is the angle alpha and lays between 0° and 360° and the second is the length ℓ which lays between 0 and 1/3L. The maximum value of 1/3 L for ℓ is assumed so that the smallest distance between two nodes will always be larger than 1/3.
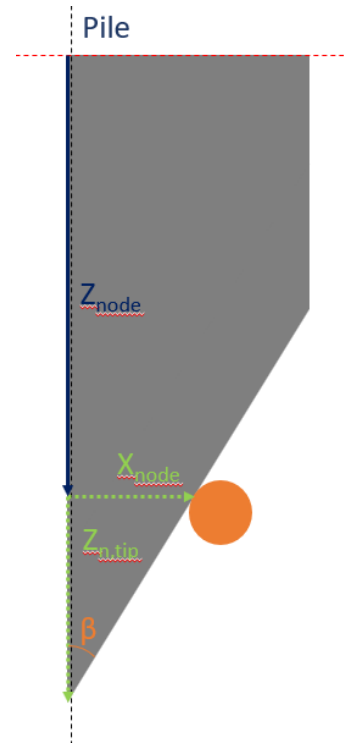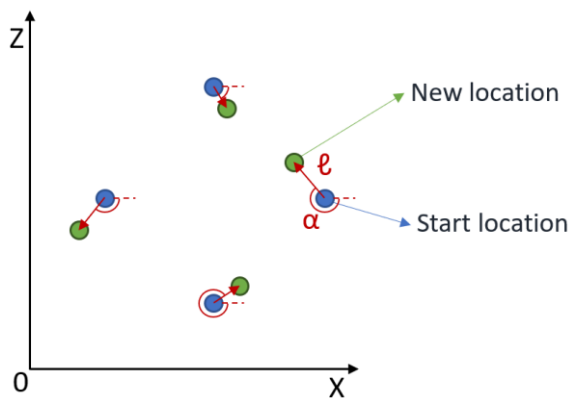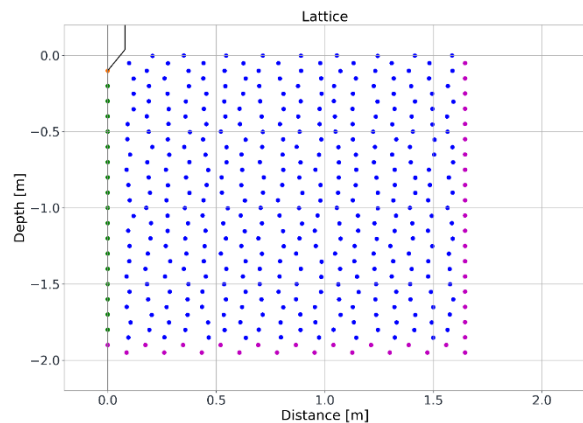

Figure 31: Randomization process

Figure 30: Randomized lattice

3.2.6 Lattice resolution

The size and resolution of the lattice have a considerable influence on the results of the model, as shown in chapter 4.5. The size of the lattice is depicted by the width and depth of the modelled soil. It is defined as the number of nodes in each direction, n states the number of nodes in the Z-direction (depth), m states the number of nodes in X-direction (width).

The resolution of the lattice determines the amount of locations at which the displacement of the soil is described. A high resolution means more data points to describe the soil displacement which results in a higher accuracy of the outcome of the model, but also means more computation time. A low accuracy means less data points in which the soil displacement is described, thus a lower accuracy of the outcome, but a faster computation time. In chapter 0 a sensitivity analysis is executed to determine the optimal resolution and lattice size at which the model provides accurate results within an acceptable computation time.

As stated in chapter 0. the unit distance describes the distance between two nodes; therefore it is used as the input parameter for the resolution of the model. The unit distance also effects the size of the lattice. Together with n and m it defines the depth and width of the modelled soil.
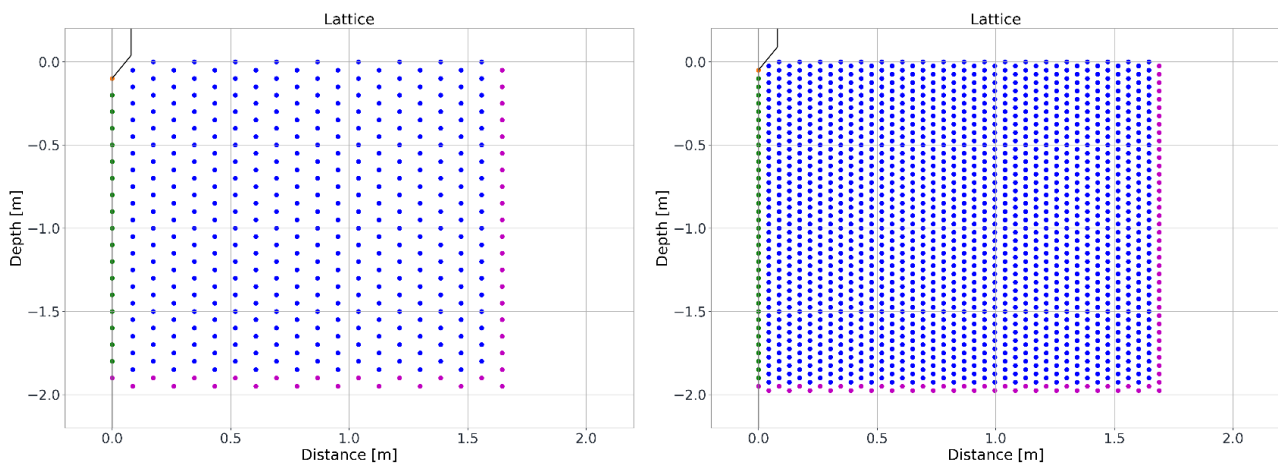

Figure 32: Two lattice configurations with different resolutions

3.3 Pile/lattice interaction

As soon as the pile and the lattice come into contact with each other, energy transfer takes place. The downward motion of the pile displaces the lattice, in this process the pile exerts a force on the lattice and vice versa. Everything that happens between the pile and lattice is captured in the model as the "pile/lattice interaction". This chapter explains what kind of forces are involved in this interaction and how these forces are calculated. These forces are divided into two categories, the forces at the tip of the pile, and forces along the shaft of the pile.

The forces that are generated at the shaft are dominated by the friction force between the nodes and the pile. The Vibro-drill has an impact on this friction force. The forces at the tip are similar to the forces at the shaft, but now there is also a compression force present and everything is at an angle.

3.3.1 Shaft friction

The pile is modelled as a rigid bod which is only allowed to move in Z-direction. The nodes at the shaft of the pile are assumed to be stuck to the shaft, therefore, they are not allowed to move in X-direction. As a result, the displacement of the lattice will either cause a pull or push force in X-direction on the pile, called the normal force. The direction of the normal force is transverse to the penetration direction of the pile. Thus the normal force itself does not have an effect on the penetration. However, friction is assumed to be present between the nodes and the shaft. As a consequence, the normal force will cause a friction force in Z-direction. These forces do contribute to the pile penetration.

3.3.1.1 Normal force and relative velocity

The friction force is calculated by multiplying the normal force with the friction factor. The magnitude of the normal force determines the magnitude of the friction force. However, when the normal force is pointing in the direction away from the pile, there is no energy transfer from the node to the pile and thus no friction force.

Figure 33: Free body diagram of different shaft friction configurations

The direction of the friction force is determined by the relative velocity of the node to the pile. If the relative velocity of the node is in positive Z-direction, the friction force on the pile will act in the same direction and vice versa.

A free body diagram of each of these situations is shown in Figure 33.

3.3.1.2 Friction factor

The friction factor plays an important role in the friction force calculation. It is the only input parameter in this calculation, and as such the only way to manipulate the friction force, assuming the lattice properties remain unchanged.

A lot of research has been done regarding friction along the shaft of the pile while it is being installed with a hydraulic hammer. The urge to find a quieter installation method resulted in more and more research towards the effects of vibratory hammering on the friction force along the shaft. The results show that certain vibrations are very effective in reducing friction. Vibrations in the longitudinal direction of the pile are most effective if the frequency of these vibrations are close to the eigenfrequencies of the pile in the soil. The research results could also be very promising if the pile is excited in torsional direction.
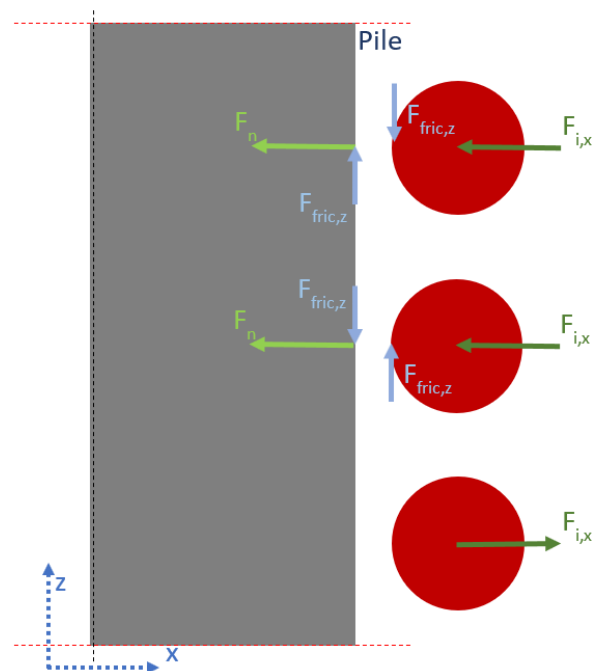
The Vibro-drill also uses vibrations, but they are induced on the bottom of the monopile, instead of on the top as is the case with the existing vibratory hammer. Currently there is no published research of the effect of vibrations on the friction along the shaft, if excited at the bottom. Therefore, the assumption is that it will have a similar effect as vibrating on the top of the monopile and it will consequently reduce the friction.

The model assumes symmetry, as a result only one outside half of the pile is modelled. Although the monopile can be assumed to be symmetrical, the friction forces on either side of the monopile are not symmetrical. A key feature of the Vibro-drill is to liquefy the soil inside the pile. This drastically reduces the friction on the inside of the pile compared to the outside. The model accounts for this by averaging the friction factor on the outside and inside.

An exact value for the friction factor is impossible to obtain at the moment. However, in chapter 0 the effect of the friction factor is assessed in the verification process of the model.

3.3.2 Tip resistance

The resistance at the tip is created by the displacement of the lattice and friction. As explained in chapter 0, the nodes at the tip of the monopile are only allowed to move in t-direction during the run of the solver, afterwards they are displaced by the pile in n-direction. This method of calculating the displacement could also have an effect on the forces generated at the tip.

3.3.2.1 Displacement force

As the pile moves through the lattice, nodes are displaced to make way for the pile volume. As these nodes are displaced, the spring and damper elements with which they are connected are pressed

Figure 34: Free body diagram of node at the tip

together. This causes a reaction force and as a result the nodes are pressed against the flipper. The force that the node exerts on the pile is called the normal force. It acts in a direction perpendicular to the flipper surface. As a result it has a component in X-direction and Z-direction. Consequently, only the component in Z-direction contributes to the total soil resistance.

3.3.2.2 Tip friction

The friction at the tip is very similar to the friction at the shaft. There are however two main differences. The first difference is the friction factor. The model uses two friction factors, one for the tip and one for the shaft. The second difference is the contribution to the total soil resistance in Z-direction. The friction force on the pile runs parallel to the flipper surface, just as the normal force, only the component in Z-direction contributes to the total soil resistance.
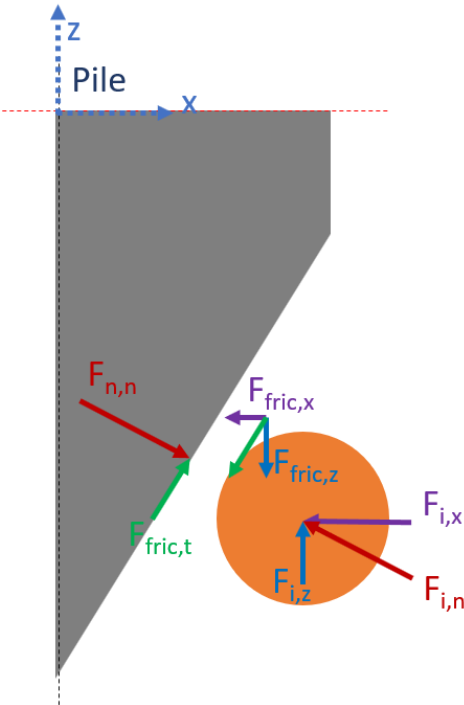
3.4 Forcing on the pile

The vibrations generated by the Vibro-drill not only reduce the friction, they also have an effect on the downward force of the monopile. This chapter goes further into how this effect is accounted for.

The forcing in this model is generated by the Vibro-drill. The eccentric force of the vibro-drill would be most effective if it would have the same frequency as the natural frequency of the pile. However, this is not possible because the pile is assumed to be rigid and consequently has no natural frequency. Therefore, as stated in chapter 3.1, the effects of the eccentric force of the Vibro-drill are simplified.

Aside from the forcing the effect of vibrations, jetting and liquefaction on the friction factor has to be assessed. Chapter 0 explains how the Vibro-drill is incorporated in the model.

The eccentric masses used to generate the vibrations can be installed in various configurations. Each configuration favours vibrations in a certain direction and opposes vibrations in other directions. A possible configuration uses vibrations that excite the pile in a torsional direction. For this model, the torsional direction of the pile is the 3^d dimension (Y-direction), and since the pile is not allowed to move in this direction, this configuration will not be dealt with in this research. Another configuration could be one in which the pile is excited in Z-direction, a direction in which the pile is allowed to move, consequently this is the configuration that will be assessed in this research.

As stated in the beginning of this chapter, the pile is modelled as a rigid body, consequently, the vibrations can't create resonance within the pile. In the lattice however, they can. The vibrations are modelled as a sinusoidal force on the pile with two different frequencies, one of which corresponding to the natural frequency of the lattice the other corresponding to the frequency used by the previous Vibro-drill penetration model of B. Arntz.

Figure 35: Forces that act on the pile

3.5 Model structure

Now that each individual part of the model is elaborated on, the operation of the combined model can be looked further into. On the next page a flowchart is used to walk through the model, starting with defining the parameters and finishing with the results being plotted.
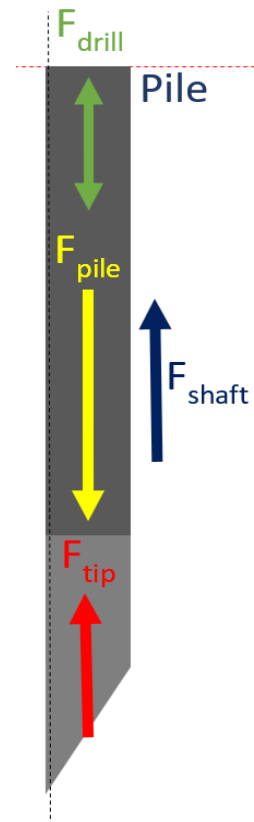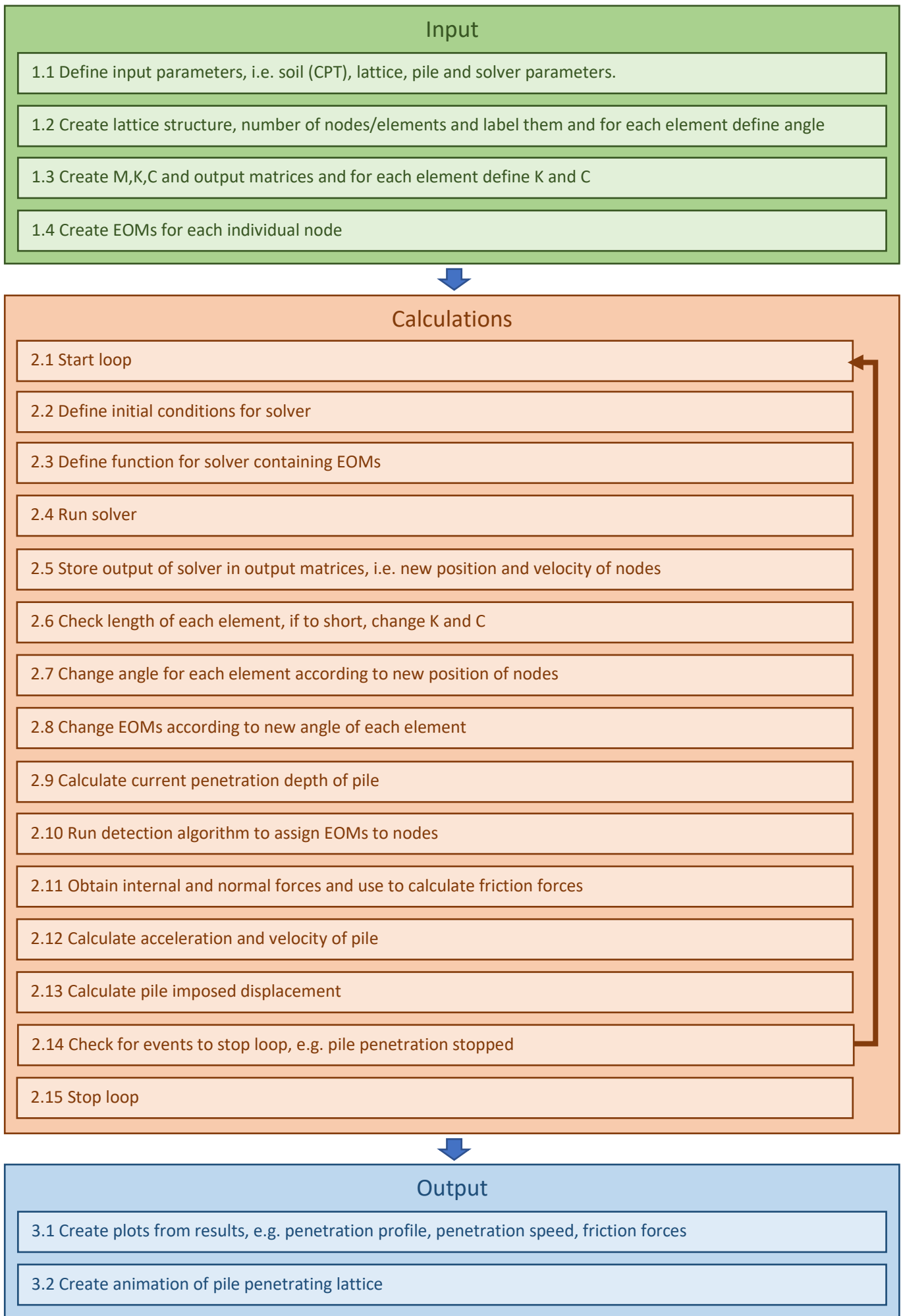
Input

1.1 Define input parameters, i.e. soil (CPT), lattice, pile and solver parameters.

1.2 Create lattice structure, number of nodes/elements and label them and for each element define angle

1.3 Create M,K,C and output matrices and for each element define K and C

1.4 Create EOMs for each individual node

Calculations

2.1 Start loop

2.2 Define initial conditions for solver

2.3 Define function for solver containing EOMs

2.4 Run solver

2.5 Store output of solver in output matrices, i.e. new position and velocity of nodes

2.6 Check length of each element, if to short, change K and C

2.7 Change angle for each element according to new position of nodes

2.8 Change EOMs according to new angle of each element

2.9 Calculate current penetration depth of pile

2.10 Run detection algorithm to assign EOMs to nodes

2.11 Obtain internal and normal forces and use to calculate friction forces

2.12 Calculate acceleration and velocity of pile

2.13 Calculate pile imposed displacement

2.14 Check for events to stop loop, e.g. pile penetration stopped

2.15 Stop loop

Output

3.1 Create plots from results, e.g. penetration profile, penetration speed, friction forces

3.2 Create animation of pile penetrating lattice

Figure 36: Schematic overview of model

4 Verification

The previous chapter explained how the model is constructed. It now reaches a point at which the model is ready to produce results. However, it is important to assess whether the results of the model make sense. Several parts of the model need to be verified in order to determine whether the results can be assumed to be valid. This is done by focusing the model on one task, independent of other aspects of the model, for which a prediction can be made of what a valid outcome would be, and then compare the outcome to the predicted results. If the results match the predicted outcome, that aspect of the model can be regarded as valid.

First a short introduction as to the physics behind the model. The pile dynamics describe how the pile moves over time. When the pile is released above the ground gravitational forces acting on the pile will make it accelerate. As the pile moves through the soil the soil resistance will act in the opposite direction of the penetration of the pile and thus will slow the pile down. Eventually the resistance will become equal to the gravitational force of the mass of the pile and it will come to a hold. Consequently, the penetration speed of a pile depends hugely on the pile dynamics and the soil resistance. It is therefore very important to verify those aspects of the model. Firstly, the pile dynamics will be looked at, and thereafter the soil resistance.

4.1 Pile dynamics

Every object that is released at a certain height in an environment without friction will have an acceleration equivalent to the gravitational acceleration. Consequently, this should also hold for the pile in this model. To recreate a pile freely falling through the lattice, all the lattice parameters, i.e. mass and spring and damper coefficients are set to zero. This replicates the absence of soil. Now, if the pile is released, the acceleration of the pile should be equal to the gravitational acceleration.

let's explain as to why this is the case. When the pile is released at a certain height, the first thing it will do is accelerating due to the gravitational force. Since there is no lattice there is no friction or another force to slow the pile down, therefore the acceleration will stay constant at the value of the gravitational acceleration 9,81 m/s^2. Consequently the velocity will increase with the same gravitational acceleration of 9,81 m/s^2. Finally the penetration depth will increase exponentially, as a consequence of the constant acceleration.
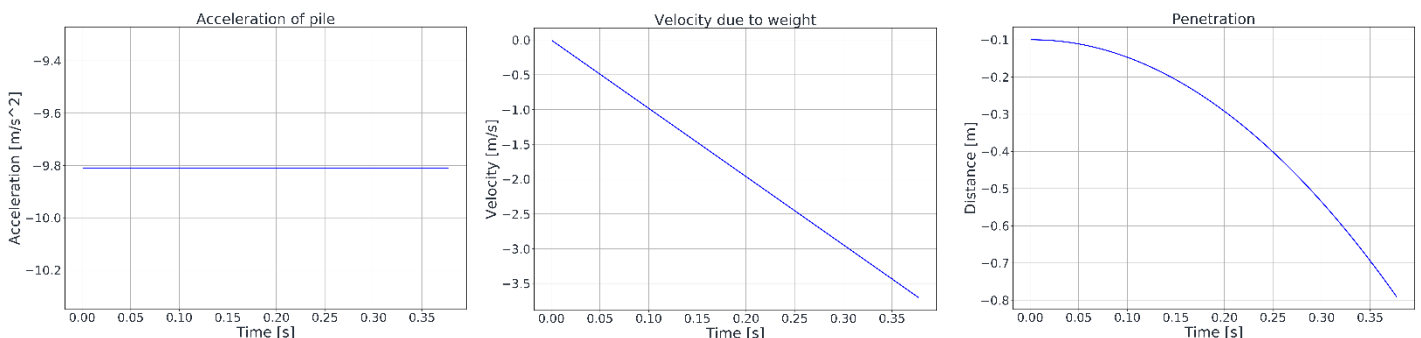

Figure 37: Acceleration, velocity and penetration diagrams for a free falling pile

The graphs above show the acceleration, velocity and penetration depth of the pile over time. The graph of the acceleration shows the acceleration on the y-axis and the time on the x-axis. It can clearly be seen that the acceleration of the pile remains constant at - 9,81 m/s^2, the value is minus because the pile moves down while the positive Z-direction is up. The graph for the velocity shows the velocity on the y-axis and the time on the x-axis. The velocity increases linearly with an acceleration of - 9,81 m/s^2. Finally, the penetration increases exponentially. This is exactly what could be expected and therefore it can be concluded that the pile dynamics are verified.

4.2 Soil resistance

As explained in 3.3 the soil resistance is the interaction between the pile and the soil which will resist the penetration of the pile.

To get a good insight into the forces that are created by the pile/lattice interaction, all possible variations in soil forces due to different soil layers and installation speed are eliminated. As a result, an even lattice, in which mass, spring and damper constants are the same over the depth of the model, is assumed during the pile penetration. The pile penetration speed itself, is assumed to remain constant.
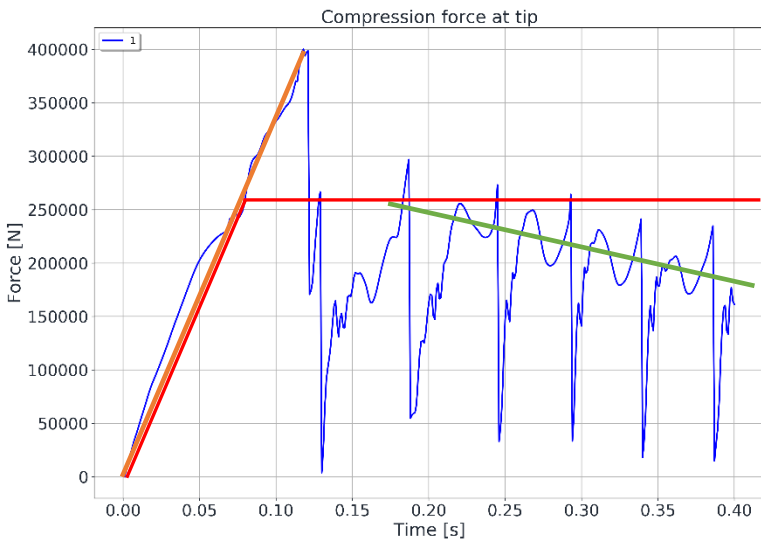
Figure 39: Tip resistance
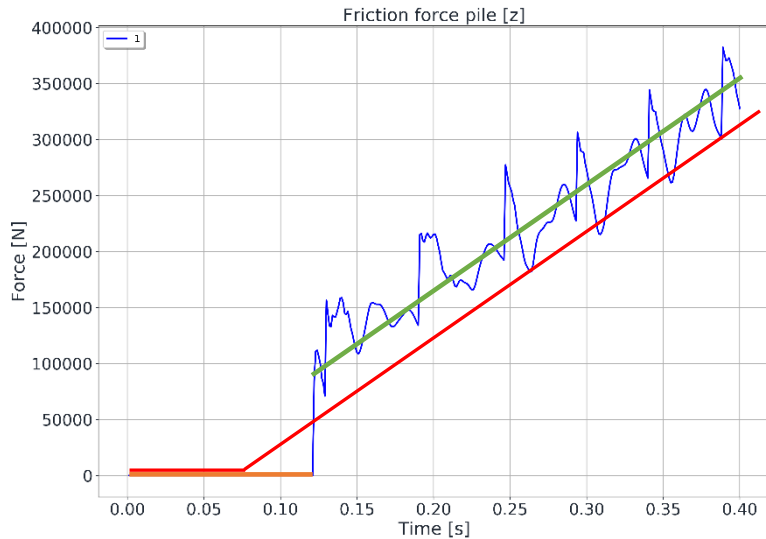
Figure 38: Shaft resistance

——	Actual soil resistance
——	Expected soil resistance
——	Actual soil resistance when there are only nodes at the tip
——	Trend line of soil resistance for the rest of the simulation
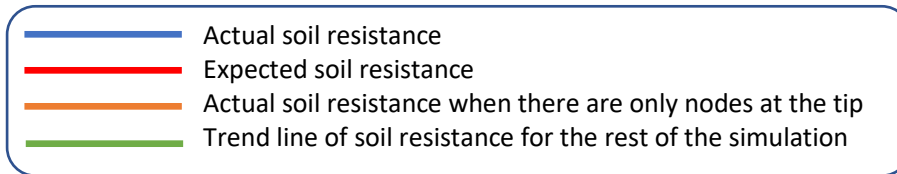
In the verification process of the soil resistance the two relevant locations are the tip and at the shaft. Figure 39 shows the soil resistance at the tip and Figure 38 shows the soil resistance at the shaft. In both figures the blue line represents the soil resistance as resulting from the model, the orange line shows the resistance when there are only nodes touching the tip, the green line shows a trend line of the soil resistance during the rest of the simulation. The red line shows the soil resistance one would expect as the outcome of the model.

Let us first look into the expected result depicted by the red line. As soon as the pile touches the soil the soil resistance at the tip is expected to increase, and since the penetration speed is assumed to be constant, this resistance will increase linearly. It increases until the full length of the tip has penetrated through the soil. At this point, some soil will move from the tip to the shaft and will therefore no longer contribute to the tip resistance, but instead to the shaft resistance. Therefore, from this point onwards the tip resistance will remain constant.

For the shaft resistance the expected outcome is quite straightforward. At first there is only soil at the tip, so there is no shaft resistance. Once the soil moves from the tip to the shaft, the shaft resistance will increase linearly.

As regards the actual soil resistance, it is assumed that the fluctuations in the blue lines are caused by the lattice. The lattice only describes the soil in certain locations/nodes, these nodes have certain EOM's that

restrict the movement in certain directions. This will have an effect on the soil resistance of the model. Subsequently, when a node will move from the tip to the shaft these restrictions change causing the node to shift rapidly which results in fluctuations. Orange and green lines are introduced that follow the trend of the graph and eliminate the fluctuations.

Figure 39 shows that the tip resistance increases linearly, as would be expected. However, between 0.07 and 0.17 seconds something strange happens. First the resistance increases further than expected, than it drops to nearly zero and eventually it returns to the expected value. This is the result of a build-up of nodes at the tip. Apparently, at the beginning of the simulation it is hard for the nodes to reach the shaft. This is probably caused by the size of the lattice and the restriction in movement of the nodes at the tip. As soon as one node passes to the shaft, more nodes quickly follow, causing a chain reaction which results in a large fluctuation in the tip resistance. The orange line clearly shows this phenomenon. More nodes at the tip translates to a higher tip resistance. At one point the excess nodes move from the tip to the shaft very rapidly, causing a drop in the tip resistance and spike in the shaft resistance after which the tip resistance goes back to its actual value. This phenomenon can also clearly be seen in the graph for the shaft resistance. The resistance at the shaft remains zero for a longer duration than expected, afterwards there is a large spike in the resistance and eventually the resistance increases linearly.

From 0.17 to 0.4 seconds the model is penetrating the soil while all the nodes transfer freely from tip to shaft. The green line shows the trend of the resistance after the tip is totally penetrated. When looking at the tip resistance it can be observed that, as the pile penetrates the lattice, the tip resistance reduces, while it is expected to remain the same. This is caused by the size and even properties of the lattice. Since the lattice is assumed to be even, the spring stiffness does not increase over the depth. As the pile penetrates the lattice, less and less nodes are present underneath the pile, resulting in less spring damper elements that are able to generate a reaction force, thus lowering the tip resistance. Using a larger lattice will overcome this problem. With a large lattice more nodes are present underneath the pile, as a result there will always be nodes to capture the force of the pile, thus the resistance will remain the same. A similar phenomenon is observed at the shaft friction. In this simulation the lattice is narrow, therefore the internal force of the lattice is influenced by the edge of the lattice. There are too few nodes between the wall and the pile to capture the energy of the pile, resulting in a higher internal force and, consequently, friction force.

If the simulation is done with a larger lattice these phenomena will be less apparent. Therefore the conclusion is that the lattice model accurately represents the tip and shaft friction.

4.2.1 Total soil resistance

Now that the tip and shaft friction are verified, the verification process of the total soil resistance is relatively easy. The total resistance is the summation of the tip and shaft friction. In Figure 40 the tip and shaft friction are plotted together with the total soil resistance. During the initial part of the graph the total soil resistance corresponds to the tip friction. Which makes sense since there is no shaft friction. As soon as the shaft friction is present, the total soil resistance starts to increase linearly, as would be expected. Therefore it can be concluded that the total soil friction is valid.
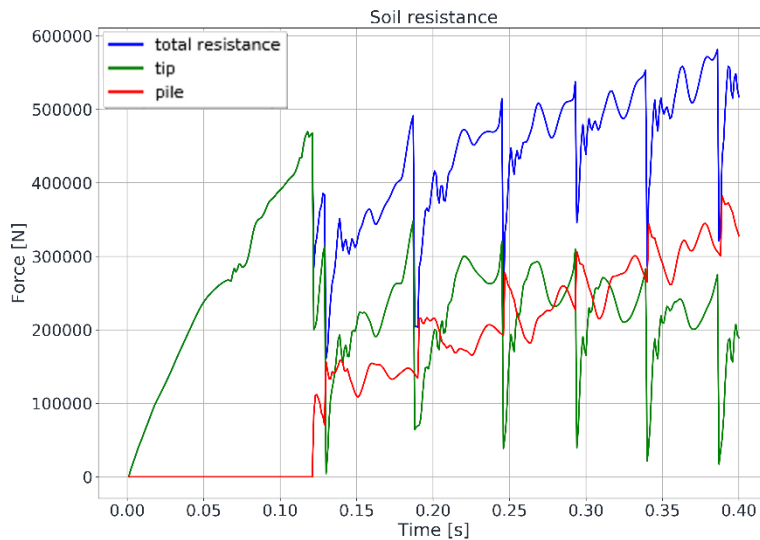
Figure 40: Total soil resistance

4.3 Damping coefficient

As explained in chapter 3.2.1, the damping ratio determines the ratio between the actual damping and the critical damping of this system. If the damping ratio is lower than 1 the system is underdamped. Which means that the system will overshoot its equilibrium position and then return and possibly overshoot it again. During each overshoot energy is dissipated, after a certain time the system stays at its equilibrium position. If the damping ratio is equal to one the damping of the system is equal to the critical damping, hence the system is critically damped. This is the exact damping at which no overshoot takes place and the equilibrium position is reached within the least time. If the damping coefficient is higher than one the system is overdamped. Like the critically damped system, no overshoot takes place but it takes longer for the system to reach its equilibrium. In Figure 41 this phenomenon is visualized in a graph for an arbitrary system. The x-axis shows the time and the y-axis shows the displacement. It is clearly visible that the green line, corresponding to a damping coefficient of 0.5, experiences two overshoots before it reaches its equilibrium, hence this is the underdamped case. The red line, the critically damped case, has no overshoot and reaches the equilibrium state quicker than the light blue line, the overdamped case. The blue line is a case with no damping at all, as a result the oscillations will always continue. This case will not be investigated for our system as this does not represent reality.
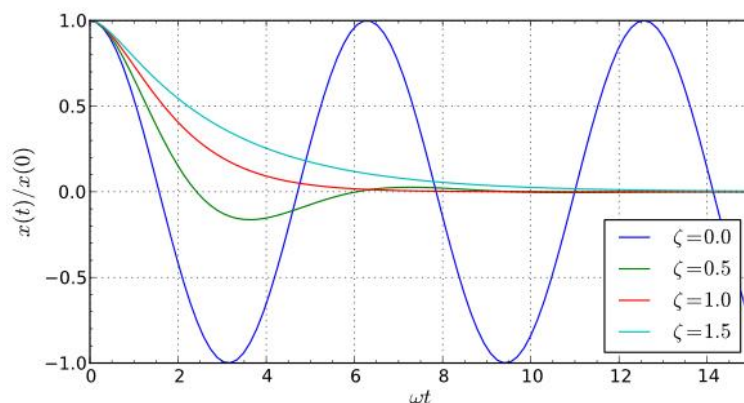
Figure 41: Damping coefficient explained

The damping coefficient is one of the parameters which can be used to calibrate the model. Therefore, the effect of the damping coefficient on the pile penetration needs further investigation. This is done by using a lattice with equal springs, dampers and masses and letting a pile penetrate the lattice. Only the damping

48

coefficient is changed between runs. Thus only the value of the dampers within the lattice change. The rest of system parameters stay the same.

In Figure 42 the penetration over time for 6 different damping coefficients is shown. As regards the two lowest damping coefficients 0.01 and 0.1 it should be noted that the penetration comes to an abrupt hold. It is not completely clear as to why this is the case, but it has probably something to do with the movement of the nodes. The transfer of nodes from the tip to the shaft does not happen fluently, it happens in stages. Nodes build up at the pile tip and at certain moments they transfer from tip to shaft. This is accompanied with a large increase in internal forces and, consequently friction forces. These forces slow the pile down, or, for cases with lower damping, make it stop penetrating completely. This phenomenon can also be seen for the damping coefficients of 0.5 and 1. The penetration of the pile is not smooth, even though the lattice parameters are the same over the depth. When the damping coefficient is increased to 5 or 10 the movement of the nodes is dampened such that the penetration profile becomes smooth, and the earlier discussed phenomena are not present anymore.

It can also be seen that, for a damping coefficient of 1 and 0.5, the penetration profile is more or less the same. When the damping coefficient is increased to 5 or 10 the penetration is less deep and it takes longer to reach the final penetration depth. Just as would be expected for an overdamped system.
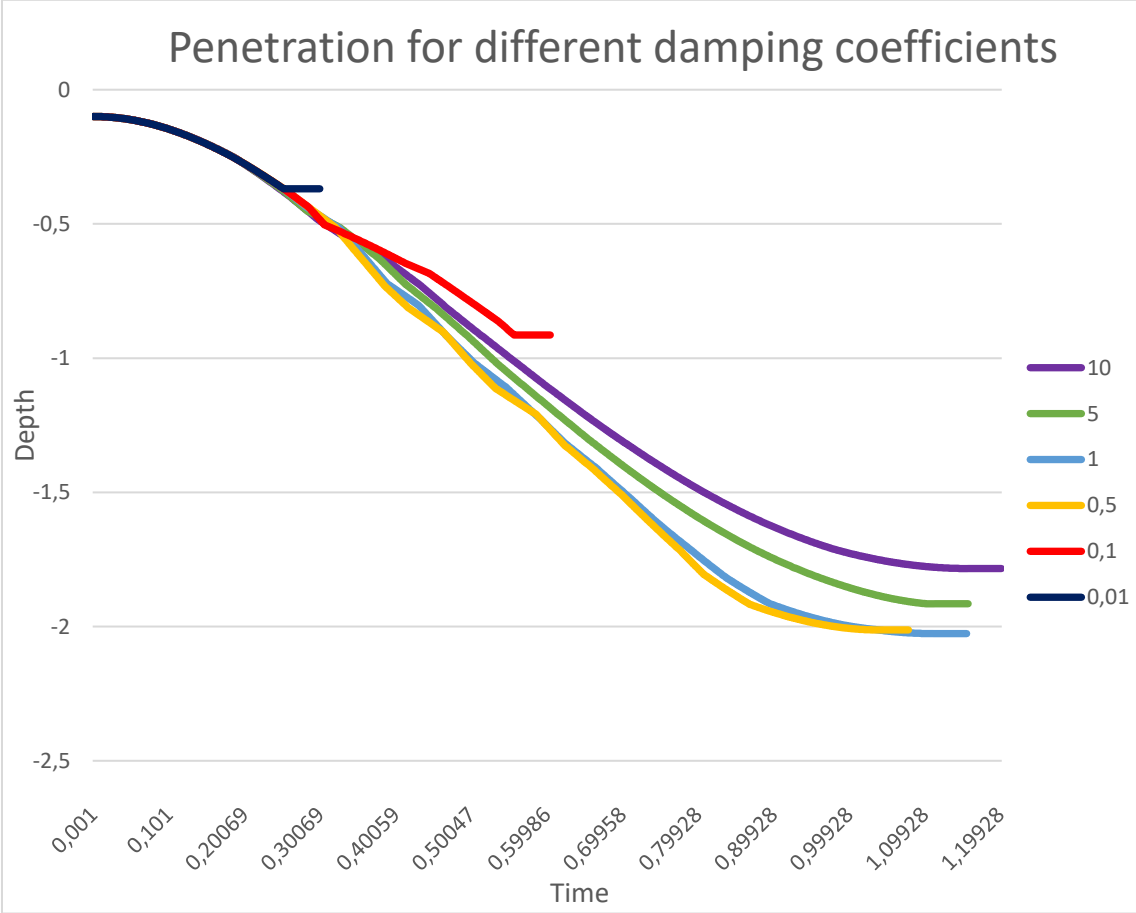
Figure 42: Penetration for different damping coefficients

4.4   Friction factor

The verification process for the friction factor is straightforward. As stated in chapter 3.3.1.2, the friction force is determined by multiplying the normal force with the friction factor. Consequently, if the friction force increases with a certain factor, the friction force should also increase by the same factor. In Figure 44 and Figure 44 the tip and shaft friction forces are shown for different tip and shaft friction factors.
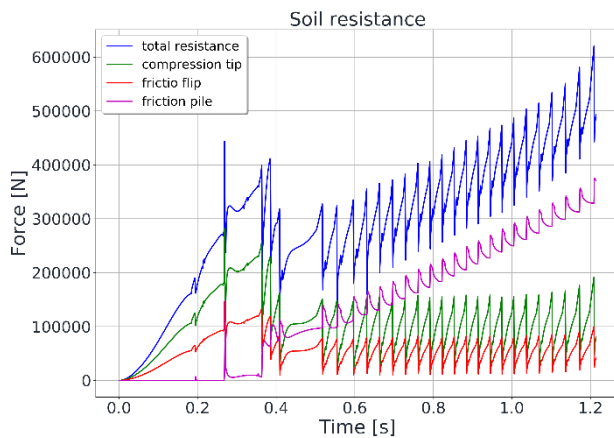
| Friction pile: | μ_{pile} = 0.3 |
| Friction tip: | μ_{tip} = 0.3 |

Figure 44: Soil resistance
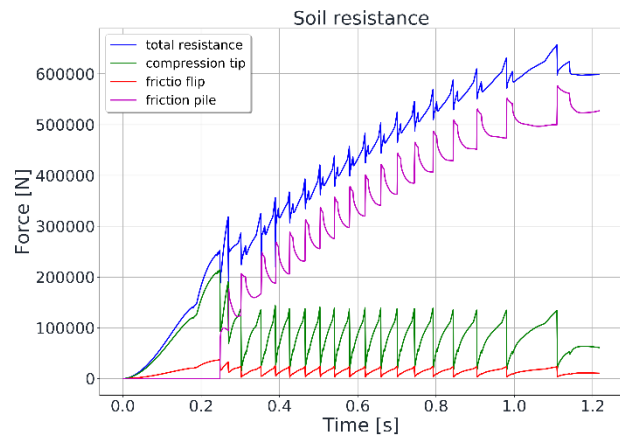
| Friction pile: | μ_{pile} = 0.4 |
| Friction tip: | μ_{tip} = 0.1 |

Figure 44: Soil resistance

Figure 44 shows that, if the tip friction *factor* is decreased with a factor three, the tip friction *force* also decreased by a factor three. In Figure 44 the same is observed for the shaft friction only now the factor is increased with a factor 0.3. Consequently the friction factors are assumed to be valid.

The penetration of the pile, soil response, friction factor and damping coefficient are now verified. This verification process leads to the conclusion that the results of the model can be assumed to be valid. The next step needed to obtain a realistic penetration prediction is to calibrate the model. This is an empirical process in which certain factors, like the damping coefficient and the friction factors, are changed until the results of the model represent real life test data. In this research however, the calibration process will not be done because of limited time. Instead, a lattice sensitivity analysis is performed, more information on this topic can be found in the next chapter.

4.5   Lattice sensitivity Analysis

There are certain input parameters that define the properties of the lattice. To find out how they affect the results of the model a sensitivity analysis is performed. For this purpose two aspects of the lattice will be assessed, the resolution and the size of the lattice. For each aspect different simulations will be performed, the results of these simulations will be compared. From this comparison the effect of each aspect on the result can be deduced.

4.5.1   Lattice size

As stated in chapter 3.2 the size of the lattice represents the amount of soil that is simulated. This is done by dividing the amount of soil into smaller volumes. These volumes are represented in the model by point masses and are connected via a spring/dashpot element. If a larger amount of soil is modelled, more energy can be absorbed by the lattice. This will have an effect on the penetration of the pile. This chapter will go further into how the size of the lattice affects the penetration of the pile.

The sensitivity analysis is performed by generating four penetration predictions in which all the parameters are the same except for the lattice size. The penetration predictions are then compared to see how the lattice size affects the penetration.
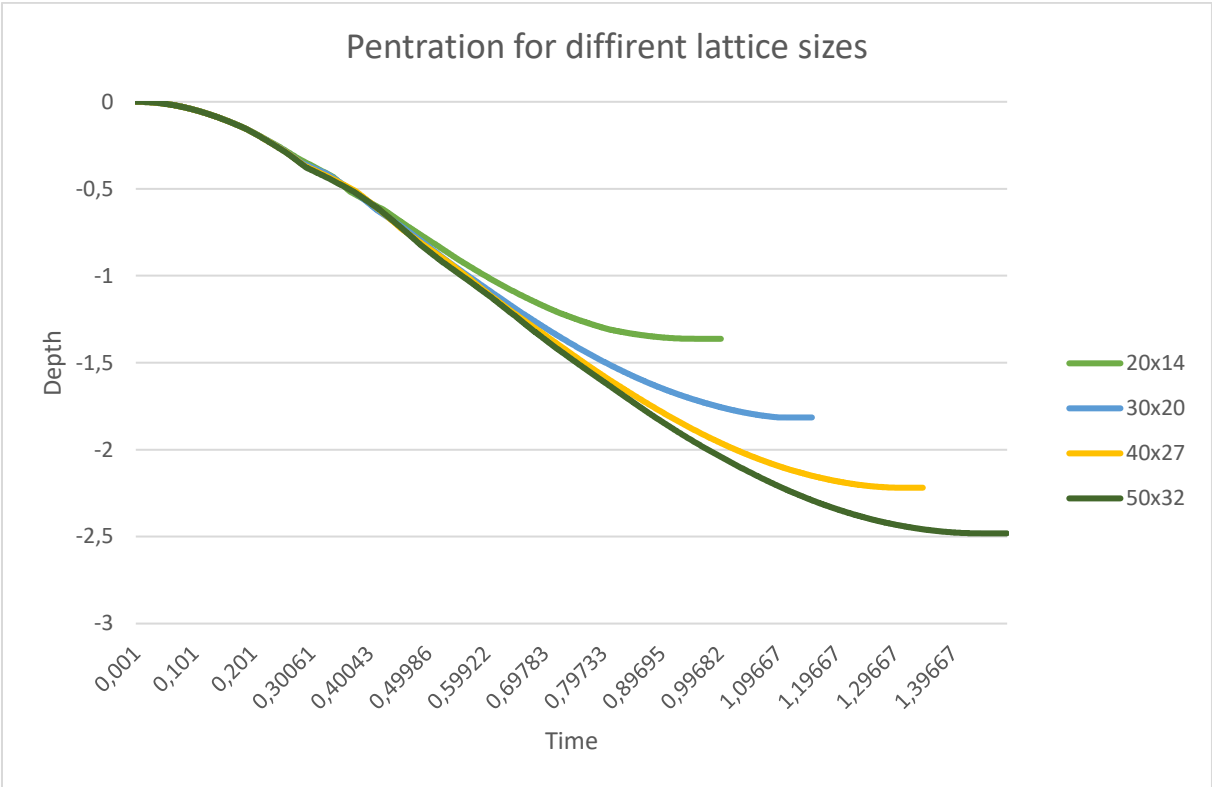

Figure 45: Penetration profile for different lattice sizes

Figure 45 clearly shows that as the lattice size increases the pile penetrates deeper. This has to do with the fact that the energy from the pile penetration is able to spread along more elements. The total spring stiffness of the system becomes lower as more springs are introduced. This principle is explained in Figure 46, which makes clear that adding more springs in series with the same spring stiffness actually reduces the spring stiffness of the total system. A similar phenomenon is happening when the lattice size is increased. As the lattice is increased more springs are added, thus the total stiffness of the system decreases and as a result the pile penetrates deeper. From the equation for the total spring stiffness it can also be concluded that, the more springs are added, the less difference it makes. Eventually, with each step, the difference in penetration depth becomes smaller, while the stepwise increase in lattice size remains the same. From this can further be concluded that eventually the penetration depth will go towards a maximum value. This can also be observed in Figure 45. In the recommendations a solution to this problem is proposed.

$$K_{system} = K_1 \qquad (4.1)$$
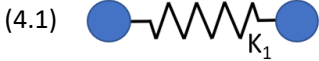
$$K_{system} = \left(\frac{1}{K_1} + \frac{1}{K_2} \right)^{-1} \qquad (4.2)$$

$$K_{system} = \left(\frac{1}{K_1} + \frac{1}{K_2} + \frac{1}{K_3} \right)^{-1} \qquad (4.3)$$

Figure 46: Combined spring stiffness explained

4.5.2 Resolution

As explained in chapter 0, the resolution of the lattice is defined by the unit distance, i.e. the distance between two nodes. The smaller the distance the more points within the lattice at which soil displacements are observed. The larger the distance the fewer points. This chapter looks into the effect of the resolution on the penetration of the pile. A high resolution will provide more information on the displaced soil, but will also increase the computation time. A low resolution could provide too little information such that the results become inaccurate/unrealistic.

In Figure 47 the penetration over time is shown for 5 different lattice resolutions. All penetrations take place in a lattice with even springs, dampers and masses. However, for each resolution the mass of each node changes as the distance between two nodes changes and, consequently, also the volume it represents. For a penetration in an even lattice a fluent penetration profile is expected. However, for almost all the resolutions this is not the case. At a depth of 0.4 meters almost all the penetrations seem to slow down after which they accelerate again. This is caused by the same phenomenon described in chapter 4.3, a build-up of nodes at the tip that at a certain point start to transfer to the shaft of the pile. During this process the friction forces on the pile increase and thus it is slowed down. It is remarkable to see that the penetration profile for the unit distance of 0,05 and 1,25 are almost the same. This shows that this phenomenon is present in both high and low resolutions. Concerning the final penetration depth, it can be assumed to vary for each resolution. An increase in unit distance does not necessarily mean an increase in final penetration depth. The most fluent penetration profile is found for a unit distance of 0,1. This is the same unit distance as is used for all the computation of the other results.

Figure 47: Penetration for different resolutions

5 Results

The model generates a lot of output. Some of this information is used to verify the validity of the model as is shown in chapter 4.1. Other information is used to execute a sensitivity analysis shown in chapter 4.2. For an applicable penetration model, however, one needs accurate results that reflect reality regarding the penetration depth and speed. This research focussed on certain aspects of the pile penetration which could be used as building blocks for a further development of a fully-fledged penetration model. As such the results are not yet sufficient to be compared to real life test. This study concentrates on the following three aspects:

1. Soil reaction should be captured in two dimensions.
2. Obtain a penetration speed that depends on the soil input and the weight of the pile.
3. Reach a final penetration depth.

The first goal is achieved by modelling the soil as a lattice. The nodes within the lattice represent the soil. They are allowed to move in Z- and X-direction, thus soil the soil dynamics are captured in a two-dimensional way.
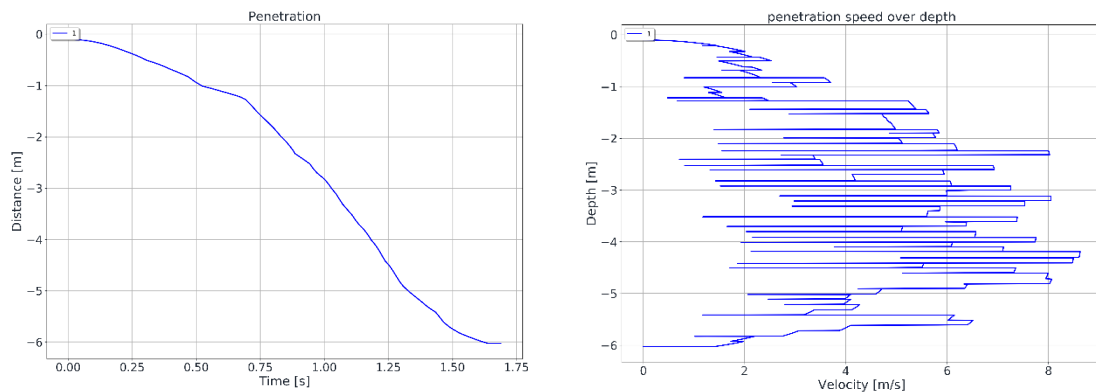
Figure 48: Penetration diagram and penetration speed over depth

Lattice size	Depth: 10m Width: 4m
Friction factor tip	0.3
Friction factor pile	0.2
Damping coefficient	0.1
Pile weight	100000 kg
Time step	0.001 sec
Eccentric moment	0.015 kg*m
Frequency	1200 Hz

Figure 49: Table with model input

The soil input for this model is provided in the form of a CPT. In Figure 48 the penetration diagram and penetration speed are shown in Figure 50 the CPT test data. The parameters used in this run can be found in Figure 49. The tip resistance and shaft friction determine the spring and damper coefficients of the lattice. Stiffer ground results in stiffer springs and dampers and vice versa. As a result, the penetration speed is lower during the penetration of tough soils and faster during the penetration of softer soils. Therefore the second goal regarding the penetration is also achieved.

As the pile moves through the lattice the total soil resistance increases to the point at which it is equal to the downward force of the pile. At this point the pile comes to a hold and the final penetration depth is reached, in this simulation the pile stopped at a depth of 6 meters. Consequently the goal regarding the final penetration depth of the pile can be assumed to be achieved.
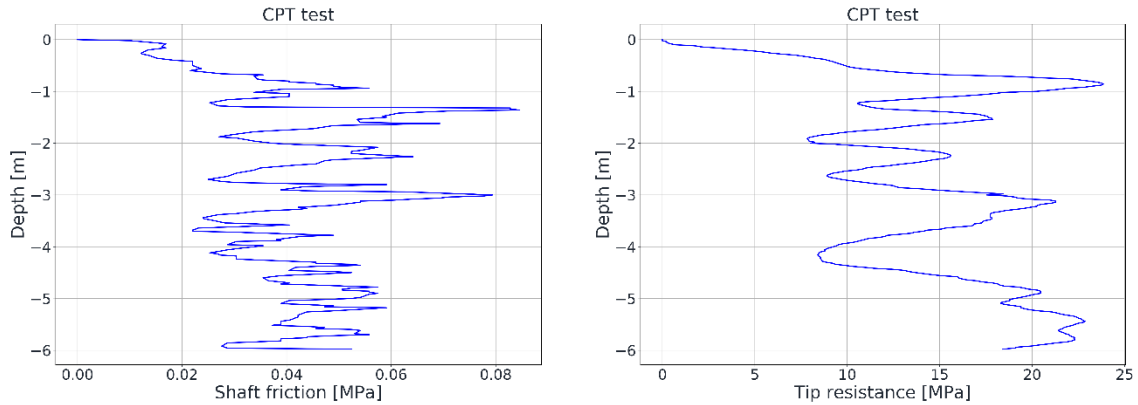
Figure 50:CPT test data: Shaft friction and Tip resistance

5.1 Discussion

Not everything regarding the penetration is in line with what would be expected. The time it takes to reach the final depth, for instance, is very short. It takes under two seconds in the simulation in Figure 48. There could be multiple reasons for this phenomenon. The first being that the pile used in this simulation is 15 times heavier than the pile used by GBM in the past tests. The heavier weight is chosen to ensure a pile penetration over a large depth. In doing so the difference in penetration speed over the depth is better visible.

The fast penetration also causes a sort of impact behaviour. As the pile reaches its final depth the simulation is stopped. If the simulation would keep on running the force of the lattice would actually start to push the pile back up again. This phenomenon could be compared to a wooden pile being dropped into water. First it would penetrate rapidly until it reaches a certain depth after which it would start to go back up again. Although this finding is very interesting and should be further investigated in the future, for now this is not necessary since it falls outside the scope of this study.

There are, however, a lot more assumptions that could cause this impact behaviour of the pile in the model. The model assumes double symmetry. This means that over two axis the model is assumed to be symmetrical, thus modelling a three-dimensional pile as a two-dimensional sheet. This is done to simplify the model and to reduce computation time. With hindsight this assumption is probably the main reason why the pile penetrates too fast. In a non-symmetrical lattice the nodes on the interface line of the model are connected to each other. If the pile would penetrate such a lattice it would take force to break the elements with which the interface nodes are connected. This will probably cause a build-up of nodes underneath the pile tip. As a result the force it would take to penetrate the lattice would be high and would therefore reduce the penetrations speed and thereby capturing reality in better way.
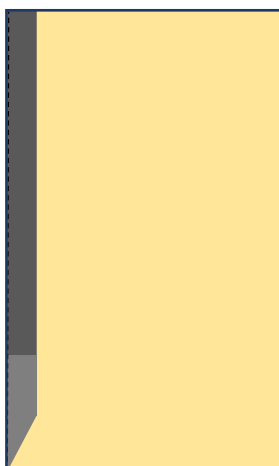

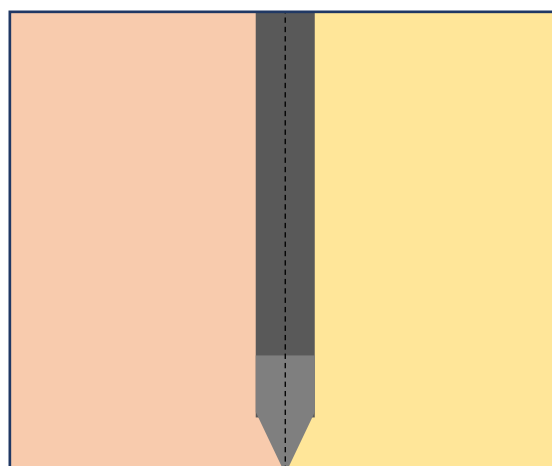*Figure 52: Symmetrical lattice, only one half is modelled.*

Figure 52: Non-symmetrical lattice, the lattice as a whole need to be modelled.

54

In this model the only way to account for the assumed symmetry is by restraining the interface nodes. They are assumed to be attached to the heartline or the pile at all times. Chapter 3.2.2 explains how this is achieved. Initially the assumption was made that this would solve the symmetry problem and that the model would generate realistic results. However, results from the model show that this is not the case. The interface nodes now behave as if they are not connected to the other side of the lattice. This phenomenon can clearly be observed in the data.
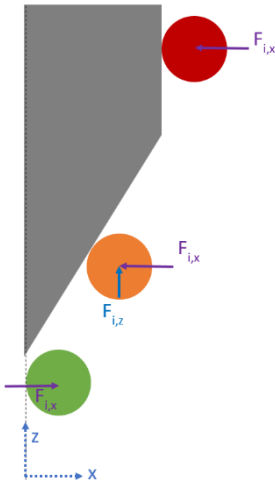
Figure 54: Interface, tip and pile nodes with their corresponding internal forces
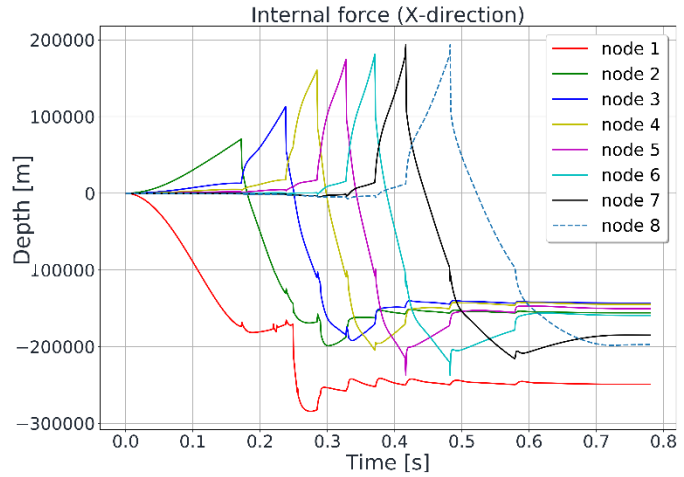
Figure 53: Internal forces for nodes 1 to 8 on the interface line

Figure 53 shows the internal forces for the nodes on the interface line over time. Form this it is clear that as the nodes move through the lattice the interface nodes (green nodes in Figure 54) are pulled inside the lattice by the other nodes (internal force in positive X-direction). As soon as they touch the pile tip they are allowed to move along the tip (orange nodes in Figure 54 and Figure 55) and the direction of the internal force changes from negative to positive, as shown in Figure 56. When the nodes reach the pile (red nodes in Figure 54) the internal forces are in negative X-direction, they are pushed against the pile. In reality one would expect that the nodes are pressed against the interface line as well as against the pile. The absence of gravity in the model is one of the reasons why the nodes do not experience this force and since there is no action taken to recreate this force, the results of the model are not realistic. Now the model simulates a pile that penetrates through a medium that experiences no gravity and along a wall with no friction. Regrettably there was not enough time to correct this error in the model.
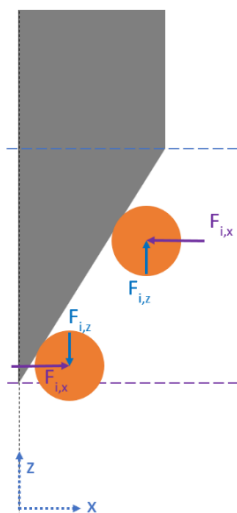

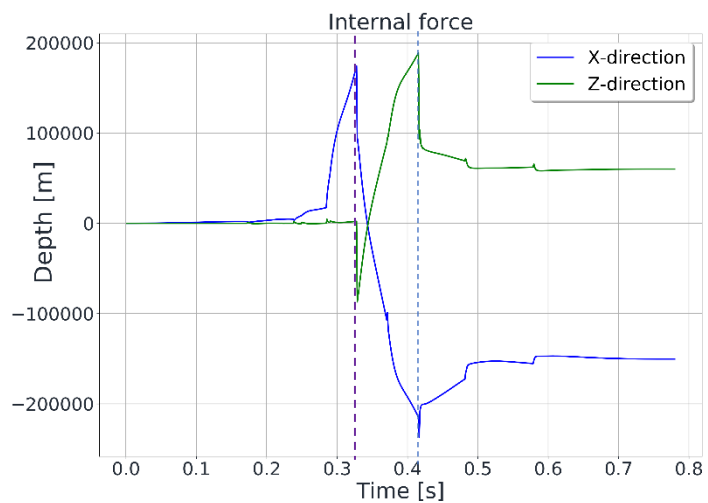Figure 55: Tip nodes with their corresponding internal forces

Figure 56: Internal force in X- and Z-direction for node 5

55

Also the soil reaction itself could cause this impact behaviour. Even though the reaction of the soil is captured in a two-dimensional way, which is a clear improvement over the current one-dimensional models, it still not captures the soil displacement in the third direction. As a result the soil displacement is restricted which could make it harder for the pile to displace the soil.

Since two masses within the lattice are only connected by a spring/dashpot element in line with the two masses, it only accounts for the compression force between two volumes of soil. The shear force is not accounted for in the model. Consequently a displacement between the two masses in the direction perpendicular to the spring damper element has almost no effect between the two masses. Including shear forces in the model would therefore better replicate the interaction between the soil volumes.

Since the model is not focussed on accurately predicting the friction force, it is accounted for in a very basic way. The friction force depends only on the normal force and the friction factor. The friction factor only changes between the tip and the shaft. In reality every soil type would have a different effect on the friction force. Assuming a single friction factor along the length of the shaft completely neglects the influence of these different soil types.

Finally a fixed boundary is assumed at the right and bottom side of the lattice. As is investigated in chapter 4.5.1, the size of the lattice, and thus the location of the fixed boundary, is of great influence on the penetration of the pile, as is concluded in Chapter 4.5.1. Increasing the size of the lattice would reduce the influence of the fixed boundary, but also increase the computation time.
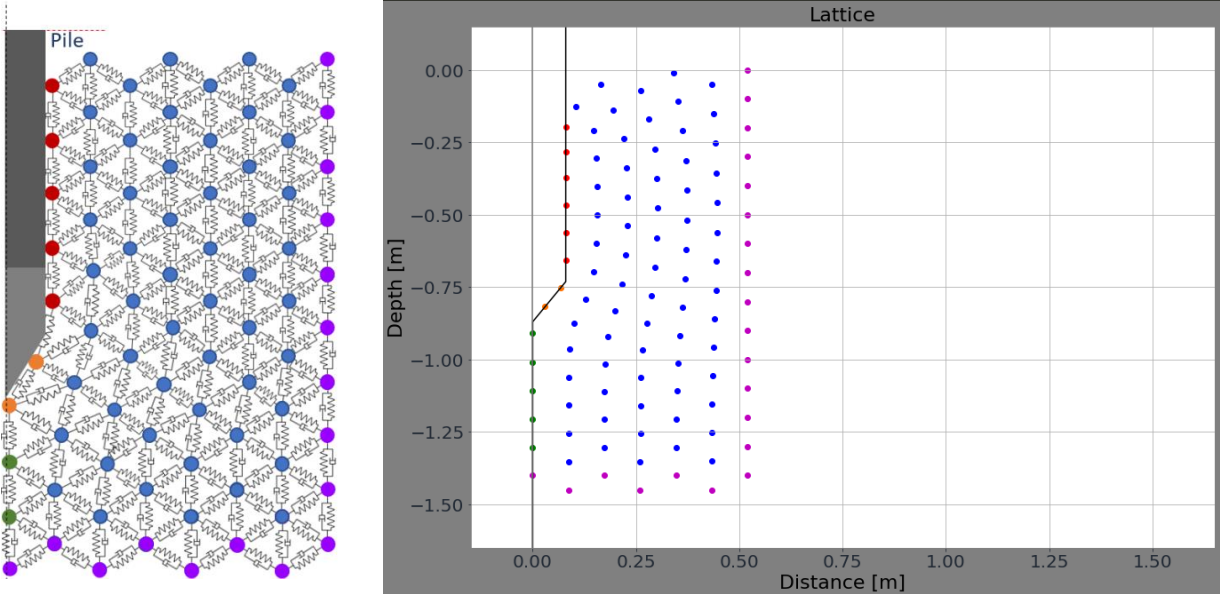

Figure 57: Picture of model

6 Conclusions and Recommendations

This thesis aims to develop a pile penetration predication model applicable for the Vibro-drill. It focusses on simulating the phenomena that occur when a pile penetrates soil. This is achieved by introducing a two-dimensional soil model in which a two-dimensional pile penetrates. While the pile penetrates the soil, forces are generated. These forces have an influence on the penetration speed and the final penetration depth of the pile, which are reflected in the results of the model. They are compared to the outcome of real-life tests with the Vibro-drill and the conclusion that can be drawn from this is that this model is a useful basis for the further development of a fully-fledged pile penetration model for the Vibro-drill.

Soil

The soil is modelled using a lattice model. A well-known practice when it comes to modelling soil in a two-dimensional way. A CPT correlation is used to translate CPT data into lattice parameters. As a result, the lattice is capable of describing different soil characteristics over the depth. This provides a realistic representation of the soil.

Pile penetration

The pile is modelled as a rigid body. Since there is no current method that describes the penetration of a pile in a lattice, for this thesis, a new method is developed. During the verification process it is shown that this method accurately simulates the penetration of the pile.

Friction forces

The friction forces are also subjected to a verification process. The model uses two different friction factors to calculate the friction, one for the tip and one for the shaft of the pile. Because of this, the friction force can be calculated separately for the tip and shaft. During the verification process the effect of the friction factors on the generated friction forces is analysed. Also the generated tip and pile friction are assessed to determine whether they match real life friction expectations. Finally the conclusion is made that the friction forces are correctly captured within the model.

Penetration speed

The friction forces and the weight of the pile are used to calculate the penetration speed of the pile. The friction forces depend on the lattice properties, which in their turn, depend on the CPT data. As a result the penetration speed will depend on different soil layers within the model, as the results show, it will slow down when penetrating a stiffer soil and accelerate when penetrating a softer soil. By doing so, the model properly reflects the real-life effects of the various types of soil on the penetration speed of the pile which enhances its usefulness as a penetration prediction model.

Vibro-drill

The Vibro-drill uses three phenomena to weaken the soil, i.e. vibrations, jetting and liquefaction. These effects are accounted for in multiple ways. The most important being the reduction in both the friction coefficients. The vibrations and jetting cause the friction at the tip to reduce. The friction of the shaft on the inside of the pile is reduced due to the liquefaction, the friction on the outside of the pile is reduced by the vibrations. Finally the eccentric forces generated by the eccentric masses are accounted for as a sinusoidal force which is added to the downwards force of the weight of the pile. As a result, adding these effects of the Vibro-drill has a positive effect on the penetration speed and final penetration depth.

6.1 Recommendations

As mentioned before, this thesis aims to provide a foundation for a fully-fledged penetration model. The first steps towards validation of the model are taken, but it cannot yet produce a reliable penetration prediction. For this to happen some steps need to be made. In this chapter these steps are elaborated on. The recommendations will be divided into two categories. The first being the recommendations towards producing a valuable penetration prediction. The second being the recommendations for the general improvement of the model.

To start with the first category. It is not yet known if applying these recommendations to the model will guarantee a valuable outcome, but it will most certainly be a step in the right direction. One of the problems explained in Chapter 5 has to do with the penetration speed. Now, the only way to penetrate the lattice is to make the pile heavier than normal. If a normal pile weight is used to run the model, the pile will penetration is very limited. This has probably something to do with the elements of the lattice. They now consist of a spring and a damper. As a result, only the elastic deformation of the soil is taken into account. When the oscillating force of the Vibro-drill is introduced, the effect it has on the penetration is not what would be expected. It is almost neglectable compared to the effect of the reduction in friction coefficients.

Non symmetrical lattice
The first attribute of the lattice that needs to be fixed is the problem described in Chapter 5.1. This chapter concludes that the way in which the symmetry is currently assumed in the model is not correct. As it stands, the model replicates a pile that penetrates along a friction-less wall and through a medium that does not experience gravity. Solving this issue would drastically increase the ability of the model to replicate a pile penetrating soil. This can either be achieved by introducing a force that replicates the forces that would be expected, but a better solution would be to get rid of the symmetry altogether and create a full lattice.

Slip/Stick method
If, instead of just a spring/dashpot element, also a slider/dashpot element is introduced in series with the spring/dashpot element, then also the plastic deformation of the soil can be accounted for. This is achieved by introducing a stick/slip method. If the system is in stick condition, only the spring/dashpot element is activated, resulting in only elastically deformed soil. If a certain critical force is subjected onto the element, the system transfers to the slip condition. While the system is in slip condition, both the spring/dashpot and the slider/dashpot element are activated. The soil is still deformed elastically by the spring/dashpot element, but also plastically by the slider/dashpot element. As a result the oscillating force of the Vibro-drill could be more visible. If this force causes the system to transfer into the slip condition it could make a huge difference in the penetration prediction compared to a pile without a the oscillating force of the Vibro-drill. Which is what is observed from prototype tests.

Shear force
Another improvement that could be beneficial for the model is to include shear soil forces between nodes. When soil is displaced, a large part of the energy is dissipated through shear forces between soil particles. By adding shear elements between nodes this shear forces could be replicated in the existing model. This adds another element of realness to the model which could possibly lead to a realistic penetration prediction.

Including either the stick/slip method or the shear force into the model and after a well performed calibration process the model is very likely to develop realistic penetration predictions. But besides those two additions, there are some other opportunities to further enhance the model.

Breaking elements
If a non-symmetrical lattice is introduced, the pile will actually penetrate the lattice, instead of slide along the side of the lattice as is the case now. For the pile to be able to penetrate the lattice, the elements through which it penetrates should be able to break. This can be implemented by introducing a maximum

element length. If this is reached, the element will break and no longer take part in the simulation. The node can now move along the pile and the pile itself can move further towards the next element.

Include vibrations in X-direction

Another benefit of introducing a non-symmetrical lattice is the ability to introduce a pile that can move in X-direction. Hence the pile can be vibrated in this direction to get a better insight in the effect these types of vibrations have on the penetration.

Non-reflective boundary

A non-reflective boundary is used to counteract waves that propagate along the lattice and reflect of the edge of the lattice back to the pile. In real life the soil continues infinitely, therefore, waves that propagate away from the pile will not have the opportunity to reflect back to the pile. Introducing non-reflective boundaries in the model will therefore better represent reality.

Friction factors for different types of soil

The friction factors used in the model are now applied as a shaft friction factor and a tip friction factor. As proven in chapter 0, if the friction factor changes, the corresponding friction forces change accordingly. However, along the tip and the shaft there are other aspects that have an influence on the friction force. These are not accounted for in the model as it stands. This could be improved by introducing a friction factor for each specific type of soil that could be found from a CPT. Than the CPT could be used to define not only the lattice parameters but also different friction factors along the depth of the lattice.8

I. Bibliography

Arshad, M., & O'Kelly, B. C. (2016). Analysis and Design of Monopile Foundations for Offshore Wind-Turbine Structures. *Marine Georesources and Geotechnology*, *34*(6), 503–525. https://doi.org/10.1080/1064119X.2015.1033070

Azzouzi, S. (2003). *Intrillen stalen damwanden*.

B.J.M. Arntz, D. (2018). *Developing the Vibro-drill ;* 1–69.

Chow Y, Smith I (1984) A numerical model for the analysis of pile driveability. In: 2nd International conference on the application of stress wave theory on piles, Balkema, Rotterdam

Cudmani R, Sturm H (2006) An investigation of the tip resistance in granular and soft soils during static, alternating and dynamic penetration. In: International conference on vibratory pile driving and deep soil compaction, Paris, France

Dierssen, G. (1994) Ein Bodenmechanisches Modell zur Beschreibung des Vibrationrammens in körnigen Böden, Dissertation, University Karlsruhe, Germany.

Groen, E. C. (2016). *Rotational jetting in clay*.

Holeyman A (1993) HIPERVIB1, An analytical model-based computer program to evaluate the penetration speed of vibratory driven sheet piles. Research report prepared for BBRI, June 1993

J.S. Hoving, 2019 *"Hydrid linear-nonlinear systems to describe the non-smooth dynamic behaviour of media in the time domain"*,
PhD-thesis, Delft University of Technology, in progress (exp. June 2020).

Henke, S., & Grabe, J. (2006). Simulation of pile driving by 3-dimensional Finite-Element analysis. *Proc. of the 17th EYGEC.--Zagreb*, (August 2016), 215–233.

Jonker, G. (1987). Vibratory pile driving hammers for pile installations and soil improvement projects. *Proceedings of the Annual Offshore Technology Conference*, *1987-April*, 549–560.

Kastelein, R. A. (2014). *Effect pile driving on porpoise hearing*. (September), 1–17.

Leonards, G.A., Deschamps, R.J., and Feng, Z., 1995. Driveability, load/settlement and bearing capacity of piles installed with vibratory hammers. Final Report submitted to the Deep Foundations Institute. School of Engineering, Purdue University, West Lafayette, Indiana, USA

Mabsout, M. E., Reese, L. C., & Tassoulas, J. L. (1995). Study of pile driving by finite-element method. *Journal of Geotechnical Engineering*, *121*(7), 535–543. https://doi.org/10.1061/(ASCE)0733-9410(1995)121:7(535)

Matlock, H. (1977). *OTe 2842 ANALYSIS OF DRIVING OF FOUNDATION PILES*.

Maradudin A. A., Montroll E. W.,. Weiss G. H, Ipatova I. P. (1971) Theory of lattice dynamics in the harmonic approximation

Mens, A. M. J., Korff, M., & van Tol, A. F. (2012). Validating and Improving Models for Vibratory Installation of Steel Sheet Piles with Field Observations. *Geotechnical and Geological Engineering*, *30*(5), 1085–1095. https://doi.org/10.1007/s10706-012-9506-5

Robertson, P. K. (2013). The James K. Mitchell lecture: Interpretation of in-situ tests-some insights. *Geotechnical and Geophysical Site Characterization 4 - Proceedings of the 4th International Conference on Site Characterization 4, ISC-4*, *1*, 3–24.

Robertson, Peter K. (2010). Soil behaviour type from the CPT: an update. *2nd International Symposium on Cone Penetration Testing*, (May), 8 p.

Robertson, Peter K. (2015). *Introduction to Cone Penetration Testing CPT Guide Outline & Scope History of CPT*. 1–33.

Schrocht, S. (2015). *Technical Noise Mitigation during Offshore-Windfarm Foundation Installation Examples from Offshore Windfarms*. (October), 1–18.

Dorival, Simone, A. (2008). *OMAE2008-57918*.

Suiker, Metrikine, De Borst, A. (2001). Comparison of wave propagation characteristics of the Cosserat continuum model and correspondingdiscrete lattice models

Smith, I. M., & To, P. (1988). Numerical studies of vibratory pile driving. *International Journal for Numerical and Analytical Methods in Geomechanics*, *12*(5), 513–531. https://doi.org/10.1002/nag.1610120506

Van Baars, S. (2004). Design of sheet pile installation by vibration. *Geotechnical and Geological Engineering*, *22*(3), 391–400. https://doi.org/10.1023/B:GEGE.0000025047.17363.f8

Van De Brug, E., Van Bergen, M., Van Griethuysen, D. E., De Boom, W., Prins, R., & Kuijpers, P. (2010). Optimal integrated combination of foundation concept and installation method. *European Wind Energy Conference and Exhibition 2010, EWEC 2010*, *5*, 3947–3948.

Wang, J., & Zhao, B. (2014). Discrete-continuum analysis of monotonic pile penetration in crushable sands. *Canadian Geotechnical Journal*, *51*(10), 1095–1110. https://doi.org/10.1139/cgj-2013-0263

Whenham, V., & Holeyman, A. (2005). *Vibrodriving prediction models vs. experimental results*. (1), 1–12.

Wind Europe. (2018). Offshore wind in Europe. *Refocus*, 1–37. https://doi.org/10.1016/S1471-0846(02)80021-X

II. List of Figures

III.   List of symbols

Symbol	Unit	Description
F_{drill}	[N]	force of drill
F_{fric}	[N]	friction force
F_n	[N]	normal force
F_{pile}	[N]	force due to weight pile
F_i	[N]	internal force
F_{soil}	[N]	soil resistance force
E_{kin}	[J]	kinetic energy
E_{pot}	[J]	potential energy
I_{SBT}, I_c	[-]	Robertson soil behaviour type
R_f	[%]	friction ration
c_c	[kNm/s]	critical damping
d_y	[m]	third dimension
e_j	[m]	elongation
p_a	[kN/m^2]	atmospheric pressure
q_c	[MPa]	conus resistance
Δt	[s]	simulation time step
u_j, u_x, u_z	[m]	Displacement
$\dot{u}_x, \dot{u}_z$	[m/s]	velocity
$\ddot{u}_x, \ddot{u}_z$	[m/s^2]	acceleration
w_n	[rad]	eigenfrequency
x_{node}	[m]	distance
$z_{node, tip}$	[m]	distance
α_E	[-]	Advanced Youngs modules factor
σ_{vo}	[kN/m^2]	total, effective stress
ν	[-]	poissons ratio
C, C_j	[kNm/s]	damping
E	[kN/m^2]	Youngs modules
F	[kN]	force
G	[kN/m^2]	Shear modules
K, K_j	[kN/m]	stiffness
$\hat{K}$	[kN/m]	combined spring stiffness
L	[J]	Lagrangian
M	[kg]	mass
V	[m^3]	volume
f^{ext}	[N]	external force
f^{int}	[N]	internal force
g	[m/s^2]	gravitational acceleration

t	[s]	time	
x, z, y, n, t	[-]	directions	
α	[deg]	angle element	
α	[-]	Youngs modules factor	
β	[deg]	angle tip	
λ	[kN/m^2]	Lamé parameter	
μ	[kN/m^2]	Lamé parameter, Shear modules	
ρ	[kg/m^3]	density soil	
φ, ζ	[-]	damping ratio	

Abbreviations

CPT	Cone Penetration Test
EOM	Equation Of Motion
GBM	Ground Breaking Machines
Hz	Hertz
m	Meter
mm	Millimetre

Appendices

A. Equation of motion full derivation

The derivation of the EOM in X- and Z-direction for multiple configurations using the Lagrange method.

Lagrangian:
$$L = E_{kin} - E_{pot}$$

Euler-Lagrange:
$$\frac{\partial L}{\partial u_{x/z}} - \frac{\partial}{\partial t}\frac{\partial L}{\partial \dot{u}_{x/z}} = 0$$

Kinetic energy:
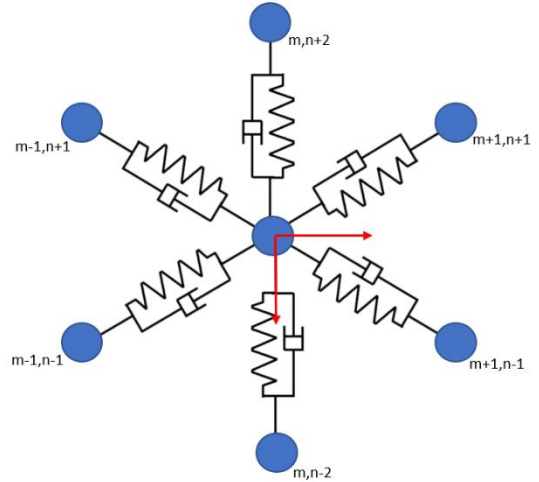$$E_{kin} = \tfrac{1}{2}m(\dot{u}_x)^2 + \tfrac{1}{2}m(\dot{u}_z)^2$$

Potential energy:
$$E_{pot} = \sum_j \tfrac{1}{2}k_j(e_j)^2$$

Linearizatie, only valid for small displacement:
$$E_{pot} = \sum_j \tfrac{1}{2}k_j((u_x^{nj} - u_x^n)\cos(x) + (u_z^{nj} - u_z^n)\sin(x))^2$$

$$E_{pot} = \sum_j \tfrac{1}{2}k_j((u_x^{nj} - u_x^n)^2 \cos^2(x) + 2(u_x^{nj} - u_x^n)(u_z^{nj} - u_z^n)\cos(x)\sin(x) + (u_z^{nj} - u_z^n)^2 \sin^2(x))$$

Lagrangian:
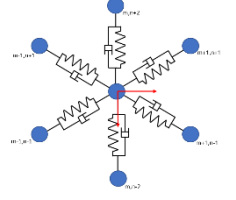$$L = E_{kin} - E_{pot}$$

$$L = \tfrac{1}{2}m(\dot{u}_x)^2 + \tfrac{1}{2}m(\dot{u}_z)^2 - \sum_j \tfrac{1}{2}k_j((u_x^{nj} - u_x^n)^2 \cos^2(x) + 2(u_x^{nj} - u_x^n)(u_z^{nj} - u_z^n)\cos(x)\sin(x) + (u_z^{nj} - u_z^n)^2 \sin^2(x))$$

Euler-Lagrange:
$$\frac{\partial L}{\partial u_{x/z}} - \frac{\partial}{\partial t}\frac{\partial L}{\partial \dot{u}_{x/z}} = 0$$

6.2 Derivation for inner nodes with start angles.

For x-direction:

$$\frac{\partial(-\sum_j \frac{1}{2}k_j((u_x^{nj}-u_x^n)^2\cos^2(x)+2(u_x^{nj}-u_x^n)(u_z^{nj}-u_z^n)\cos(x)\sin(x)+(u_z^{nj}-u_z^n)^2\sin^2(x)))}{\partial u_x} - \frac{\partial}{\partial t}\frac{\partial(\frac{1}{2}m(\dot{u}_x)^2+\frac{1}{2}m(\dot{u}_z)^2)}{\partial \dot{u}_x}=0$$

$$\frac{\partial L}{\partial u_x}-\frac{\partial}{\partial t}\frac{\partial L}{\partial \dot{u}_x}=-m\ddot{u}_x-\sum_j\frac{1}{2}\frac{k_j}{\partial u_x}((u_x^{nj}-u_x^n)^2\cos^2(x)+2(u_x^{nj}-u_x^n)(u_z^{nj}-u_z^n)\cos(x)\sin(x))=0$$

$$m\ddot{u}_x+\sum_j\frac{1}{2}\frac{k_j}{\partial u_x}\left((u_x^{nj}-u_x^n)^2\cos^2(x)+2(u_x^{nj}-u_x^n)(u_z^{nj}-u_z^n)\cos(x)\sin(x)\right)=0$$

$$m\ddot{u}_x+\sum_j\frac{1}{2}\frac{k_j}{\partial u_x}\begin{pmatrix}\left(\left(u_x^{m+1,n-1}-u_x^{m,n}\right)^2\cos^2(30)+2\left(u_x^{m+1,n-1}-u_x^{m,n}\right)\left(u_z^{m+1,n-1}-u_z^{m,n}\right)\cos(30)\sin(30)\right)\\+\left(\left(u_x^{m-1,n-1}-u_x^{m,n}\right)^2\cos^2(150)+2\left(u_x^{m-1,n-1}-u_x^{m,n}\right)\left(u_z^{m-1,n-1}-u_z^{m,n}\right)\cos(150)\sin(150)\right)\\+\left(\left(u_x^{m-1,n+1}-u_x^{m,n}\right)^2\cos^2(210)+2\left(u_x^{m-1,n+1}-u_x^{m,n}\right)\left(u_z^{m-1,n+1}-u_z^{m,n}\right)\cos(210)\sin(210)\right)\\+\left(\left(u_x^{m+1,n+1}-u_x^{m,n}\right)^2\cos^2(330)+2\left(u_x^{m+1,n+1}-u_x^{m,n}\right)\left(u_z^{m+1,n+1}-u_z^{m,n}\right)\cos(330)\sin(330)\right)\end{pmatrix}=0$$

For spring m+1,n-1:

$$\frac{1}{2}\frac{k_{m+1,n-1}}{\partial u_x}\left(\left(u_x^{m+1,n-1}-u_x^{m,n}\right)^2\cos^2(30)+2\left(u_x^{m+1,n-1}-u_x^{m,n}\right)\left(u_z^{m+1,n-1}-u_z^{m,n}\right)\cos(30)\sin(30)\right)$$

$$\frac{1}{2}\frac{k_{m+1,n-1}}{\partial u_x}\left(\left(\left(u_x^{m+1,n-1}\right)^2-u_x^{m,n}u_x^{m+1,n-1}+\left(u_x^{m,n}\right)^2\right)\cos^2(30)+2\left(u_x^{m+1,n-1}u_z^{m+1,n-1}-u_x^{m+1,n-1}u_z^{m,n}-u_x^{m,n}u_z^{m+1,n-1}+u_x^{m,n}u_z^{m,n}\right)\cos(30)\sin(30)\right)$$

$$\frac{1}{2}k_{m+1,n-1}\left(\left(2u_x^{m,n}-u_x^{m+1,n-1}\right)\cos^2(30)+2\left(u_z^{m,n}-u_z^{m+1,n-1}\right)\cos(30)\sin(30)\right)$$
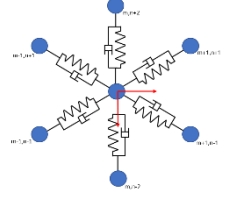
For all springs:

$$m\ddot{u}_x+\sum_j\frac{1}{2}k_j\begin{pmatrix}\left(\left(2u_x^{m,n}-2u_x^{m+1,n-1}\right)\cos^2(30)+2\left(u_z^{m,n}-u_z^{m+1,n-1}\right)\cos(30)\sin(30)\right)\\+\left(\left(2u_x^{m,n}-2u_x^{m-1,n-1}\right)\cos^2(150)+2\left(u_z^{m,n}-u_z^{m-1,n-1}\right)\cos(150)\sin(150)\right)\\+\left(\left(2u_x^{m,n}-2u_x^{m-1,n+1}\right)\cos^2(210)+2\left(u_z^{m,n}-u_z^{m-1,n+1}\right)\cos(210)\sin(210)\right)\\+\left(\left(2u_x^{m,n}-2u_x^{m+1,n+1}\right)\cos^2(330)+2\left(u_z^{m,n}-u_z^{m+1,n+1}\right)\cos(330)\sin(330)\right)\end{pmatrix}=0$$

$$m\ddot{u}_x+\sum_j\frac{1}{2}k_j\begin{pmatrix}\left(\left(2u_x^{m,n}-2u_x^{m+1,n-1}\right)\frac{3}{4}+2\left(u_z^{m,n}-u_z^{m+1,n-1}\right)\frac{1}{2}\sqrt{3}*\frac{1}{2}\right)\\+\left(\left(2u_x^{m,n}-2u_x^{m-1,n-1}\right)\frac{3}{4}+2\left(u_z^{m,n}-u_z^{m-1,n-1}\right)-\frac{1}{2}\sqrt{3}*\frac{1}{2}\right)\\+\left(\left(2u_x^{m,n}-2u_x^{m-1,n+1}\right)\frac{3}{4}+2\left(u_z^{m,n}-u_z^{m-1,n+1}\right)-\frac{1}{2}\sqrt{3}*-\frac{1}{2}\right)\\+\left(\left(2u_x^{m,n}-2u_x^{m+1,n+1}\right)\frac{3}{4}+2\left(u_z^{m,n}-u_z^{m+1,n+1}\right)\frac{1}{2}\sqrt{3}*-\frac{1}{2}\right)\end{pmatrix}=0$$

Kj = K

$$m\ddot{u}_x+k\left(3u_x^{m,n}-\frac{3}{4}\left(u_x^{m+1,n-1}+u_x^{m-1,n-1}+u_x^{m-1,n+1}+u_x^{m+1,n+1}\right)+\frac{1}{4}\sqrt{3}\left(-u_z^{m+1,n-1}+u_z^{m-1,n-1}-u_z^{m-1,n+1}+u_z^{m+1,n+1}\right)\right)=0$$

For z-direction:

$$\frac{\partial(-\sum_j \frac{1}{2}k_j((u_x^{nj}-u_x^n)^2\cos^2(x)+2(u_x^{nj}-u_x^n)(u_z^{nj}-u_z^n)\cos(x)\sin(x)+(u_z^{nj}-u_z^n)^2\sin^2(x)))}{\partial u_z}-\frac{\partial}{\partial t}\frac{\partial(\frac{1}{2}m(\dot{u}_x)^2+\frac{1}{2}m(\dot{u}_z)^2)}{\partial \dot{u}_z}=0$$

$$\frac{\partial L}{\partial u_z}-\frac{\partial}{\partial t}\frac{\partial L}{\partial \dot{u}_z}=-m\ddot{u}_z-\sum_j \frac{1}{2}\frac{k_j}{\partial u_z}((u_z^{nj}-u_z^n)^2\sin^2(x)+2(u_x^{nj}-u_x^n)(u_z^{nj}-u_z^n)\cos(x)\sin(x))=0$$

$$m\ddot{u}_z+\sum_j \frac{1}{2}\frac{k_j}{\partial u_z}\left((u_z^{nj}-u_z^n)^2\sin^2(x)+2(u_x^{nj}-u_x^n)(u_z^{nj}-u_z^n)\cos(x)\sin(x)\right)=0$$

$$m\ddot{u}_z+\sum_j \frac{1}{2}k_j\begin{pmatrix}\left(\left(u_z^{m+1,n-1}-u_z^{m,n}\right)^2\sin^2(30)+2\left(u_x^{m+1,n-1}-u_x^{m,n}\right)\left(u_z^{m+1,n-1}-u_z^{m,n}\right)\cos(30)\sin(30)\right)\\ +\left(\left(u_z^{m+1,n-1}-u_z^{m,n}\right)^2\sin^2(90)+2\left(u_x^{m+1,n-1}-u_x^{m,n}\right)\left(u_z^{m+1,n-1}-u_z^{m,n}\right)\cos(90)\sin(90)\right)\\ +\left(\left(u_z^{m-1,n-1}-u_z^{m,n}\right)^2\sin^2(150)+2\left(u_x^{m-1,n-1}-u_x^{m,n}\right)\left(u_z^{m-1,n-1}-u_z^{m,n}\right)\cos(150)\sin(150)\right)\\ +\left(\left(u_z^{m+1,n-1}-u_z^{m,n}\right)^2\sin^2(180)+2\left(u_x^{m+1,n-1}-u_x^{m,n}\right)\left(u_z^{m+1,n-1}-u_z^{m,n}\right)\cos(180)\sin(180)\right)\\ +\left(\left(u_z^{m-1,n+1}-u_z^{m,n}\right)^2\sin^2(210)+2\left(u_x^{m-1,n+1}-u_x^{m,n}\right)\left(u_z^{m-1,n+1}-u_z^{m,n}\right)\cos(210)\sin(210)\right)\\ +\left(\left(u_z^{m+1,n+1}-u_z^{m,n}\right)^2\sin^2(330)+2\left(u_x^{m+1,n+1}-u_x^{m,n}\right)\left(u_z^{m+1,n+1}-u_z^{m,n}\right)\cos(330)\sin(330)\right)\end{pmatrix}=0$$
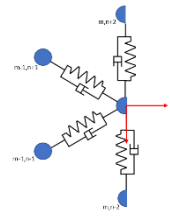
$$m\ddot{u}_z+\sum_j \frac{1}{2}k_j\begin{pmatrix}\left(\left(2u_z^{m,n}-2u_z^{m+1,n-1}\right)\sin^2(30)+2\left(u_x^{m,n}-u_x^{m+1,n-1}\right)\cos(30)\sin(30)\right)\\ +\left(\left(2u_z^{m,n}-2u_z^{m,n-2}\right)\sin^2(90)+2\left(u_x^{m,n}-u_x^{m,n-2}\right)\cos(90)\sin(90)\right)\\ +\left(\left(2u_z^{m,n}-2u_z^{m-1,n-1}\right)\sin^2(150)+2\left(u_x^{m,n}-u_x^{m-1,n-1}\right)\cos(150)\sin(150)\right)\\ +\left(\left(2u_z^{m,n}-2u_z^{m-1,n+1}\right)\sin^2(210)+2\left(u_x^{m,n}-u_x^{m-1,n+1}\right)\cos(210)\sin(210)\right)\\ +\left(\left(2u_z^{m,n}-2u_z^{m,n+2}\right)\sin^2(270)+2\left(u_x^{m,n}-u_x^{m,n+2}\right)\cos(270)\sin(270)\right)\\ +\left(\left(2u_z^{m,n}-2u_z^{m+1,n+1}\right)\sin^2(330)+2\left(u_x^{m,n}-u_x^{m+1,n+1}\right)\cos(330)\sin(330)\right)\end{pmatrix}=0$$

$$m\ddot{u}_z+\sum_j \frac{1}{2}k_j\begin{pmatrix}\left(\left(2u_z^{m,n}-2u_z^{m+1,n-1}\right)\frac{1}{4}+2\left(u_x^{m,n}-u_x^{m+1,n-1}\right)\frac{1}{2}\sqrt{3}*\frac{1}{2}\right)\\ +\left(\left(2u_z^{m,n}-2u_z^{m,n-2}\right)1+2\left(u_x^{m,n}-u_x^{m,n-2}\right)0*1\right)\\ +\left(\left(2u_z^{m,n}-2u_z^{m-1,n-1}\right)\frac{1}{4}+2\left(u_x^{m,n}-u_x^{m-1,n-1}\right)-\frac{1}{2}\sqrt{3}*\frac{1}{2}\right)\\ +\left(\left(2u_z^{m,n}-2u_z^{m-1,n+1}\right)\frac{1}{4}+2\left(u_x^{m,n}-u_x^{m-1,n+1}\right)-\frac{1}{2}\sqrt{3}*-\frac{1}{2}\right)\\ +\left(\left(2u_z^{m,n}-2u_z^{m,n+2}\right)1+2\left(u_x^{m,n}-u_x^{m,n+2}\right)0*-1\right)\\ +\left(\left(2u_z^{m,n}-2u_z^{m+1,n+1}\right)\frac{1}{4}+2\left(u_x^{m,n}-u_x^{m+1,n+1}\right)\frac{1}{2}\sqrt{3}*-\frac{1}{2}\right)\end{pmatrix}=0$$

Kj = K

$$m\ddot{u}_z+k\left(3u_z^{m,n}-u_z^{m,n-2}-u_z^{m,n+2}-\frac{1}{4}\left(u_z^{m+1,n-1}+u_z^{m-1,n-1}+u_z^{m-1,n+1}+u_z^{m+1,n+1}\right)+\frac{1}{4}\sqrt{3}\left(u_x^{m+1,n-1}-u_x^{m-1,n-1}+u_x^{m-1,n+1}-u_x^{m+1,n+1}\right)\right)=0$$

6.3 Derivation for edge of pile and interface nodes.

For x-direction:

$$\frac{\partial(-\sum_j \frac{1}{2}k_j((u_x^{nj}-u_x^n)^2\cos^2(x)+2(u_x^{nj}-u_x^n)(u_z^{nj}-u_z^n)\cos(x)\sin(x)+(u_z^{nj}-u_z^n)^2\sin^2(x)))}{\partial u_x} - \frac{\partial}{\partial t}\frac{\partial(\frac{1}{2}(\frac{1}{2}m)(\dot{u}_x)^2+\frac{1}{2}(\frac{1}{2}m)(\dot{u}_z)^2)}{\partial \dot{u}_x}=0$$

$$\frac{\partial L}{\partial u_x}-\frac{\partial}{\partial t}\frac{\partial L}{\partial \dot{u}_x}=-\frac{1}{2}m\ddot{u}_x-\sum_j\frac{1}{2}\frac{k_j}{\partial u_x}((u_x^{nj}-u_x^n)^2\cos^2(x)+2(u_x^{nj}-u_x^n)(u_z^{nj}-u_z^n)\cos(x)\sin(x))=0$$

$$\frac{1}{2}m\ddot{u}_x+\sum_j\frac{1}{2}\frac{k_j}{\partial u_x}\Big((u_x^{nj}-u_x^n)^2\cos^2(x)+2(u_x^{nj}-u_x^n)(u_z^{nj}-u_z^n)\cos(x)\sin(x)\Big)=0$$

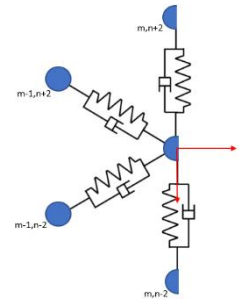$$\frac{1}{2}m\ddot{u}_x+\sum_j\frac{1}{2}\frac{k_j}{\partial u_x}\left(\begin{array}{c}\left(\left(u_x^{m-1,n-1}-u_x^{m,n}\right)^2\cos^2(150)+2\left(u_x^{m-1,n-1}-u_x^{m,n}\right)\left(u_z^{m-1,n-1}-u_z^{m,n}\right)\cos(150)\sin(150)\right)\\+\left(\left(u_x^{m-1,n+1}-u_x^{m,n}\right)^2\cos^2(210)+2\left(u_x^{m-1,n+1}-u_x^{m,n}\right)\left(u_z^{m-1,n+1}-u_z^{m,n}\right)\cos(210)\sin(210)\right)\end{array}\right)=0$$

$$\frac{1}{2}m\ddot{u}_x+\sum_j\frac{1}{2}k_j\left(\begin{array}{c}\left(\left(2u_x^{m,n}-2u_x^{m-1,n-1}\right)\cos^2(150)+2\left(u_z^{m,n}-u_z^{m-1,n-1}\right)\cos(150)\sin(150)\right)\\+\left(\left(2u_x^{m,n}-2u_x^{m-1,n+1}\right)\cos^2(210)+2\left(u_z^{m,n}-u_z^{m-1,n+1}\right)\cos(210)\sin(210)\right)\end{array}\right)=0$$

$$\frac{1}{2}m\ddot{u}_x+\sum_j\frac{1}{2}k_j\left(\begin{array}{c}\left(\left(2u_x^{m,n}-2u_x^{m-1,n-1}\right)\frac{3}{4}+2\left(u_z^{m,n}-u_z^{m-1,n-1}\right)-\frac{1}{2}\sqrt{3}*\frac{1}{2}\right)\\+\left(\left(2u_x^{m,n}-2u_x^{m-1,n+1}\right)\frac{3}{4}+2\left(u_z^{m,n}-u_z^{m-1,n+1}\right)-\frac{1}{2}\sqrt{3}*-\frac{1}{2}\right)\end{array}\right)=0$$

Kj = K

$$\frac{1}{2}m\ddot{u}_x+k\left(\frac{3}{2}u_x^{m,n}-\frac{3}{4}\left(u_x^{m-1,n-1}+u_x^{m-1,n+1}\right)+\frac{1}{4}\sqrt{3}\left(u_z^{m-1,n-1}-u_z^{m-1,n+1}\right)\right)=0$$

For z-direction:

$$\frac{\partial(-\sum_j \frac{1}{2}k_j((u_x^{nj}-u_x^n)^2\cos^2(x)+2(u_x^{nj}-u_x^n)(u_z^{nj}-u_z^n)\cos(x)\sin(x)+(u_z^{nj}-u_z^n)^2\sin^2(x)))}{\partial u_z}-\frac{\partial}{\partial t}\frac{\partial(\frac{1}{2}(\frac{1}{2}m)(\dot{u}_x)^2+\frac{1}{2}(\frac{1}{2}m)(\dot{u}_z)^2)}{\partial \dot{u}_z}=0$$

$$\frac{\partial L}{\partial u_z}-\frac{\partial}{\partial t}\frac{\partial L}{\partial \dot{u}_z}=-\frac{1}{2}m\ddot{u}_z-\sum_j\frac{1}{2}\frac{k_j}{\partial u_z}((u_z^{nj}-u_z^n)^2\sin^2(x)+2(u_x^{nj}-u_x^n)(u_z^{nj}-u_z^n)\cos(x)\sin(x))=0$$

$$\frac{1}{2}m\ddot{u}_z+\sum_j\frac{1}{2}\frac{k_j}{\partial u_z}\left((u_z^{nj}-u_z^n)^2\sin^2(x)+2(u_x^{nj}-u_x^n)(u_z^{nj}-u_z^n)\cos(x)\sin(x)\right)=0$$

$$\frac{1}{2}m\ddot{u}_z+\sum_j\frac{1}{2}k_j\begin{pmatrix}\frac{1}{2}\left(\left(u_z^{m+1,n-1}-u_z^{m,n}\right)^2\sin^2(90)+2\left(u_x^{m+1,n-1}-u_x^{m,n}\right)\left(u_z^{m+1,n-1}-u_z^{m,n}\right)\cos(90)\sin(90)\right)\\ +\left(\left(u_z^{m-1,n-1}-u_z^{m,n}\right)^2\sin^2(150)+2\left(u_x^{m-1,n-1}-u_x^{m,n}\right)\left(u_z^{m-1,n-1}-u_z^{m,n}\right)\cos(150)\sin(150)\right)\\ +\left(\left(u_z^{m+1,n-1}-u_z^{m,n}\right)^2\sin^2(180)+2\left(u_x^{m+1,n-1}-u_x^{m,n}\right)\left(u_z^{m+1,n-1}-u_z^{m,n}\right)\cos(180)\sin(180)\right)\\ +\frac{1}{2}\left(\left(u_z^{m-1,n+1}-u_z^{m,n}\right)^2\sin^2(210)+2\left(u_x^{m-1,n+1}-u_x^{m,n}\right)\left(u_z^{m-1,n+1}-u_z^{m,n}\right)\cos(210)\sin(210)\right)\end{pmatrix}=0$$

$$\frac{1}{2}m\ddot{u}_z+\sum_j\frac{1}{2}k_j\begin{pmatrix}\frac{1}{2}\left(\left(2u_z^{m,n}-2u_z^{m,n-2}\right)\sin^2(90)+2\left(u_x^{m,n}-u_x^{m,n-2}\right)\cos(90)\sin(90)\right)\\ +\left(\left(2u_z^{m,n}-2u_z^{m-1,n-1}\right)\sin^2(150)+2\left(u_x^{m,n}-u_x^{m-1,n-1}\right)\cos(150)\sin(150)\right)\\ +\left(\left(2u_z^{m,n}-2u_z^{m-1,n+1}\right)\sin^2(210)+2\left(u_x^{m,n}-u_x^{m-1,n+1}\right)\cos(210)\sin(210)\right)\\ +\frac{1}{2}\left(\left(2u_z^{m,n}-2u_z^{m,n+2}\right)\sin^2(270)+2\left(u_x^{m,n}-u_x^{m,n+2}\right)\cos(270)\sin(270)\right)\end{pmatrix}=0$$

$$\frac{1}{2}m\ddot{u}_z+\sum_j\frac{1}{2}k_j\begin{pmatrix}\frac{1}{2}\left(\left(2u_z^{m,n}-2u_z^{m,n-2}\right)1+2\left(u_x^{m,n}-u_x^{m,n-2}\right)0*1\right)\\ +\left(\left(2u_z^{m,n}-2u_z^{m-1,n-1}\right)\frac{1}{4}+2\left(u_x^{m,n}-u_x^{m-1,n-1}\right)-\frac{1}{2}\sqrt{3}*\frac{1}{2}\right)\\ +\left(\left(2u_z^{m,n}-2u_z^{m-1,n+1}\right)\frac{1}{4}+2\left(u_x^{m,n}-u_x^{m-1,n+1}\right)-\frac{1}{2}\sqrt{3}*-\frac{1}{2}\right)\\ +\frac{1}{2}\left(\left(2u_z^{m,n}-2u_z^{m,n+2}\right)1+2\left(u_x^{m,n}-u_x^{m,n+2}\right)0*-1\right)\end{pmatrix}=0$$

Kj = K

$$\frac{1}{2}m\ddot{u}_z+k\left(\frac{3}{2}u_z^{m,n}-\frac{1}{2}u_z^{m,n-2}-\frac{1}{2}u_z^{m,n+2}-\frac{1}{4}\left(u_z^{m-1,n-1}+u_z^{m-1,n+1}\right)+\frac{1}{4}\sqrt{3}\left(u_x^{m-1,n-1}+u_x^{m-1,n+1}\right)\right)=0$$

6.4 Derivation for edge of pile and interface nodes.

For x-direction:

$$\frac{\partial(-\sum_j \frac{1}{2}k_j((u_x^{nj}-u_x^n)^2\cos^2(x)+2(u_x^{nj}-u_x^n)(u_z^{nj}-u_z^n)\cos(x)\sin(x)+(u_z^{nj}-u_z^n)^2\sin^2(x)))}{\partial u_x} - \frac{\partial}{\partial t}\frac{\partial(\frac{1}{2}(\frac{1}{2}m)(\dot{u}_x)^2+\frac{1}{2}(\frac{1}{2}m)(\dot{u}_z)^2)}{\partial \dot{u}_x}=0$$

$$\frac{\partial L}{\partial u_x}-\frac{\partial}{\partial t}\frac{\partial L}{\partial \dot{u}_x}=-\frac{1}{2}m\ddot{u}_x-\sum_j\frac{1}{2}\frac{k_j}{\partial u_x}((u_x^{nj}-u_x^n)^2\cos^2(x)+2(u_x^{nj}-u_x^n)(u_z^{nj}-u_z^n)\cos(x)\sin(x))=0$$

$$\frac{1}{2}m\ddot{u}_x+\sum_j\frac{1}{2}\frac{k_j}{\partial u_x}\left((u_x^{nj}-u_x^n)^2\cos^2(x)+2(u_x^{nj}-u_x^n)(u_z^{nj}-u_z^n)\cos(x)\sin(x)\right)=0$$

$$\frac{1}{2}m\ddot{u}_x+\sum_j\frac{1}{2}\frac{k_j}{\partial u_x}\left(\begin{array}{l}\left(\left(u_x^{m+1,n-1}-u_x^{m,n}\right)^2\cos^2(30)+2\left(u_x^{m+1,n-1}-u_x^{m,n}\right)\left(u_z^{m+1,n-1}-u_z^{m,n}\right)\cos(30)\sin(30)\right)\\+\left(\left(u_x^{m+1,n+1}-u_x^{m,n}\right)^2\cos^2(330)+2\left(u_x^{m+1,n+1}-u_x^{m,n}\right)\left(u_z^{m+1,n+1}-u_z^{m,n}\right)\cos(330)\sin(330)\right)\end{array}\right)=0$$
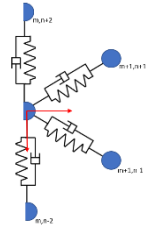
For all springs:

$$\frac{1}{2}m\ddot{u}_x+\sum_j\frac{1}{2}k_j\left(\begin{array}{l}\left(\left(2u_x^{m,n}-2u_x^{m+1,n-1}\right)\cos^2(30)+2\left(u_z^{m,n}-u_z^{m+1,n-1}\right)\cos(30)\sin(30)\right)\\+\left(\left(2u_x^{m,n}-2u_x^{m+1,n+1}\right)\cos^2(330)+2\left(u_z^{m,n}-u_z^{m+1,n+1}\right)\cos(330)\sin(330)\right)\end{array}\right)=0$$

$$\frac{1}{2}m\ddot{u}_x+\sum_j\frac{1}{2}k_j\left(\begin{array}{l}\left(\left(2u_x^{m,n}-2u_x^{m+1,n-1}\right)\frac{3}{4}+2\left(u_z^{m,n}-u_z^{m+1,n-1}\right)\frac{1}{2}\sqrt{3}*\frac{1}{2}\right)\\+\left(\left(2u_x^{m,n}-2u_x^{m+1,n+1}\right)\frac{3}{4}+2\left(u_z^{m,n}-u_z^{m+1,n+1}\right)\frac{1}{2}\sqrt{3}*-\frac{1}{2}\right)\end{array}\right)=0$$

Kj = K

$$\frac{1}{2}m\ddot{u}_x+k\left(\frac{3}{2}u_x^{m,n}-\frac{3}{4}\left(u_x^{m+1,n-1}+u_x^{m+1,n+1}\right)+\frac{1}{4}\sqrt{3}\left(-u_z^{m+1,n-1}+u_z^{m+1,n+1}\right)\right)=0$$

For z-direction:

$$\frac{\partial(-\sum_j \frac{1}{2}k_j((u_x^{nj}-u_x^n)^2\cos^2(x)+2(u_x^{nj}-u_x^n)(u_z^{nj}-u_z^n)\cos(x)\sin(x)+(u_z^{nj}-u_z^n)^2\sin^2(x)))}{\partial u_z}-\frac{\partial}{\partial t}\frac{\partial(\frac{1}{2}(\frac{1}{2}m)(\dot{u}_x)^2+\frac{1}{2}(\frac{1}{2}m)(\dot{u}_z)^2)}{\partial \dot{u}_z}=0$$

$$\frac{\partial L}{\partial u_z}-\frac{\partial}{\partial t}\frac{\partial L}{\partial \dot{u}_z}=-\frac{1}{2}m\ddot{u}_z-\sum_j \frac{1}{2}\frac{k_j}{\partial u_z}((u_z^{nj}-u_z^n)^2\sin^2(x)+2(u_x^{nj}-u_x^n)(u_z^{nj}-u_z^n)\cos(x)\sin(x))=0$$

$$\frac{1}{2}m\ddot{u}_z+\sum_j \frac{1}{2}\frac{k_j}{\partial u_z}\left((u_z^{nj}-u_z^n)^2\sin^2(x)+2(u_x^{nj}-u_x^n)(u_z^{nj}-u_z^n)\cos(x)\sin(x)\right)=0$$

$$\frac{1}{2}m\ddot{u}_z+\sum_j \frac{1}{2}k_j\left(\begin{array}{l}\left(\left(u_z^{m+1,n-1}-u_z^{m,n}\right)^2\sin^2(30)+2\left(u_x^{m+1,n-1}-u_x^{m,n}\right)\left(u_z^{m+1,n-1}-u_z^{m,n}\right)\cos(30)\sin(30)\right)\\[4pt]+\frac{1}{2}\left(\left(u_z^{m,n-2}-u_z^{m,n}\right)^2\sin^2(90)+2\left(u_x^{m,n-2}-u_x^{m,n}\right)\left(u_z^{m,n-2}-u_z^{m,n}\right)\cos(90)\sin(90)\right)\\[4pt]+\frac{1}{2}\left(\left(u_z^{m,n+2}-u_z^{m,n}\right)^2\sin^2(270)+2\left(u_x^{m,n+2}-u_x^{m,n}\right)\left(u_z^{m,n+2}-u_z^{m,n}\right)\cos(270)\sin(270)\right)\\[4pt]+\left(\left(u_z^{m+1,n+1}-u_z^{m,n}\right)^2\sin^2(330)+2\left(u_x^{m+1,n+1}-u_x^{m,n}\right)\left(u_z^{m+1,n+1}-u_z^{m,n}\right)\cos(330)\sin(330)\right)\end{array}\right)=0$$
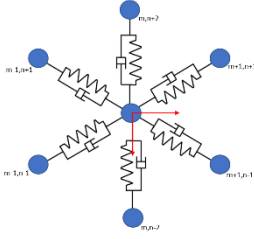
$$\frac{1}{2}m\ddot{u}_z+\sum_j \frac{1}{2}k_j\left(\begin{array}{l}\left(\left(2u_z^{m,n}-2u_z^{m+1,n-1}\right)\sin^2(30)+\left(u_x^{m,n}-u_x^{m+1,n-1}\right)\cos(30)\sin(30)\right)\\[4pt]+\frac{1}{2}\left(\left(2u_z^{m,n}-2u_z^{m,n-2}\right)\sin^2(90)+\left(u_x^{m,n}-u_x^{m,n-2}\right)\cos(90)\sin(90)\right)\\[4pt]+\frac{1}{2}\left(\left(2u_z^{m,n}-2u_z^{m,n+2}\right)\sin^2(270)+\left(u_x^{m,n}-u_x^{m,n+2}\right)\cos(270)\sin(270)\right)\\[4pt]+\left(\left(2u_z^{m,n}-2u_z^{m+1,n+1}\right)\sin^2(330)+\left(u_x^{m,n}-u_x^{m+1,n+1}\right)\cos(330)\sin(330)\right)\end{array}\right)=0$$

$$\frac{1}{2}m\ddot{u}_z+\sum_j \frac{1}{2}k_j\left(\begin{array}{l}\left(\left(2u_z^{m,n}-2u_z^{m+1,n-1}\right)\frac{1}{4}+\left(u_x^{m,n}-u_x^{m+1,n-1}\right)\frac{1}{2}\sqrt{3}*\frac{1}{2}\right)\\[4pt]+\frac{1}{2}\left(\left(2u_z^{m,n}-2u_z^{m,n-2}\right)1+\left(u_x^{m,n}-u_x^{m,n-2}\right)0*1\right)\\[4pt]+\frac{1}{2}\left(\left(2u_z^{m,n}-2u_z^{m,n+2}\right)1+\left(u_x^{m,n}-u_x^{m,n+2}\right)0*-1\right)\\[4pt]+\left(\left(2u_z^{m,n}-2u_z^{m+1,n+1}\right)\frac{1}{4}+\left(u_x^{m,n}-u_x^{m+1,n+1}\right)\frac{1}{2}\sqrt{3}*-\frac{1}{2}\right)\end{array}\right)=0$$
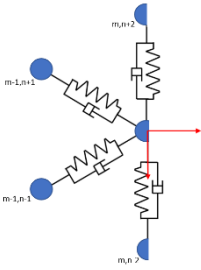
Kj = K

$$\frac{1}{2}m\ddot{u}_z+k\left(\frac{3}{2}u_z^{m,n}-\frac{1}{2}u_z^{m,n-2}-\frac{1}{2}u_z^{m,n+2}-\frac{1}{4}\left(u_z^{m+1,n-1}+u_z^{m+1,n+1}\right)+\frac{1}{4}\sqrt{3}\left(u_x^{m+1,n-1}-u_x^{m+1,n+1}\right)\right)=0$$
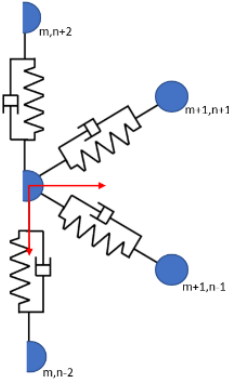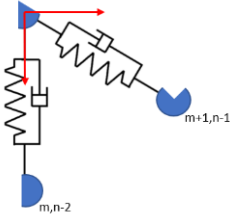
6.5 EOM's for all possible configurations

$$m\ddot{u}_x + k\left(3u_x^{m,n} - \tfrac{3}{4}\left(u_x^{m+1,n-1} + u_x^{m-1,n-1} + u_x^{m-1,n+1} + u_x^{m+1,n+1}\right) + \tfrac{1}{4}\sqrt{3}\left(-u_z^{m+1,n-1} + u_z^{m-1,n-1} - u_z^{m-1,n+1} + u_z^{m+1,n+1}\right)\right) = 0$$

$$m\ddot{u}_z + k\left(3u_z^{m,n} - u_z^{m,n-2} - u_z^{m,n+2} - \tfrac{1}{4}\left(u_z^{m+1,n-1} + u_z^{m-1,n-1} + u_z^{m-1,n+1} + u_z^{m+1,n+1}\right) + \tfrac{1}{4}\sqrt{3}\left(u_x^{m+1,n-1} - u_x^{m-1,n-1} + u_x^{m-1,n+1} - u_x^{m+1,n+1}\right)\right) = 0$$

$$\tfrac{1}{2}m\ddot{u}_x + k\left(\tfrac{3}{2}u_x^{m,n} - \tfrac{3}{4}\left(u_x^{m-1,n-1} + u_x^{m-1,n+1}\right) + \tfrac{1}{4}\sqrt{3}\left(u_z^{m-1,n-1} - u_z^{m-1,n+1}\right)\right) = 0$$

$$\tfrac{1}{2}m\ddot{u}_z + k\left(\tfrac{3}{2}u_z^{m,n} - \tfrac{1}{2}u_z^{m,n-2} - \tfrac{1}{2}u_z^{m,n+2} - \tfrac{1}{4}\left(u_z^{m-1,n-1} + u_z^{m-1,n+1}\right) + \tfrac{1}{4}\sqrt{3}\left(-u_x^{m-1,n-1} + u_x^{m-1,n+1}\right)\right) = 0$$
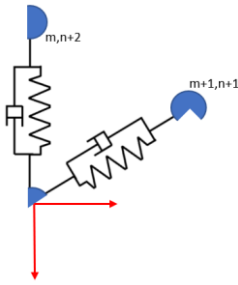

$$\tfrac{1}{2}m\ddot{u}_x + k\left(\tfrac{3}{2}u_x^{m,n} - \tfrac{3}{4}\left(u_x^{m+1,n-1} + u_x^{m+1,n+1}\right) + \tfrac{1}{4}\sqrt{3}\left(-u_z^{m+1,n-1} + u_z^{m+1,n+1}\right)\right) = 0$$

$$\tfrac{1}{2}m\ddot{u}_z + k\left(\tfrac{3}{2}u_z^{m,n} - \tfrac{1}{2}u_z^{m,n-2} - \tfrac{1}{2}u_z^{m,n+2} - \tfrac{1}{4}\left(u_z^{m+1,n-1} + u_z^{m+1,n+1}\right) + \tfrac{1}{4}\sqrt{3}\left(u_x^{m+1,n-1} - u_x^{m+1,n+1}\right)\right) = 0$$
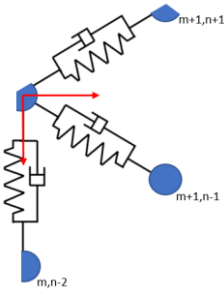
$$\frac{1}{6} m \ddot{u}_x + k \left(\frac{3}{8} u_x^{m,n} - \frac{3}{8} u_x^{m+1,n-1} - \frac{1}{8} \sqrt{3} * u_z^{m+1,n-1} \right) = 0$$

$$\frac{1}{6} m \ddot{u}_z + k \left(\frac{5}{8} u_z^{m,n} - \frac{1}{2} u_z^{m,n-2} - \frac{1}{8} u_z^{m+1,n-1} + \frac{1}{8} \sqrt{3} * u_x^{m+1,n-1} \right) = 0$$
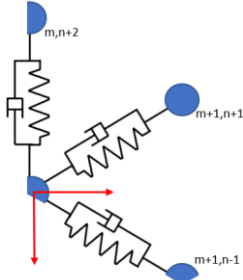

$$\frac{1}{6} m \ddot{u}_x + k \left(\frac{3}{8} u_x^{m,n} - \frac{3}{8} u_x^{m+1,n+1} + \frac{1}{8} \sqrt{3} * u_z^{m+1,n+1} \right) = 0$$

$$\frac{1}{6} m \ddot{u}_z + k \left(\frac{5}{8} u_z^{m,n} - \frac{1}{2} u_z^{m,n+2} - \frac{1}{8} u_z^{m+1,n+1} - \frac{1}{8} \sqrt{3} * u_x^{m+1,n+1} \right) = 0$$
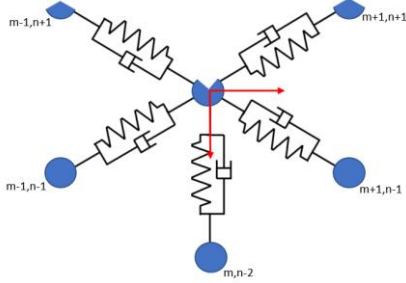

$$\frac{1}{3} m \ddot{u}_x + k \left(\frac{9}{8} u_x^{m,n} - \frac{3}{4} \left(u_x^{m+1,n-1} + \frac{1}{2} u_x^{m+1,n+1} \right) + \frac{1}{4} \sqrt{3} \left(-u_z^{m+1,n-1} + \frac{1}{2} u_z^{m+1,n+1} \right) \right) = 0$$

$$\frac{1}{3} m \ddot{u}_z + k \left(\frac{7}{8} u_z^{m,n} - \frac{1}{2} u_z^{m,n-2} - \frac{1}{4} \left(u_z^{m+1,n-1} + \frac{1}{2} u_z^{m+1,n+1} \right) + \frac{1}{4} \sqrt{3} \left(u_x^{m+1,n-1} - \frac{1}{2} u_x^{m+1,n+1} \right) \right) = 0$$
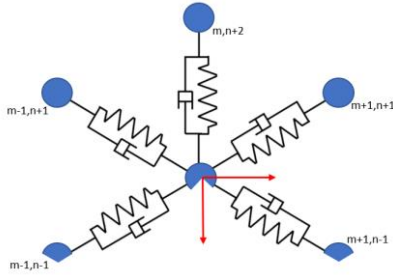
$$\frac{1}{3}m\ddot{u}_x + k\left(\frac{9}{8}u_x^{m,n} - \frac{3}{4}\left(\frac{1}{2}u_x^{m+1,n-1} + u_x^{m+1,n+1}\right) + \frac{1}{4}\sqrt{3}\left(-\frac{1}{2}u_z^{m+1,n-1} + u_z^{m+1,n+1}\right)\right) = 0$$

$$\frac{1}{3}m\ddot{u}_z + k\left(\frac{7}{8}u_z^{m,n} - \frac{1}{2}u_z^{m,n+2} - \frac{1}{4}\left(\frac{1}{2}u_z^{m+1,n-1} + u_z^{m+1,n+1}\right) + \frac{1}{4}\sqrt{3}\left(\frac{1}{2}u_x^{m+1,n-1} - u_x^{m+1,n+1}\right)\right) = 0$$
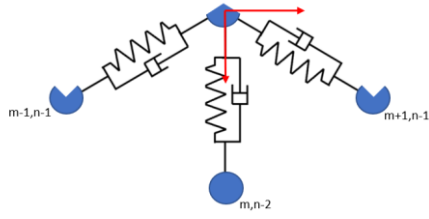

$$\frac{2}{3}m\ddot{u}_x + k\left(\frac{9}{4}u_x^{m,n} - \frac{3}{4}\left(u_x^{m+1,n-1} + u_x^{m-1,n-1} + \frac{1}{2}u_x^{m-1,n+1} + \frac{1}{2}u_x^{m+1,n+1}\right) + \frac{1}{4}\sqrt{3}\left(-u_z^{m+1,n-1} + u_z^{m-1,n-1} - \frac{1}{2}u_z^{m-1,n+1} + \frac{1}{2}u_z^{m+1,n+1}\right)\right) = 0$$

$$\frac{2}{3}m\ddot{u}_z + k\left(\frac{7}{4}u_z^{m,n} - u_z^{m,n-2} - \frac{1}{4}\left(u_z^{m+1,n-1} + u_z^{m-1,n-1} + \frac{1}{2}u_z^{m-1,n+1} + \frac{1}{2}u_z^{m+1,n+1}\right) + \frac{1}{4}\sqrt{3}\left(u_x^{m+1,n-1} - u_x^{m-1,n-1} + \frac{1}{2}u_x^{m-1,n+1} - \frac{1}{2}u_x^{m+1,n+1}\right)\right) = 0$$
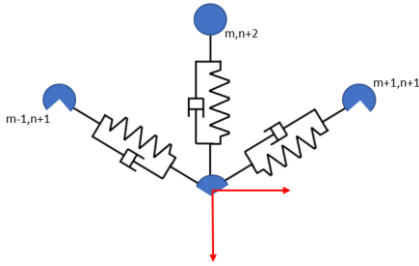

$$\frac{2}{3}m\ddot{u}_x + k\left(\frac{9}{4}u_x^{m,n} - \frac{3}{4}\left(\frac{1}{2}u_x^{m+1,n-1} + \frac{1}{2}u_x^{m-1,n-1} + u_x^{m-1,n+1} + u_x^{m+1,n+1}\right) + \frac{1}{4}\sqrt{3}\left(-\frac{1}{2}u_z^{m+1,n-1} + \frac{1}{2}u_z^{m-1,n-1} - u_z^{m-1,n+1} + u_z^{m+1,n+1}\right)\right) = 0$$

$$\frac{2}{3}m\ddot{u}_z + k\left(\frac{7}{4}u_z^{m,n} - u_z^{m,n+2} - \frac{1}{4}\left(\frac{1}{2}u_z^{m+1,n-1} + \frac{1}{2}u_z^{m-1,n-1} + u_z^{m-1,n+1} + u_z^{m+1,n+1}\right) + \frac{1}{4}\sqrt{3}\left(\frac{1}{2}u_x^{m+1,n-1} - \frac{1}{2}u_x^{m-1,n-1} + u_x^{m-1,n+1} - u_x^{m+1,n+1}\right)\right) = 0$$

$$\frac{1}{3}m\ddot{u}_x + k\left(\frac{3}{4}u_x^{m,n} - \frac{3}{8}\left(u_x^{m+1,n-1} + u_x^{m-1,n-1}\right) + \frac{1}{8}\sqrt{3}\left(-u_z^{m+1,n-1} + u_z^{m-1,n-1}\right)\right) = 0$$

$$\frac{1}{3}m\ddot{u}_z + k\left(\frac{5}{4}u_z^{m,n} - u_z^{m,n-2} - \frac{1}{8}\left(u_z^{m+1,n-1} + u_z^{m-1,n-1}\right) + \frac{1}{8}\sqrt{3}\left(u_x^{m+1,n-1} - u_x^{m-1,n-1}\right)\right) = 0$$

$$\frac{1}{3}m\ddot{u}_x + k\left(\frac{3}{4}u_x^{m,n} - \frac{3}{8}\left(u_x^{m-1,n+1} + u_x^{m+1,n+1}\right) + \frac{1}{8}\sqrt{3}\left(-u_z^{m-1,n+1} + u_z^{m+1,n+1}\right)\right) = 0$$

$$\frac{1}{3}m\ddot{u}_z + k\left(\frac{5}{4}u_z^{m,n} - u_z^{m,n+2} - \frac{1}{8}\left(u_z^{m-1,n+1} + u_z^{m+1,n+1}\right) + \frac{1}{8}\sqrt{3}\left(u_x^{m-1,n+1} - u_x^{m+1,n+1}\right)\right) = 0$$